

SOURCE VARIATION AND GROUND ACCESSIBILITY OF
MAGNETOSPHERIC MID-LATITUDE ELF/VLF
CHORUS AND HISS

A DISSERTATION
SUBMITTED TO THE DEPARTMENT OF
ELECTRICAL ENGINEERING
AND THE COMMITTEE ON GRADUATE STUDIES
OF STANFORD UNIVERSITY
IN PARTIAL FULFILLMENT OF THE REQUIREMENTS
FOR THE DEGREE OF
DOCTOR OF PHILOSOPHY

Daniel Irving Golden
February 2011

2011 by Daniel I Golden. All Rights Reserved.

Re-distributed by Stanford University under license with the author.

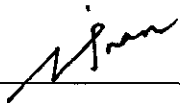


This work is licensed under a Creative Commons Attribution-Noncommercial 3.0 United States License.

<http://creativecommons.org/licenses/by-nc/3.0/us/>


This dissertation is online at: <http://purl.stanford.edu/pj437wk3608>

I certify that I have read this dissertation and that, in my opinion, it is fully adequate in scope and quality as a dissertation for the degree of Doctor of Philosophy.



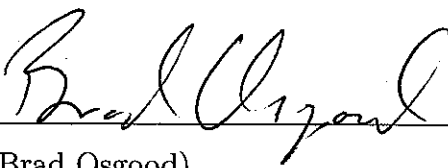
(Umran S. Inan) Principal Adviser

I certify that I have read this dissertation and that, in my opinion, it is fully adequate in scope and quality as a dissertation for the degree of Doctor of Philosophy.



(Maria Spasojevic)

I certify that I have read this dissertation and that, in my opinion, it is fully adequate in scope and quality as a dissertation for the degree of Doctor of Philosophy.



(Brad Osgood)

Approved for the University Committee on Graduate Studies

*There once was a chorus display
About which Umran did say,
“Analyze this for years
‘Till a pattern appears
And I’ll sign your thesis that day.”*

Abstract

The distribution of relativistic electrons that form the Earth's radiation belts is extremely variable, with the trapped flux changing by several orders of magnitude on timescales of a few hours to days. These energetic particles pose a significant hazard to satellites and astronauts in the near-Earth space environment. The dynamic evolution of the radiation belts is believed to be controlled in large part by two separate but related classes of naturally occurring plasma waves: extremely low frequency/very low frequency (ELF/VLF) chorus and hiss. Although these waves can be observed in situ, ground-based observing stations can provide orders of magnitude higher data volumes and decades long data coverage essential for certain long-term and statistical studies of wave properties. This dissertation explores characteristics of chorus and hiss observed at Palmer Station, Antarctica ($L=2.4$, 50°S invariant latitude) with the goal of improving our ability to differentiate between effects of emission sources and the effects of their propagation to the ground.

In order to perform a meaningful statistical analysis of emissions, it is necessary to identify them in the data. To this end, an automated system of detecting and categorizing chorus and hiss in broadband ELF/VLF data using neural networks has been developed. The system has been used to process ten years of data at Palmer Station from May 2000 through May 2010, providing the first long term, spectrally-categorized database of broadband ELF/VLF chorus and hiss emissions.

Using this database, diurnal, seasonal and solar cyclical variations of emissions are analyzed. Chorus is observed exclusively in the dawn sector while hiss is observed at all magnetic local times, peaking in the dawn and dusk sectors. The average rate of both emissions in a given year is highly correlated with the average level of

geomagnetic activity in that year. In contrast, the average rate of chorus emissions in a given month is primarily dependent on the seasonal variation of the day/night terminator, with few emissions seen during local day and prodigious emissions seen during local night. The variation of hiss emissions is similar but less pronounced.

The distance between ground receivers and the magnetospheric source of waves poses a significant challenge to separating the effects of emission sources from effects of their propagation to the ground. It is widely believed that all magnetospheric emissions observed on the ground have been ducted by field-aligned plasma density irregularities, which confine the emissions to a single magnetic field line and constrict their wavenormal angles to be nearly field-aligned. This paradigm is explored through a combination of data analysis and numerical simulations. First, the observed emissions at Palmer are compared with satellite measurements of plasmasphere extent. It is found that chorus occurrence at Palmer peaks when the plasmapause is somewhat beyond Palmer's latitude. This relationship is confirmed via end-to-end modeling of chorus propagation from the source region to the ground using raytracing, magnetospheric Landau damping, and a full wave model of subionospheric propagation. The result of this modeling is a proxy estimate of chorus observation probability at Palmer as a function of plasmasphere extent. The results of modeling agree with observations and indicate that the observed plasmaspheric control over chorus propagation is a consequence of the fact that the observed chorus propagates in a non-ducted mode from the source region to the ground. This newly-explored mode of propagation to the ground indicates that ground stations may be able to observe waves over a significantly larger portion of the magnetospheric source region than would be possible if they were restricted to observing ducted emissions. This analysis provides for a more accurate interpretation of ground-observed waves and facilitates the use of ground-based wave data in future studies of radiation belt dynamics.

Acknowledgment

No author of a doctoral dissertation could accomplish so much without the help of innumerable people. And despite their innumerable nature, I shall nonetheless list them here.

Above and beyond my expectations, Maria Spasojevic has been an incredible mentor to me during my time at Stanford. Maria possesses a marvelous ability to put details in context and to pick out the occasional relevant bits from my often rambling stream of consciousness. Throughout my time here, Maria has always believed in my capabilities, even when I gave her reasons not to (especially regarding my use of commas). I can think of no greater aspiration for my career than to be as meticulous and insightful a researcher as Maria.

I also owe a debt of gratitude to my dissertation advisor, Umran Inan. Umran has consistently supported me throughout my research, and he possesses an amazing knowledge both of the field and of the mind of a graduate student that is both unparalleled and occasionally disconcerting. I also appreciate the effort and time commitments of Brad Osgood and Phil Scherrer, reader of this thesis and chair of my dissertation committee, respectively.

I am grateful to Don Carpenter for our many interactions and for his historical insight and constant urging to explore outstanding questions in the field. I also thank Don for his consistent interest in my work, even when it diverged into territory with which he was less familiar.

Though there are those who live for research in and of itself, I confess that I would not have had nearly as much fun in the VLF group without the company of my many colleagues and friends throughout the years, including group administrators Shaolan

Min and Helen Niu, as well as Dan Musetescu, Nikolai Lehtinen, Dave Lauben, Brant Carlson, Tim Chevalier, Morris Cohen, Marek Golkowski, Prajwal Kulkarni, Robert Newsome, Ryan Said and David Strauss.

In particular, I must single out Kevin Graf and Forrest Foust, my office mates for the last year of my thesis work. Kevin has been a never-ending source of entertainment, both for better and for worse, and together we have avoided many an hour of research with the help of exotic wind-up toys, an always-changing assortment of devil duckies, and the hallowed weekly “split-split” lunch special. Forrest, though he’ll try to deny it, is one of the most intelligent, diligent, and downright altruistic programmers I have ever known. Forrest wrote the Stanford 3D raytracer and Landau damping code that I use in Chapter 4, which allowed me to perform one of the most interesting studies of this Ph.D. research, and the one of which I am the most proud. Forrest’s never-ending commitment to both supporting his code and helping with questions unrelated to his field is truly an inspiration to me.

Finally, I must thank my family and my wonderful wife, Rachel, without whose love and support I probably still could have gotten this Ph.D., but it certainly wouldn’t have been nearly as much fun.

DANIEL I. GOLDEN
Stanford, California
January 20, 2011

This research was supported by the National Science Foundation under grants ATM-0524805 and ANT-0538627, by NASA under grant NNG04GN01G, and by the Office of Naval Research under awards N00014-09-1-0034 and Z882802. K_p and AE data were obtained from the World Data Center for Geomagnetism, Kyoto. The 10.7-cm solar flux data are provided as a service by the National Research Council of Canada.

Contents

Abstract	v
Acknowledgment	vii
1 Introduction	1
1.1 The Magnetosphere	2
1.1.1 Plasma Regions Within the Magnetosphere	4
1.1.2 ELF/VLF Chorus and Hiss	12
1.1.3 Geomagnetic Disturbances	14
1.2 Ground Measurements of Magnetospherically-Originating Waves	16
1.2.1 Challenges of Ground Measurements	16
1.2.2 Field-Aligned Density Irregularities (Ducts)	17
1.3 Measurements at Palmer Station, Antarctica	20
1.3.1 Palmer System Description	21
1.4 Contributions of this Work	23
2 Scientific Background	25
2.1 The Geomagnetic Coordinate System	25
2.1.1 Dipole Field Model	25
2.1.2 Solar Magnetic Coordinate System	27
2.1.3 IGRF and Tsyganenko Field Models	28
2.2 Wave Propagation in a Magnetized Plasma	29
2.2.1 Whistler-Mode Plasma Waves	30
2.2.2 Wave-Particle Interactions	34

2.3	Properties of Chorus and Hiss	37
2.3.1	Spectral Characterization and Source Locations	38
2.3.2	Role in Maintaining the Radiation Belt Structure	43
2.3.3	Generation Mechanisms	44
3	Diurnal Dependence of Chorus and Hiss	47
3.1	Experimental Methodology	48
3.1.1	Emission Selection Criteria	48
3.1.2	Cumulative Spectrograms	49
3.2	Occurrence Characteristics	51
3.2.1	Local Time and Frequency	51
3.2.2	Occurrence Rates and Correlation with <i>AE</i>	57
3.3	Discussion	59
3.3.1	Chorus as a Source of Hiss	61
3.3.2	Lightning as a Source of Hiss	62
3.4	Summary	65
4	Plasmaspheric Control of Chorus Propagation	66
4.1	Motivation	67
4.2	Experimental Methodology	68
4.2.1	Palmer Emission Database	68
4.2.2	Plasmapause Location Database	69
4.3	Dependence of Chorus Observations on Plasmasphere Extent	71
4.3.1	Choice of <i>AE</i> Metric	71
4.3.2	Chorus Occurrence versus Plasmasphere Extent	72
4.3.3	Chorus Occurrence versus Plasmasphere Extent and <i>AE</i>	75
4.4	Modeling of Chorus Propagation	79
4.4.1	The Stanford VLF 3D Raytracer	79
4.4.2	Raytracing Procedure	83
4.4.3	Chorus Availability Factor	90
4.4.4	Comparison with Observations	95
4.5	Summary	97

5	Automated Emission Detection	100
5.1	Automated Emission Detection	101
5.1.1	Removal of Sferics and Hum	101
5.1.2	Event Detection	108
5.1.3	Event Characterization	112
5.1.4	Construction of the Neural Network Training Set	115
5.1.5	Neural Network Implementation and Training	116
5.1.6	Algorithm Speed	121
5.2	Solar Cycle Variation of Emissions	123
5.2.1	General Trends	123
5.2.2	Yearly and Monthly Variation	125
5.3	Summary	130
6	Summary and Suggestions for Future Work	132
6.1	Summary of Major Results	132
6.2	Suggestions for Future Work	136
A	Statistics for Binomial-Distributed Data	140
A.1	The Central Limit Theorem	141
A.2	The Agresti-Coull Confidence Interval	141
A.3	Hypothesis Testing for Sample Means	143
A.4	Logistic Multiple Regression	144
A.5	Fishing Expeditions: A Statistical Fallacy	146
B	Notable Emissions at Palmer	149
B.1	Chorus and Hiss Progression	149
B.2	Individual Emissions	153

List of Tables

2.1	Magnetospheric ELF/VLF Hiss Varieties	42
4.1	Univariate Model Coefficients	75
4.2	Bivariate Model Coefficients (All Frequencies)	77
5.1	List of Event Characteristics and Units	113

List of Figures

1.1	The Horizontal Geomagnetic Field	3
1.2	The Magnetosphere	5
1.3	Magnetospheric Plasma Regions	6
1.4	Earth-Ionosphere Waveguide Attenuation	9
1.5	EUV Images of the Plasmasphere	10
1.6	Distribution of Plasmasphere Extents	11
1.7	Example Chorus and Hiss Spectrograms	13
1.8	Ducted and Non-ducted Waves	18
1.9	Palmer Station	20
1.10	Palmer Receiver System	22
2.1	Geomagnetic Coordinate System	26
2.2	CGM L-shells on the Earth's Surface	28
2.3	ω — k Diagram of Plasma Waves	31
2.4	Typical Plasma Cutoff Frequencies	32
2.5	Model Landau and Cyclotron Resonant Energies	36
2.6	Source Regions of Chorus and Hiss	39
3.1	Palmer 24-Hour Synoptic Spectrogram	48
3.2	Examples of Emission Types	50
3.3	Cumulative Spectrogram Generation Procedure	51
3.4	Cumulative Spectrograms of Hiss, Chorus, and Chorus with Hiss	52
3.5	Emission Spectra	56
3.6	Emission Cumulative Occurrence Probability	56

3.7	Histograms Showing Dependence of Emissions on AE^\dagger	58
3.8	Cumulative Spectrograms Showing Dependence of Emissions on AE^\dagger	60
3.9	Multiply-Hopping Whistler	64
4.1	Cumulative Spectrogram of Chorus From April–June, 2001	70
4.2	Dependence of L_{PP} on AE	72
4.3	Scatter Plot of Synoptic Epochs With and Without Chorus	73
4.4	Chorus Occurrence Rate Versus L_{PP} via Logistic Regression	76
4.5	Chorus Occurrence Rate Versus L_{PP} and AE via Logistic Regression	78
4.6	Ray Families at 1 kHz, $L_{PP}=2.9$	85
4.7	Ray Families at 4 kHz, $L_{PP}=2.9$	89
4.8	Source Attenuation Plots for $L_{PP}=2.9$	91
4.9	Histogram of Recorded Chorus Amplitudes	93
4.10	Comparison of Model and Observations of Chorus Occurrence versus L_{PP}	94
5.1	Emission Detector Block Diagram	102
5.2	Example of Sferic Removal Procedure	103
5.3	Spectrogram Before and After Noise Removal	107
5.4	Common Types of Detected Broadband Events	110
5.5	Neural Network Block Diagram	118
5.6	Neural Network Confusion Matrices: Noise	120
5.7	Neural Network Confusion Matrices: Emission	122
5.8	Cumulative Spectrograms of Chorus and Hiss Determined by the Au- tomated Emission Detector	124
5.9	Emission Occurrence Rates with Monthly Cadence Over a Solar Cycle	126
5.10	Emission Occurrence Rates Averaged over Years and Months Over a Solar Cycle	127
5.11	Monthly Cumulative Spectrograms of Chorus	129
5.12	Monthly Cumulative Spectrograms of Hiss	130
6.1	Map of Broadband VLF Receiver Sites	137

A.1	Definition of z -score	142
B.1	Chorus Event Progressions	151
B.2	Hiss Event Progressions	152
B.3	Chorus Emissions	154
B.4	Hiss Emissions	155
B.5	Chorus with Hiss Emissions	156
B.6	Multiply-Hopping Whistlers and Hiss	157
B.7	Whistler-Triggered Emissions	158
B.8	Periodic, Quasi-Periodic and Discrete Emissions	159

Chapter 1

Introduction

The Earth’s radiation belts are toroidal regions of geomagnetically trapped energetic ions and electrons that extend from approximately 1000 km altitude out to 8 Earth radii (R_E) from the center of the Earth [*van Allen and Frank, 1959; Vernov and Chudakov, 1960*]. The radiation belts contain significant densities of relativistic particles with energies of up to one million electron volts (1 MeV), and these energetic particles pose a significant hazard to space-borne technological systems and astronauts in the near-Earth space environment [e.g., *Baker, 2000*]. A complete understanding of the fundamental processes that contribute to the spatial and temporal variability of the structure of the radiation belts is thus needed both for scientific and practical reasons.

Many physical processes control the dynamic evolution of fluxes in the radiation belts (see recent reviews by *Shprits et al. [2008a,b]*). One process that is believed to be important for both the source and loss of energetic electrons is cyclotron resonant wave-particle interactions involving whistler-mode plasma waves. For example, it is believed that “plasmaspheric hiss,” a naturally-occurring electromagnetic whistler-mode wave, is a major driver of electron losses within the so-called slot region [e.g., *Lyons et al., 1972; Lyons and Thorne, 1973; Abel and Thorne, 1998*]. Another whistler-mode emission known as “chorus” is believed to be capable of both accelerating medium energy electrons up to relativistic energies, thereby providing a source mechanism for the belts [e.g., *Meredith et al., 2002; Horne et al., 2003, 2005*],

as well as scattering electrons out of the radiation belts over a wide range of energy, thus driving their loss [e.g., [Lorentzen et al., 2001](#); [O’Brien et al., 2003](#); [Thorne et al., 2005](#); [Shprits et al., 2006](#)]. Understanding the relative role of whistler-mode waves in controlling the global evolution of the electron radiation belts is a major outstanding problem in magnetospheric physics.

Ground-based electromagnetic wave measurements in the extremely low frequency and very low frequency (ELF/VLF, 0.3-30 kHz) ranges provide large databases of chorus and hiss emissions. However, interpretation of these measurements is confounded by the rather complicated propagation path and attenuation profile of the waves as they travel from their source regions in the magnetosphere to the measurement locations on the ground. The goal of this thesis is to improve the ability to differentiate between source and propagation effects in interpreting ground-based measurements of chorus and hiss, to use these ground measurements to generate a large statistical database, and to use this database to explore long-term trends of the emissions. This work has led to a more accurate interpretation of ground-based observations of magnetospherically-generated waves and will facilitate the use of ground-based wave data in future studies of radiation belt dynamics.

1.1 The Magnetosphere

The Earth’s intrinsic magnetic field is believed to be generated by the fluid motions of the liquid portions of the Earth’s metallic-like core [[Chapman and Bartels, 1940](#); [Gubbins, 1981](#)]. The Earth’s magnetic poles, defined as the points on the surface of the Earth at which the horizontal component of the geomagnetic field goes to zero, are located approximately 11° from the geographic poles and can be clearly seen as local minima of horizontal field amplitude in the map of horizontal magnetic field intensity in Figure 1.1. The geomagnetic field lines are pointed vertically upwards at the southern magnetic pole and vertically downwards at the northern magnetic pole; thus, by convention, the southern magnetic pole is actually a magnetic *north* pole, and vice versa.

To first order, at radial distances of less than $\sim 4 R_E$, the Earth’s magnetic field

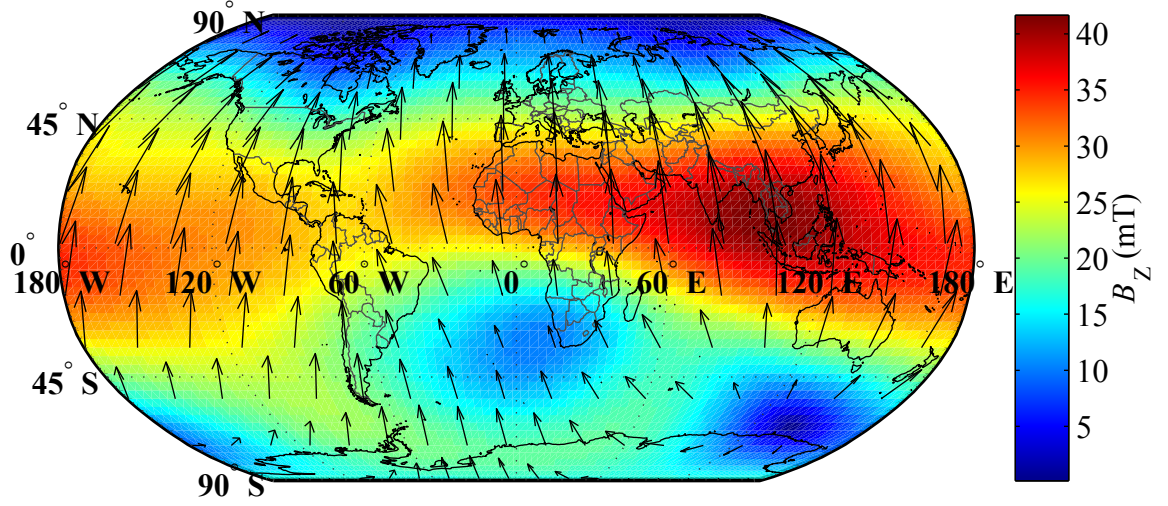


Figure 1.1: A map of magnitude and direction of the horizontal component of the Earth’s magnetic field. Arrows point in the same direction that a magnetic compass would in that location. The magnetic poles can be seen as the minima of horizontal field intensity in northern Canada and south of Australia. The depression in field intensity southwest of Africa is related to the south-Atlantic anomaly.

may be approximated with a centered, tilted dipole. In this case, a given point in space is described by three coordinates: L shell, λ and MLT. Under the dipole approximation, the L shell defines a set of field lines which intersect the geomagnetic equator some number of Earth radii from the center of the Earth; e.g., $L=4$ indicates the set of field lines which intersect the geomagnetic equator at a radial distance of $4 R_E$. Geomagnetic latitude (λ) is measured from the geomagnetic equator, and MLT is the magnetic equivalent of local time, measured in hours. These coordinates are discussed in more detail in Section 2.1.

At higher altitudes, the shape of the geomagnetic field is distorted by the solar wind flow [Neugebauer and Snyder, 1966] past the Earth. The region of space over which the Earth’s magnetic field is the dominant force on charged particles, particularly when compared to the interplanetary magnetic field (IMF) of solar origin, is known as the magnetosphere. Because any movement of plasma perpendicular to field lines has the effect of “dragging” the field lines along with the plasma [e.g., Bittencourt, 2004, Sec. 12.4], the flowing solar wind causes the characteristic bullet

shape of the magnetosphere, as shown in Figure 1.2. The magnetosphere stretches from $\sim 10 R_E$ on the sunward side to more than $100 R_E$ on the anti-sunward side of the Earth. The boundary of the magnetosphere, where the outward force of the compressed geomagnetic field balances with the force of the solar wind plasma pressure, is known as the magnetopause. Because charged particles move much more freely parallel to a magnetic field than perpendicular to it, the magnetosphere buffers the region of near-Earth space from the full effects of highly energetic solar wind. Within the magnetosphere is a rich and complicated system of flowing and trapped plasmas, which generate and interact with a wide variety of electromagnetic and electrostatic plasma wave phenomena.

1.1.1 Plasma Regions Within the Magnetosphere

Within the magnetosphere, several distinct populations of plasmas exist, as shown in the cartoon in Figure 1.3. Cold electrons (energies $E \lesssim 10$ electron volts, or eV) in the ionosphere appear in sufficient densities ($N_e > 10^4 \text{ cm}^{-3}$) to attenuate waves due to particle collisions. The cold electron density in the plasmasphere is also relatively high ($N_e \sim 10^3 \text{ cm}^{-3}$), and the plasmasphere is primarily responsible for determining the refractive index and the propagation direction of waves. The densities of hot electrons ($100 \text{ eV} \lesssim E \lesssim 1 \text{ MeV}$) in the radiation belts are lower ($N_e < 1 \text{ cm}^{-3}$) and hot electrons are responsible for reducing the amplitude of waves via Landau damping at lower energies and amplification and/or generation of those same waves at higher energies through cyclotron resonance (Section 2.2.2).

Ionosphere

The ionosphere is the lowest-altitude region of plasma in near-Earth space and consists of molecules from the Earth's neutral atmosphere which have become ionized by short-wavelength electromagnetic radiation from the sun [*Appleton and Barnett, 1925; Bauer, 1973; Bilitza and Reinisch, 2008*]. Beginning somewhere between 50 and 70 km in altitude (depending on factors such as time of day and geographic latitude), the ionospheric density peaks with electron densities of $\sim 10^5 \text{ cm}^{-3}$ (night) or $\sim 10^6 \text{ cm}^{-3}$

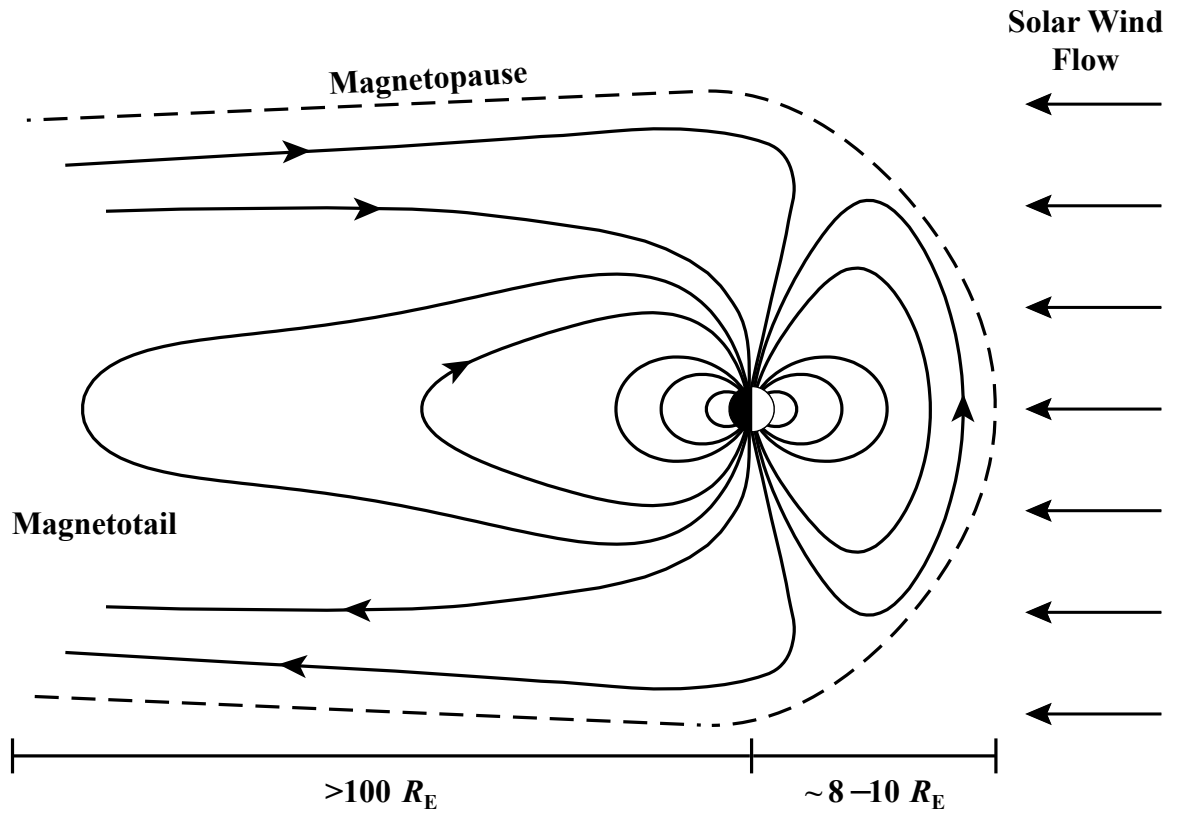


Figure 1.2: The field lines of the Earth's magnetic field are distorted by pressure from the solar wind. This distortion results in the characteristic bullet shape of the magnetosphere, shown in the meridional plane with the sun to the right. Distortion is minimal closer to the Earth, where the field can be accurately modeled as a dipole. Figure from [Spasojević \[2003, Fig. 1.2\]](#).

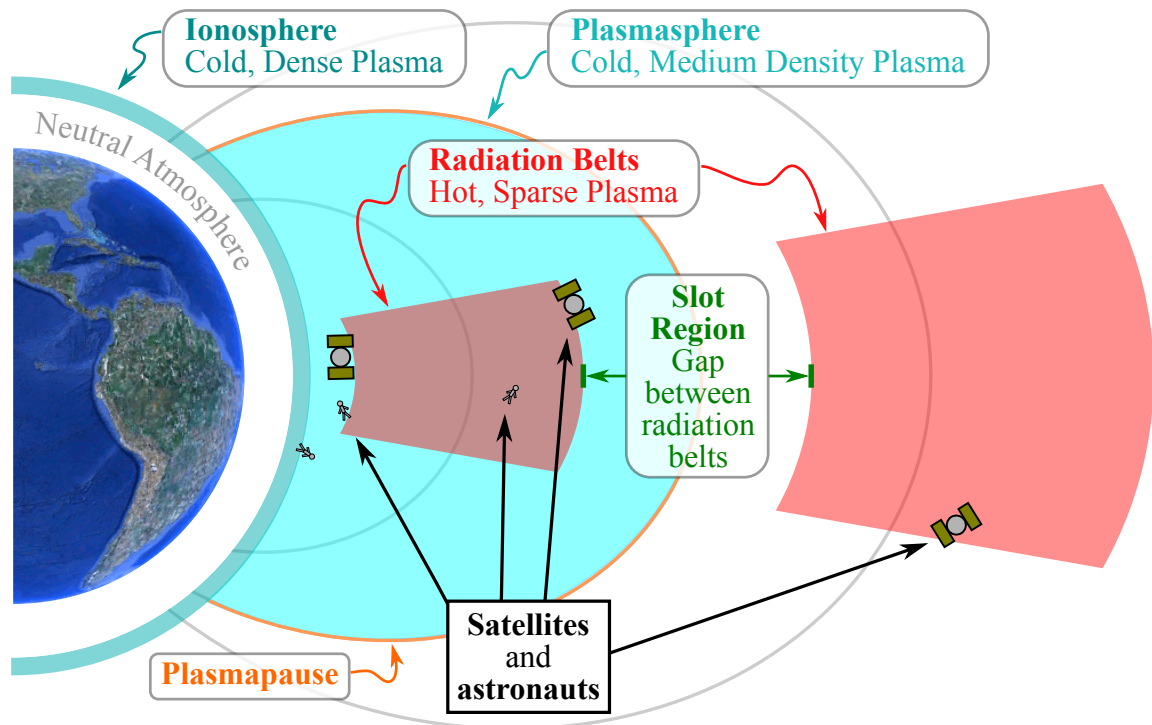


Figure 1.3: A cartoon showing several distinct plasma regions in the Earth's magnetosphere (not to scale). The cold plasma in the ionosphere and plasmasphere controls the propagation of whistler-mode plasma waves, while the hot plasma of the radiation belts/ring current contribute to wave growth and damping.

(day) at ~ 350 km. The ionospheric density decreases gradually at higher altitudes and there is no distinct boundary between the ionosphere and the greater magnetosphere. With peak energies of less than 1 eV, the constituent electrons of the ionosphere are usually considered to be “cold” ($E \sim 0$ eV).

The ionosphere influences ground observations of magnetospheric waves in two ways. The first is via attenuation of the waves. All magnetospheric waves must pass completely through the ionosphere before reaching the ground, and therefore all ground observations of magnetospheric waves are influenced by ionospheric absorption. The primary loss mechanism is collisions between electrons in the lower ionosphere with neutral molecules, though there is also a contribution from Coulomb collisions (interactions between electrons and other electrons or ions) in the upper ionosphere [Helliwell, 1965, Sec. 3.8]. Overall, at the middle geomagnetic latitudes ($\sim 50^\circ$) and frequencies (~ 2 kHz) of interest here, trans-ionospheric absorption is expected to be on the order of ~ 10 dB during the local day and ~ 2 dB during the night [Helliwell, 1965, Fig. 3-35]. Absorption is significantly higher during local day due to the corresponding increased solar radiation and resulting increased ionospheric density.

Once magnetospheric waves have penetrated through the ionosphere, they propagate in the Earth-ionosphere waveguide, a lossy parallel plate waveguide formed by the surface of the Earth and the ionosphere. Once in the waveguide, waves convert into free-space waveguide modes and are attenuated via geometrical spreading and losses at the boundaries. Losses are primarily due to the finite conductivity of the walls of the waveguide, both in the ionosphere and in either seawater or the Earth’s crust depending on the propagation path.

Tsuruda *et al.* [1982] reported an attenuation rate of 7 dB/100 km for 2–3 kHz waves propagating in the Earth-ionosphere waveguide based on multi-station observations of Siple transmitter signals in the conjugate region. These observational results can be compared with modeling results using the full wave method of Lehtinen and Inan [2008, 2009] shown in Figure 1.4. The full wave method is a technique for finding a steady state solution of waves at a single frequency in a stratified medium such as the ionosphere. The modeling begins with a wave packet distributed as a Gaussian

in width (horizontal to the ground) with a radius of 20 km, injected with vertical (downward) wavenormals at 140 km altitude. The modeled results show that the attenuation rate of waves is highest close to the ionospheric exit point, before the establishment of distinct waveguide modes. In this region near the injection point, the attenuation rate may be as high as 7 dB/100 km. Once modes are resolved, beyond 500 km away from the exit point, the attenuation rate is significantly lower, on the order of ~ 1 dB/100 km. However, the wave is already attenuated significantly at this point, down 45 dB from its original amplitude above the ionosphere. Note that these numbers are for local night, and the model assumes a flat earth. Attenuation during local day is somewhat higher due to increased ionospheric losses. In a spherical Earth, there is a small focusing effect at large distances, which is partially balanced by a small increased loss from the changing reflection angle of the wave with respect to the waveguide walls over the course of its propagation.

Plasmasphere

Beyond the ionosphere lies the plasmasphere, a region of cold ($E < 1$ eV) plasma which extends in a primarily field-aligned toroid around the earth. The constituent plasma of the plasmasphere is fed by the ionosphere [Lemaire, 1989], and heating processes such as wave-particle interactions and Coulomb collisions slightly elevate the energies of its constituent electrons by on average a factor of 3 [Comfort, 1986; Newberry *et al.*, 1989]. The plasma density in the plasmasphere is one or more orders of magnitude lower than that in the ionosphere, on the order of 10^3 – 10^4 cm $^{-3}$. The boundary of the plasmasphere is known as the plasmapause, and the plasma density drops precipitously across this boundary, often by more than an order of magnitude over a distance of only $0.1 R_E$ [Carpenter and Anderson, 1992].

The plasmasphere is highly dynamic, and its structure is strongly influenced by geomagnetic activity. In particular, interactions between the geomagnetic field and the IMF during geomagnetic storms drive a large-scale electric field which transports plasmaspheric plasma sunward, resulting in an “erosion” of the bulk plasmasphere and the development of a plasmaspheric plume [Carpenter, 1970] on the dusk side.

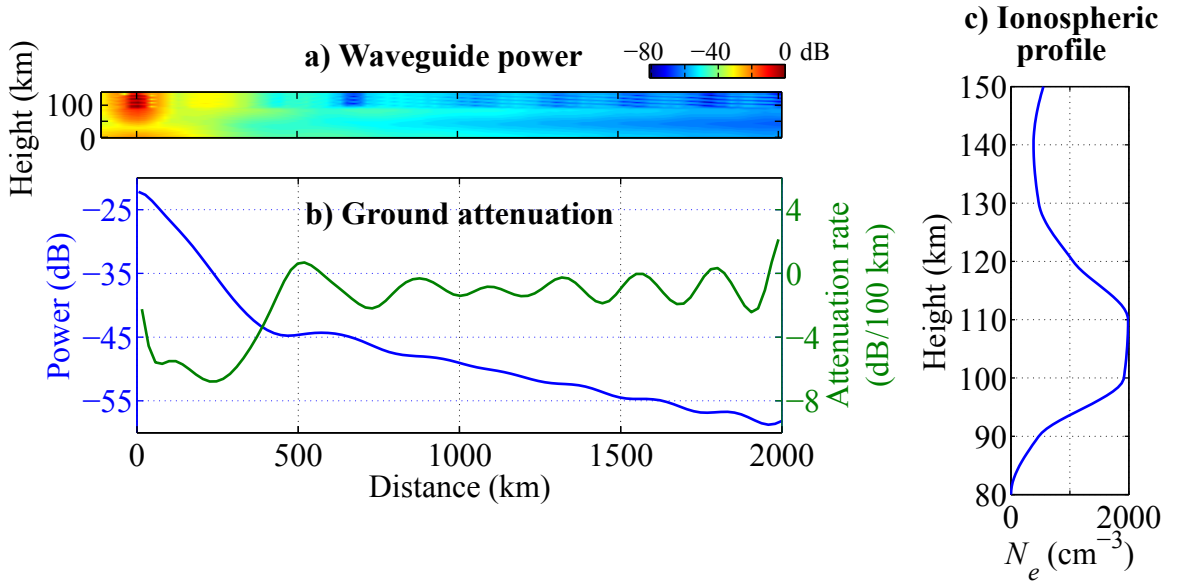


Figure 1.4: Modeled attenuation of a 2 kHz wave in the Earth-ionosphere waveguide determined using the full wave method of [Lehtinen and Inan \[2008, 2009\]](#). (a) A two-dimensional slice in height and distance showing the power distribution up to 2000 km from the injection point at 140 km altitude. (b) A plot of power as would be received on the ground with respect to peak injected power (blue) in dB, and the attenuation rate per unit distance (green) in dB/100 km. (c) The ionospheric profile used for this model, a summer night time model for Palmer Station's geographical location (64.77°S, 64.05°W).

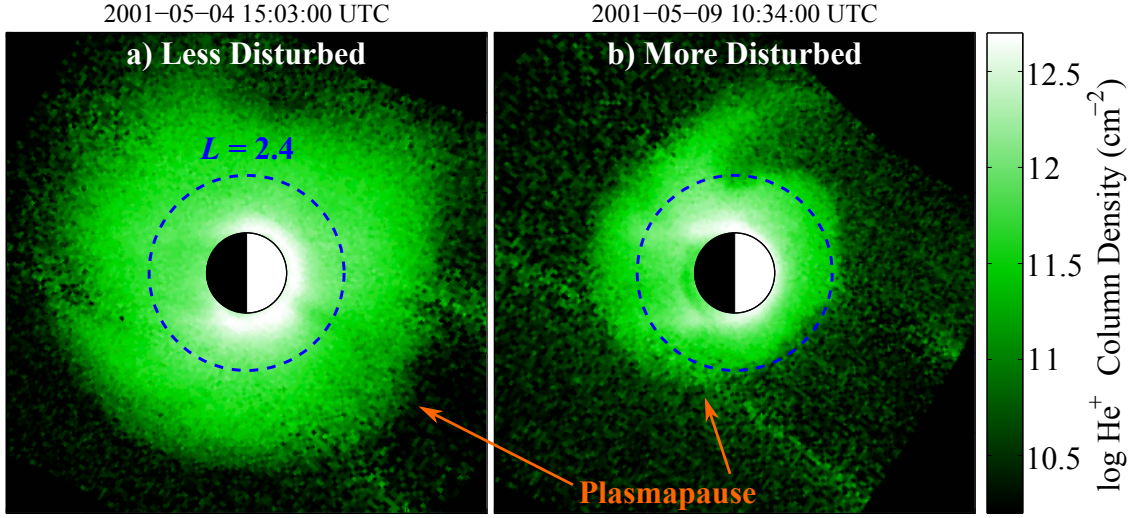


Figure 1.5: Extreme ultraviolet images of the column density of plasmaspheric He^+ show how the extent of the plasmasphere changes with changing geomagnetic conditions. (a) Under less disturbed conditions, the plasmasphere expands due to slow filling from the ionosphere. (b) Under disturbed conditions, enhanced magnetospheric convection erodes the plasmasphere so that the plasmapause moves to low L shells. Images are shown in the geomagnetic equatorial plane with the north geomagnetic pole pointing out of the page. The L shell of Palmer Station ($L = 2.4$) is indicated with the blue dashed circle.

These features can be seen in Figure 1.5, which shows images of integrated He^+ column density from the extreme ultraviolet (EUV) instrument [Sandel *et al.*, 2000] on board the IMAGE satellite [Burch, 2000] during both quiet and disturbed geomagnetic conditions. Although the He^+ distribution is only a minority constituent of the ionic composition of the plasmasphere, its distribution is an effective proxy for the plasmaspheric electron distribution [Goldstein *et al.*, 2003].

An example of the variability of plasmasphere extent (i.e., the L shell of the plasmapause, L_{PP}) is illustrated in Figure 1.6, which shows a histogram of 1600 samples of L_{PP} taken at the MLT of Palmer Station (UTC $- 4$ hrs) using IMAGE EUV data from April–June, 2001. Due to the often complicated structure of the plume in the dusk sector, only data from the midnight, dawn and noon sectors are included in the statistics. Geomagnetic conditions during this time are representative of 2001 as a whole, which in turn was a moderately disturbed year (see Figure 5.10,

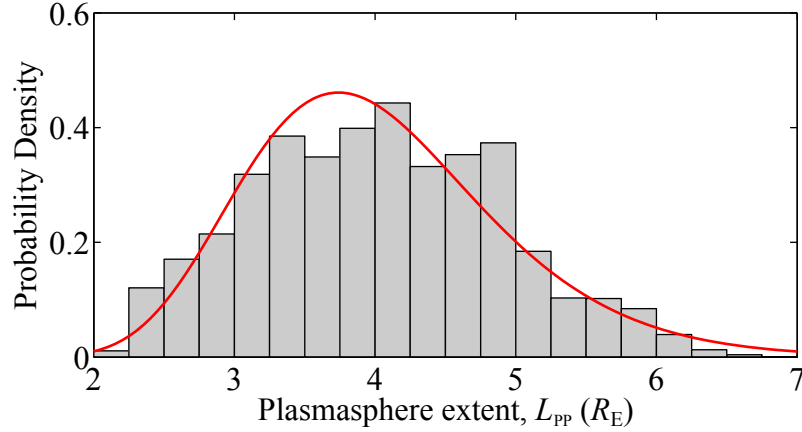


Figure 1.6: Histogram of plasmasphere extent (L_{PP}) at Palmer’s MLT (UTC – 4 hrs) for three months from April–June, 2001. The dusk sector ($15 < \text{MLT} < 21$) is excluded due to the complicated plume structure that often appears there. The fitted distribution (red line) is lognormal with $\mu = 4.0 R_E$ and $\sigma = 0.88 R_E$.

lower-left). As a result of the higher geomagnetic disturbance level, the values of L_{PP} in Figure 1.6 are slightly lower than typical. The average value of L_{PP} during this period is $4 R_E$, but it is highly variable, reaching down to nearly $2 R_E$ during great geomagnetic disturbances and out to $6 R_E$ and beyond during quiet periods. During extended quiet periods, the plasmopause becomes less distinct and may not exist in any identifiable fashion, such as in the top portion (dusk sector) of Figure 1.5a.

Wave propagation can be dramatically influenced by the steep density gradient at the plasmopause. Generally, the boundary acts like an obstacle, preventing waves which originate outside the plasmasphere from entering it and preventing waves which originate within the plasmasphere from leaving. However, under the right circumstances, this steep density gradient may have the effect of causing a rapid rotation of wavenormal angles (k -vectors), allowing waves to cross the plasmopause boundary while undergoing a magnetospheric reflection, i.e., a rapid reversal of the direction of the k -vector. The manner in which the plasmasphere extent controls access of chorus waves to the ground, a process which requires traversal of this plasmaspheric boundary by the waves, is explored in Chapter 4.

Radiation Belts and Ring Current

The electron radiation belts [*van Allen and Frank*, 1959; *Vernov and Chudakov*, 1960] consist of two distinct regions of trapped energetic electrons separated by a local minimum of particle flux known as the “slot region.” Energetic electrons extend out to $L \sim 7$ in the outer belt and down to $L \sim 1.25$ in the inner belt, with a slot centered at $L \sim 2.5$ [*Walt*, 1994, Fig. 5.15]. The high energies of radiation belt particles allow them to interact in many significant ways with electromagnetic waves, transferring energy to and from the waves depending on the characteristics of the local particle distributions (see Section 2.2.2).

The effects of enhanced radiation belt fluxes on satellites are of increasing interest in modern times as the number of active satellites, and correspondingly the number of satellites experiencing serious anomalies continues to increase. These anomalies are likely a result of interactions with the radiation belts or other aspects of space weather [*Baker*, 2000]. As the number of manned and unmanned near-Earth space missions increases in the future, it will prove increasingly vital to be able to accurately quantify the factors that determine the structure of the radiation belts.

Contrary to the cold ionospheric and plasmaspheric plasmas which are primarily sensitive to electric field-driven drifts, the hot particles of the radiation belts experience longitudinal gradient and curvature drifts due to the spatially-varying geomagnetic field. Ions and electrons drift in opposite directions; electrons drift eastwards while ions drift westwards, which results in a net westward current known as the ring current. Due to their greater energy density, ions are dominant over electrons in contributing to the net current [*Daglis et al.*, 1999].

1.1.2 ELF/VLF Chorus and Hiss

The magnetosphere is host to a variety of electromagnetic plasma waves [e.g., *Sonwalkar*, 1995, Sec. 4.2]. Chorus and hiss are two such types of whistler-mode waves (see Section 2.3 for more details) that are generated in the magnetosphere at frequencies in the range 0.1–10 kHz, a subset of the ELF/VLF range of 0.3–30 kHz. This frequency range has the interesting property that it lies comfortably within the

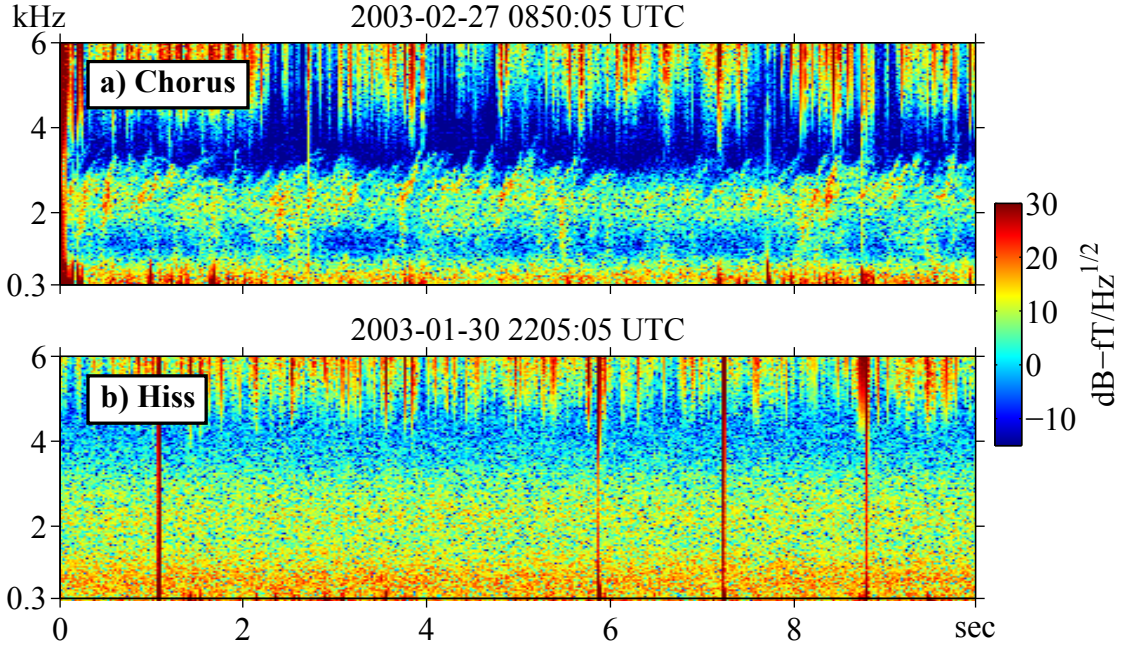


Figure 1.7: Spectrograms of chorus and hiss emissions received at Palmer Station, Antarctica. (a) Chorus is characterized by a series of closely-spaced, usually rising tones while (b) hiss consists of an incoherent band-limited noise-like signal.

typical range of human hearing, of 0.02–20 kHz. A simple system consisting of a long antenna hooked directly up to an audio transducer, without any sort of signal processing equipment, is sufficient to detect these magnetospheric waves [Helliwell, 1965, Ch. 1.1]. Early observations of the waves were carried out with just such systems for audio analysis of the signals, which also explains how the emissions got their names. Chorus, sounding like a “rookery heard from a distance,” was named after birds’ dawn chorus [Storey, 1953], while hiss receives its onomatopoetic name from the incoherent “hissy” sound that it makes when played aloud.

Modern analysis involves far more complex receivers and signal processing, and the canonical method of characterizing emissions is via a “spectrogram,” which is a frequency versus time plot showing the evolution of the frequency content of a signal with time. Figure 1.7 shows spectrograms of chorus and hiss emissions as received at Palmer Station, Antarctica in 2003. The color of the spectrogram indicates the power spectral density of the signal in dB with respect to 1 fT/ $\sqrt{\text{Hz}}$.

Chorus and hiss emissions are ELF/VLF magnetospheric waves which (a) are naturally generated in the magnetosphere, (b) significantly contribute to the structure of the radiation belts and (c) are able to penetrate to the ground at mid-geomagnetic latitudes and be received there. It is for these reasons that chorus and hiss are the focal topic of this thesis.

1.1.3 Geomagnetic Disturbances

The magnetosphere is highly sensitive to variations in the solar wind and its embedded magnetic field, the IMF [[Murayama, 1982](#)]. The primary process by which energy, mass and momentum is transferred from the solar wind to the magnetosphere is known as magnetic field reconnection. Reconnection occurs at the subsolar magnetopause when the IMF has a component that is directed opposite to that of the main field of the Earth, i.e., the IMF has a significant southward component [[Dungey, 1961](#)]. Dayside reconnection allows for solar wind entry into the magnetosphere, but more importantly it results in the buildup of magnetic flux in the magnetotail, which is subsequently released as part of the substorm cycle. This release of flux drives a large-scale electric field across the magnetosphere, which transports particles trapped in the magnetotail into the inner magnetosphere leading to the buildup of the ring current.

Geomagnetic Storms and Substorms

Substorms are the most common type of geomagnetic disturbance. Substorms consist of global reconfigurations of the magnetosphere involving the storage of solar wind energy in the magnetotail and its abrupt release in the form of particle heating and kinetic energy. The growth phase of a substorm is initiated when the IMF turns southward, and the most visible manifestation of substorms is the intensification of the visible aurora at high latitudes that occurs 30-90 minutes later during substorm onset. The aurora is caused by magnetospheric particles colliding with constituents in the Earth's atmosphere (a process known as "particle precipitation").

Substorms also result in increased fluxes of energetic particles in the inner magnetosphere. These particle distributions tend to be anisotropic, leading to the growth of plasma waves such as chorus and hiss, whose presence has long been known to correlate with geomagnetic activity [e.g., [Tsurutani and Smith, 1974](#); [Burtis and Hellwell, 1976](#); [Meredith et al., 2001, 2004](#)].

When the IMF retains a southward component for an extended period of time, a geomagnetic storm may develop. During this prolonged period of interaction between the solar wind and the magnetosphere, the gradual build up of energetic particle fluxes causes increasingly intense aurora, magnetospheric wave generation, plasmaspheric erosion, and an increase in intensity of magnetospheric current systems. The increased magnetospheric currents can have drastic negative consequences for radio communications, terrestrial power distribution systems, and other aspects of terrestrial life [e.g., [Cole, 2003](#)].

Geomagnetic Indices

Several geomagnetic indices have been devised to track different aspects of the bulk geomagnetic activity. These indices are all based on measurements of the geomagnetic field on the surface of the Earth using magnetometers, which measure deflections in the strength and direction of the Earth's main field that result from large-scale ionospheric and magnetospheric current systems.

The K_p index [[Bartels et al., 1939](#)] is the most widely used geomagnetic index. K_p is derived from measurements of 12 worldwide mid-latitude magnetometer stations between 48° and 63° geomagnetic latitude. K_p is given on a quasi-logarithmic scale in discrete intervals of the form 0_\circ , $0+$, $1-$, \dots , $9-$, 9_\circ . K_p is meant to be used as an indicator of the general level of geomagnetic activity from the solar wind, and does not attempt to separate the effects of the many different current systems which affect its measurements.

The AE (auroral electrojet) index [[Davis and Sugiura, 1966](#)] is calculated using a series of high latitude stations between 62.5° and 71.6° geomagnetic latitude. As its name implies, AE is intended to measure the intensity of the auroral electrojet, a current system that increases in intensity during substorms. Substorms result in the

rapid injection of energetic electrons in the range of a few to a few hundred keV into the inner magnetosphere. Since electrons in this energy range are believed to be the source of chorus and hiss emissions, the *AE* is the preferred index for studies of these emissions [e.g., [Smith et al., 1999](#); [Meredith et al., 2001, 2004](#)].

The *Dst* index [[Sugiura, 1964](#)] is a low-latitude index which is used as a measurement of large-scale variations in the ring current. *Dst* is only capable of measuring very large changes in the ring current intensity, such as those which would be produced by geomagnetic storms, and the response of *Dst* to the individual substorm injections of particles which give rise to chorus and hiss is fairly low. As a result, *Dst* is not an appropriate index for studies of chorus and hiss.

1.2 Ground Measurements of Magnetospherically-Originating Waves

1.2.1 Challenges of Ground Measurements

When compared to in situ space-based measurements, ground-based measurements have several advantages, such as the ability to consistently observe a small range of *L* shells, significantly lower construction and operating costs, and high data rates. However, ground stations are intrinsically limited to sampling the portion of magnetospheric waves that are able to propagate to low altitudes and penetrate through the ionosphere [e.g., [Sonwalkar, 1995](#), pp. 424-425]. These measurable waves include either waves that have propagated such that their wavenormals are within the transmission cone at the ionospheric boundary [[Helliwell, 1965](#), Sec. 3.7] or waves that have scattered from low-altitude meter-scale density irregularities [e.g., [Sonwalkar and Harikumar, 2000](#)]. Thus, not all types of waves observed in space are observable on the ground, an important factor to keep in mind when interpreting ground observations.

1.2.2 Field-Aligned Density Irregularities (Ducts)

In a smooth magnetosphere, magnetic field lines serve as crude guiding structures for whistler-mode waves, preferentially guiding the waves in the direction of the ambient magnetic field. The result is that the paths that these waves take in the magnetosphere tend to be nearly field-aligned. However, in a smooth magnetosphere, this guiding effect is not sufficient on its own to allow a wave which has originated on the ground to travel out into the magnetosphere and return again to the Earth's surface; instead, such waves magnetospherically reflect at high altitudes and remain in the magnetosphere until they eventually dissipate [Kimura, 1966], as illustrated in Figure 1.8a.

Despite this tendency for waves in a smooth magnetosphere to magnetospherically reflect away from the ground, impulses from terrestrial lightning have long been observed to propagate from the ground into the magnetosphere and return to the ground in the conjugate hemisphere [Helliwell, 1965, Ch. 2]. The returned signals are known as “whistlers,” after their characteristic spectrum which, when played through a speaker, sounds like a declining whistling tone as a result of dispersion in the magnetosphere. There is therefore a need to explain the method by which these signals are able to return to Earth when the guiding effect of a smooth magnetosphere is insufficient to allow the signals to do so.

The prevailing theory is that whistlers propagate within field-aligned density irregularities known as ducts [e.g., Helliwell, 1965, Sec. 3.6]. This theory states that ducts, which may be either density enhancements or depletions, constrain waves to a given field line and allow them to return to the ground. Ducts are believed to permeate the magnetosphere, appearing, disappearing and moving in L shell as conditions change. Because ducts, though plentiful, occupy a very small percentage of the total magnetospheric volume, they are difficult to observe directly with in situ satellite observations of electron density. However, remote sounding measurements by Carpenter *et al.* [2002] using the radio plasma imager (RPI) instrument on the IMAGE satellite within the magnetosphere were consistent with scattering from, partial reflection from, and propagation along ducts both inside and outside the plasmapause. The work of Carpenter *et al.* [2002] therefore strengthens the theory that these ducts are

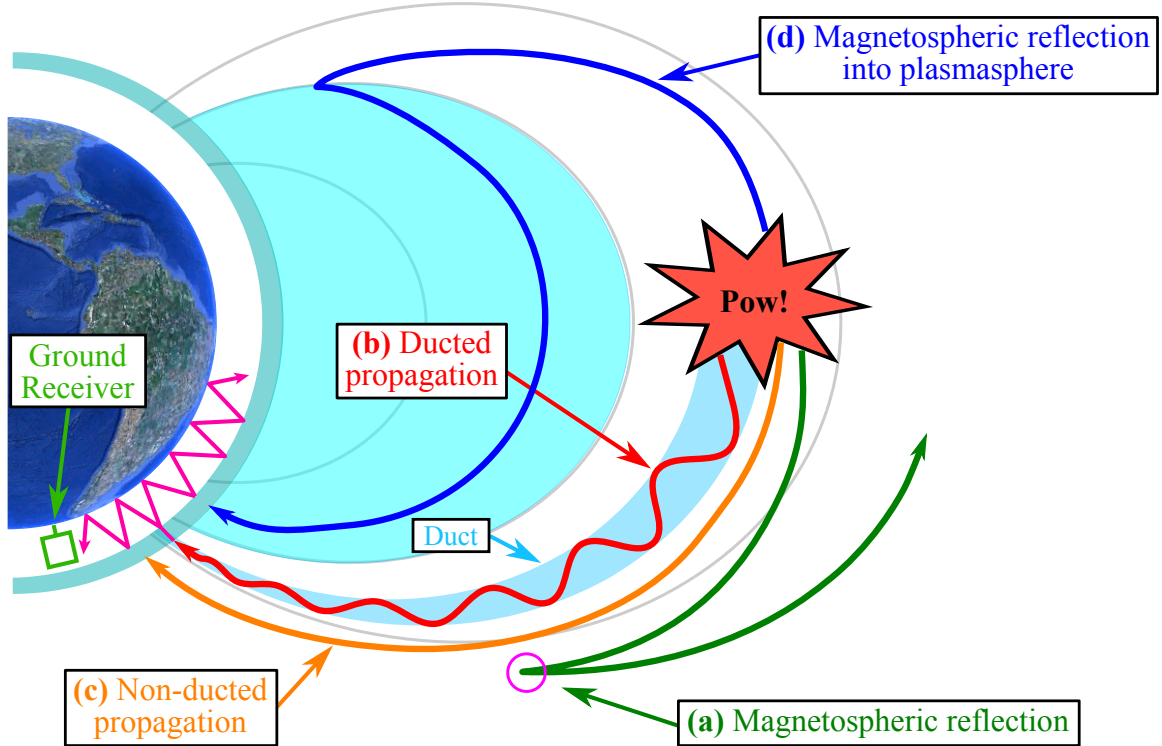


Figure 1.8: Previously, it was believed that (a) non-ducted emissions would magnetospherically reflect away from the Earth at high latitudes and that therefore (b) all magnetospheric emissions which were observed on the ground were ducted. (c) We show in Chapter 4 that, in fact, the dominant chorus emissions received on the ground at mid-latitudes may be non-ducted, and may arrive on the ground either via the direct path or via (d) magnetospheric reflection into the plasmasphere.

prevalent within the magnetosphere.

Based on the theory of ducted whistlers, past researchers tended to assume that observations of *all* types of emissions on the ground, including chorus and hiss, were made possible only by virtue of their having been ducted, a paradigm illustrated in Figure 1.8b. This belief was buoyed by the fact that chorus-like noise bursts were occasionally observed to be triggered [Carpenter *et al.*, 1975] or damped [Gail and Carpenter, 1984] by whistlers. This observation in turn implied that the chorus and whistlers resided in the same duct, consistent with the theory that ground-observed chorus was also ducted.

However, the fundamental difference between chorus or hiss and whistlers is in their source locations. Because whistlers originate on the ground, Snell’s law dictates that the large difference in refractive index between free space and the ionosphere requires that whistlers have near-vertical wavenormals upon their entrance into the ionosphere. Chorus and hiss, however, are generated in the magnetosphere, and have no such obvious constraint on their initial wavenormals. As a result, it is not obvious that the requirement of ducting for observations of ground-originating whistlers also applies to all magnetosphere-originating chorus and hiss.

Previous authors have explored the possibility that chorus received on the ground is non-ducted. A raytracing study by Chum and Santolík [2005] showed that chorus waves with a certain range of initial wavenormal angles could propagate to low altitudes and possibly to the ground, as illustrated in Figure 1.8c. This result was replicated by another raytracing study by Bortnik *et al.* [2007b]. Golkowski and Inan [2008] made multi-station measurements of chorus on the ground and observed emissions with both singular exit points and multiple exit points. The multiple exit point chorus was interpreted as having defocused in the magnetosphere due to its non-ducted propagation. We present a study in Chapter 4 which concludes that, in contrast to previous expectations, most chorus observed on the ground at mid-latitudes is likely to be non-ducted and may propagate to the ground either via the direct path shown in Figure 1.8c or via magnetospheric reflection into the plasmasphere as in Figure 1.8d.

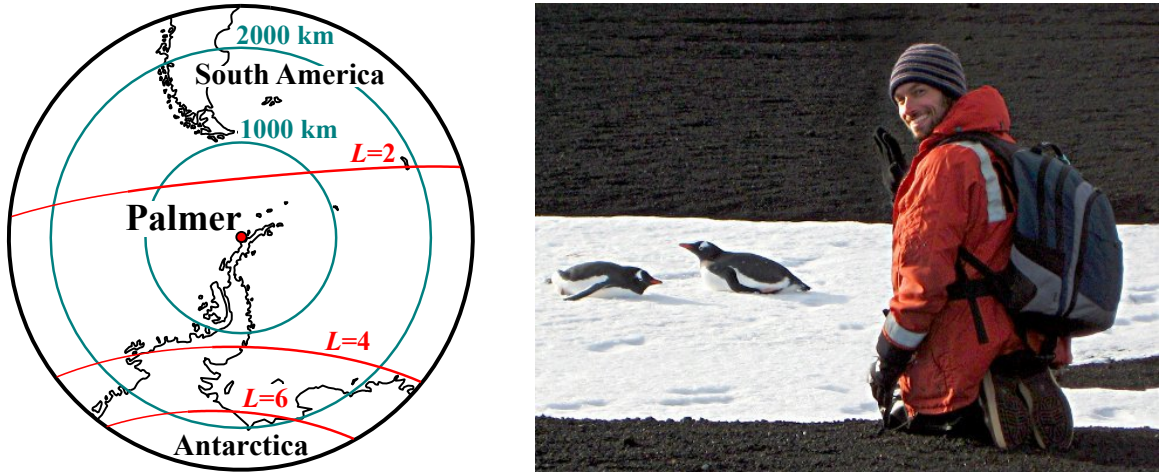


Figure 1.9: (Left) A map of Palmer Station in relation to nearby L shells. (Right) The author with wildlife at Deception Island, en route to Palmer from Punta Arenas, Chile, on 26 March, 2009.

1.3 Measurements at Palmer Station, Antarctica

This thesis is based primarily on data recorded on the ground with Stanford University’s ELF/VLF broadband receiver at Palmer Station, Antarctica. Palmer Station is located on Anvers Island, near the tip of the Antarctic peninsula, at 64.77°S , 64.05°W , with IGRF geomagnetic parameters of $L=2.4$, $\Lambda=50^{\circ}\text{S}$ invariant latitude, and magnetic local time (MLT) = UTC $- 4.0$ hrs at 100 km altitude (see Section 2.1 for a detailed discussion of geomagnetic coordinate systems). Figure 1.9 shows a map of the station’s location with respect to nearby L shells, along with a photograph of the author while en route to Palmer.

Palmer Station is an excellent vantage point from which to observe chorus and hiss emissions. Palmer is located thousands of kilometers from the nearest city, which means that electromagnetic interference from power lines and other anthropogenic radio sources is minimal. Interference is further reduced by the location of the antenna on the Anvers island glacier, over 1 km from the main station. This results in a very high signal to noise ratio (SNR) for observed emissions. In addition, as a result of its mid to low-latitude magnetic location at $L=2.4$, Palmer is capable of observing copious amounts of both chorus and hiss emissions.

1.3.1 Palmer System Description

A block diagram of the ELF/VLF receiver at Palmer is illustrated in Figure 1.10 along with associated images of the receiver components. The magnetic component of electromagnetic waves are received via two orthogonal, 18-m base, triangular cross-loop wire antennas which are located approximately 1400 m East of the main station. A preamplifier adjacent to the antenna amplifies the signal before it is sent through ~ 1500 m of signal cable down to the line receiver in the main station. The line receiver applies signal conditioning to the analog signal before sending it to a desktop computer. Analog-to-digital (A/D) conversion is performed with an add-on signal processing card within the computer. Precise timing of the A/D conversion is accomplished via a clock signal from an external GPS receiver.

The Palmer receiver records broadband ELF/VLF data at 100 kilosamples per second with approximately 96 dB of dynamic range. The analyses of this thesis use the North/South channel exclusively, it being the less noisy of the two channels due to the fact that its viewing direction is orthogonal to the main station. This has the additional effect of focusing Palmer's viewing area more tightly to its magnetic meridian than if both channels were used. Data products used are 10-second broadband data files, beginning every 15 minutes at 5, 20, 35 and 50 minutes past the hour, 24 hours per day. The start time of a data record is referred to as a "synoptic epoch."

In April 2005, the Palmer antenna was moved to its present location from a location approximately 500 m nearer to the station. This move was both to mitigate station noise and to increase the structural stability of the antenna platform by erecting it on a more level section of the glacier. After the antenna move, the net amplitude of signals received by the antenna decreased by approximately 3 dB due to the increased cable length.

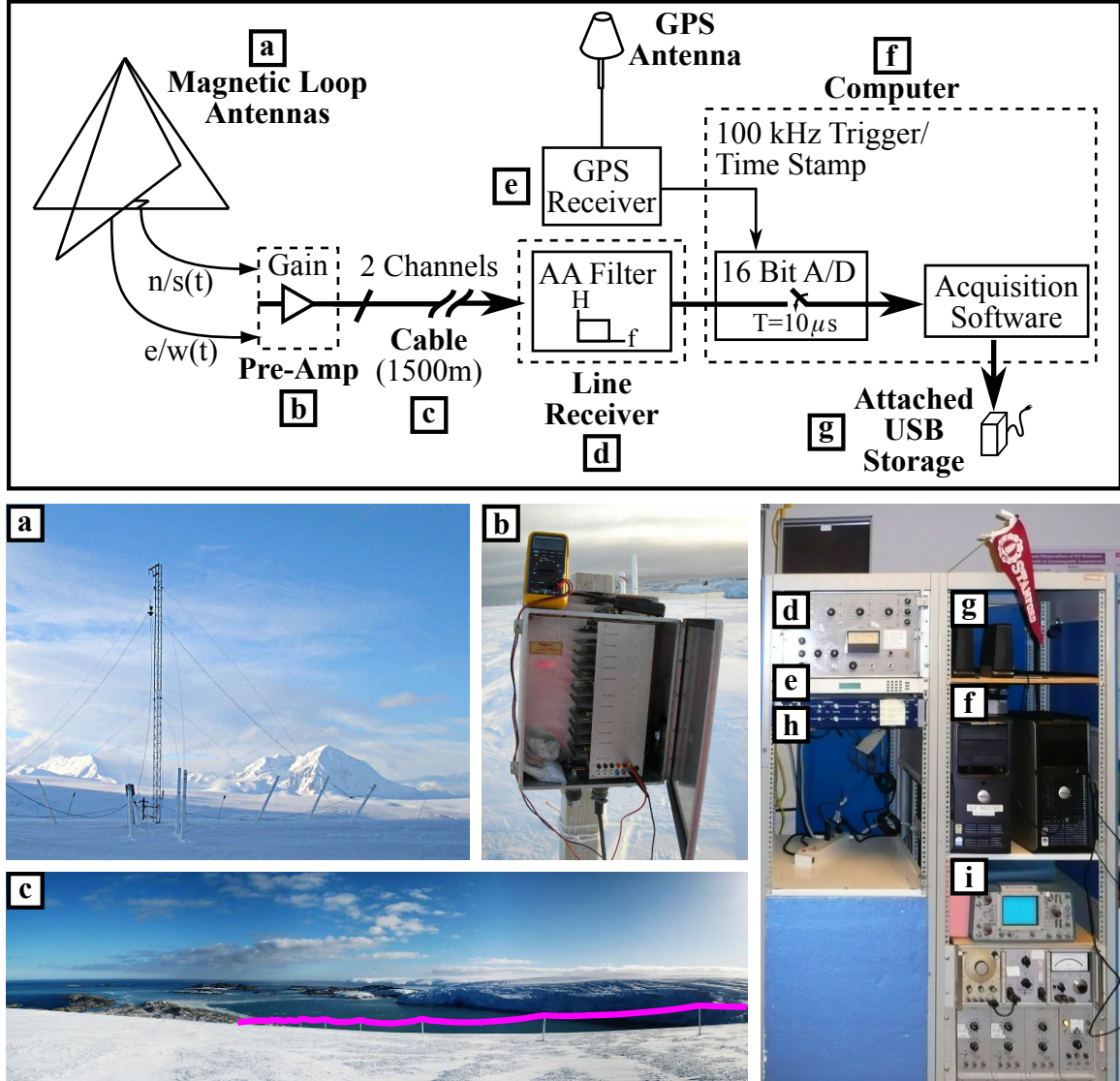


Figure 1.10: The Palmer receiver system consists of (a) two crossed-loop magnetic antennas, (b) a preamplifier, (c) 1500 m of signal cable (shown in false color for clarity), (d) a line receiver, (e) a GPS receiver, (f) acquisition software on a desktop computer, and (g) attached USB hard drives for data storage. The (h) signal splitter and (i) calibration circuit are legacy components that are not integral to the acquisition process. Block diagram after [Saïd \[2009, Fig. 3.1\]](#), and photos (a) and (b) courtesy of Robert Newsome.

1.4 Contributions of this Work

This dissertation is primarily concerned with using ground-based measurements of ELF/VLF chorus and hiss from Palmer Station to better understand the source variation of these waves and what factors affect their ability to propagate to the ground. Following a description of necessary scientific background in Chapter 2, we initially use measurements at Palmer to test two leading theories of hiss generation in Chapter 3. Following this, because only a subset of these waves are able to penetrate to and be received on the ground, we devote Chapter 4 to a study of which source populations of chorus Palmer is able to observe, and how these populations are influenced by the plasmapause. Finally, we discuss in Chapter 5 a method that we have developed of automatically detecting chorus and hiss emissions in broadband data, as well as some scientific results that we have made using a resulting database of emissions from Palmer. Conclusions and suggestions for future work appear in Chapter 6. Some relevant statistical methods and a small catalog of interesting emissions at Palmer are shown in Appendices A and B, respectively.

The contributions of this work may be summarized as follows:

1. Determined that dawn hiss is consistent with chorus as a source, while dusk hiss is more likely sourced by terrestrial lightning.
2. Determined that ELF/VLF chorus observations at mid-latitude ground stations are consistent with propagation in the non-ducted mode and emissions may therefore originate at field lines far removed from those of the receiving station.
3. Determined that the ability to observe ELF/VLF chorus at mid-latitude ground stations is strongly dependent on the instantaneous plasmasphere extent.
4. Developed a method to automatically detect and distinguish between chorus and hiss emissions in broadband ELF/VLF data.
5. Created the first database of spectrally-categorized broadband ELF/VLF chorus and hiss emissions spanning an entire solar cycle.

Chapter 2

Scientific Background

The following sections give some helpful scientific background to allow the reader to better understand the phenomena of chorus and hiss and to put the results of this thesis in context.

2.1 The Geomagnetic Coordinate System

When discussing magnetospheric phenomena, it is useful to employ a coordinate system that is developed around the geometry of the geomagnetic field, as discussed below.

2.1.1 Dipole Field Model

To first order, at radial distances of less than $\sim 4 R_E$, and during periods of low to moderate geomagnetic disturbance, the Earth's magnetic field may be approximated with a centered tilted dipole as shown in Figure 2.1, with the dipole axis inclined by about 11° with respect to the geographic rotation axis. Under this approximation, a location in geomagnetic coordinates may be described using three variables: L shell (or L value, L), magnetic latitude (λ) and magnetic local time (MLT). The L shell parameter was originally constructed by *McIlwain* [1961] for the purpose of organizing energetic particle data in a realistic magnetic field. Within the centered

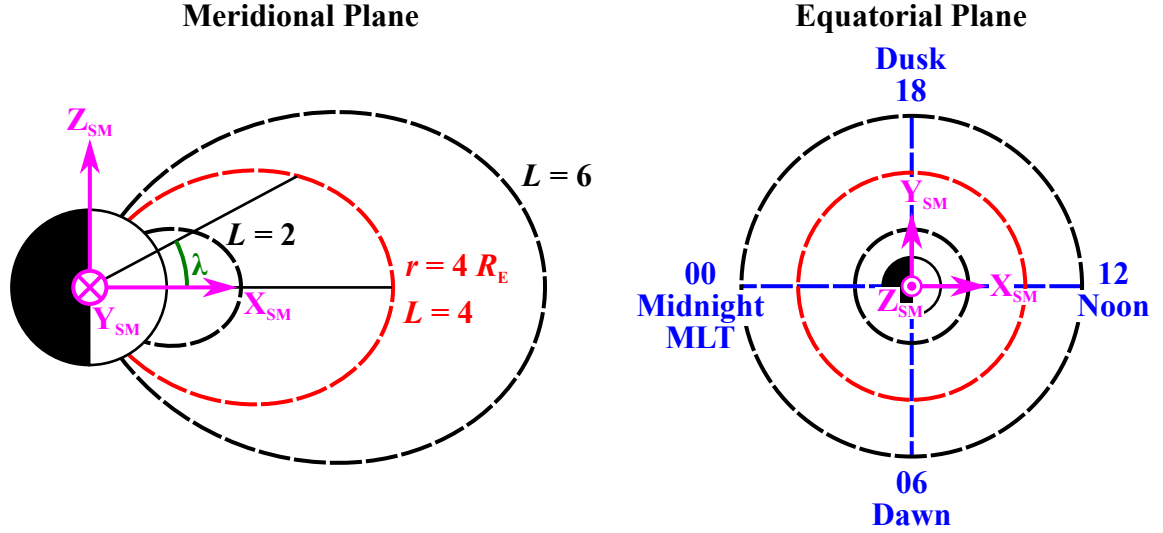


Figure 2.1: The geomagnetic coordinate system consists of three parameters: L shell (L), magnetic latitude (λ) and magnetic local time (MLT). These coordinates are illustrated in a (left) meridional plane and (right) equatorial plane. The definition of L shell as the radial extent of a given magnetic field line's equatorial crossing, in units of Earth radii, is strictly valid only under a dipole model of the Earth's magnetic field. Figure adapted from [Spasojević \[2003, Fig. 1.3\]](#).

dipole approximation, the definition is greatly simplified as the radial extent of the equatorial crossing of a set of field lines, in units of R_E . For example, all field lines that cross the geomagnetic equator at $4 R_E$ from the center of the Earth are described by $L=4$. The position along a given L shell is described by the angle λ , measured from the equatorial plane, ranging from -90 to 90° . Finally, MLT, in units of hours, describes the position of the field line with respect to the direction of the sun, where an MLT of 00 is in the anti-sunward direction, and 06, 12 and 18 describe dawn, noon and dusk, respectively. Invariant latitude (Λ , not to be confused with geomagnetic latitude, λ) is a constant of a given L shell and is defined as the value of λ of the given field line at its intersection with the surface of the Earth.

2.1.2 Solar Magnetic Coordinate System

The solar magnetic (SM) coordinate system is a standard right-handed Cartesian coordinate system for use when describing magnetospheric phenomena. In the solar magnetic coordinate system, the $+Z$ axis is parallel to the north geomagnetic pole, the $+Y$ axis is perpendicular to the Earth-Sun line, towards dusk, and the $+X$ axis completes the right-handed set. Note that the $+X$ axis does not point directly towards the sun, and the angle that it makes with respect to the ecliptic plane changes by 22° over a 24-hour period.

Conversion between the SM coordinate system and the L, λ, MLT coordinate system is simple when noting that the radial component in the spherical coordinate system, $\rho = \sqrt{x^2 + y^2 + z^2}$, is given by $\rho = L \cos^2 \lambda$ in the L, λ, MLT coordinate system [Walt, 1994, Eqn. 3.18]. The following equations allow conversion from L, λ, MLT coordinates to SM coordinates:

$$\rho = L \cos^2 \lambda \quad (2.1a)$$

$$x = \rho \cos \lambda \cos \left[\frac{2\pi}{24} (\text{MLT} + 12) \right] \quad (2.1b)$$

$$y = \rho \cos \lambda \sin \left[\frac{2\pi}{24} (\text{MLT} + 12) \right] \quad (2.1c)$$

$$z = \rho \sin \lambda \quad (2.1d)$$

and vice versa

$$\rho = \sqrt{x^2 + y^2 + z^2} \quad (2.2a)$$

$$L = \rho / \cos^2 [\arcsin(z/\rho)] = \frac{\rho}{1 - (z/\rho)^2} \quad (2.2b)$$

$$\lambda = \arcsin(z/\rho) \quad (2.2c)$$

$$\text{MLT} = \text{mod} \left[\arctan_2(y, x) \frac{24}{2\pi} + 12, 24 \right] \quad (2.2d)$$

where \arctan_2 is the four-quadrant arctangent function (`atan2` in Matlab).

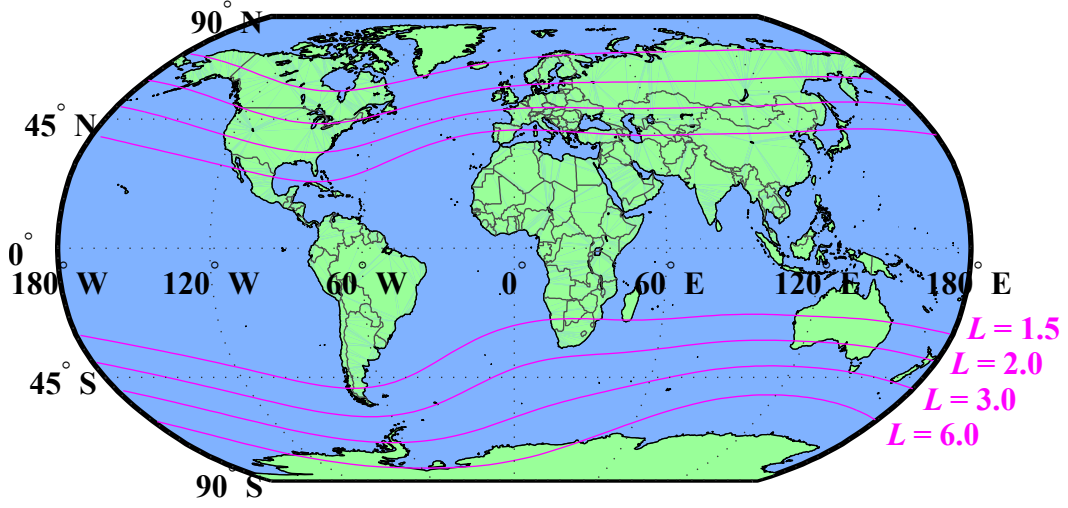


Figure 2.2: A map showing contours of CGM L shells. L shells converge in the vicinity of the geomagnetic poles, which results in the unequal spacing of L shells with respect to each other.

2.1.3 IGRF and Tsyganenko Field Models

When considering a more accurate non-dipole magnetic field, the SM coordinate system remains valid but the definitions of L , λ and MLT must be changed. The geomagnetic locations of ground receivers are often quoted in the corrected geomagnetic coordinate (CGM) system [Gustafsson *et al.*, 1992], which is based on the International Geomagnetic Reference Field (IGRF) model. To determine the L shell of a given location in space or on the Earth's surface, the IGRF model is used to trace the field line which intersects that location until it reaches the dipole equatorial plane. Then, the dipole magnetic field line which intersects that equatorial point is noted. The L shell of the original point is defined as the L shell of this dipole field line, and λ is defined as the geomagnetic latitude of the dipole field line's intersection with the surface containing the original point. A map showing several CGM L shell contours on the surface of the Earth is shown in Figure 2.2.

Determination of MLT in the CGM system is as follows [Papitashvili, 2001]. Let us assume that the station is located at local midnight, i.e., at some UT instance the local geographic meridian is at 00 LT and the station is “behind” the geographic

pole with respect to the Sun. If the Earth rotates through an angle (measured in UTC hours) so that the station’s local CGM meridian (approximated by the great-circle arc) is moved to 00 MLT, then the station is “behind” the CGM pole with respect to the Sun. The time through which the Earth must rotate so that this is so is the station’s MLT, with respect to UTC. For example, an MLT of UTC $- 4$ indicates that, at UTC = 20, the geomagnetic meridian containing the station and the geomagnetic poles also contains the Sun-Earth direction.

The IGRF model only takes into account contributions to the magnetic field from within the Earth and specifically excludes external forcing effects from the IMF and the solar wind. The IGRF model is therefore only valid when the effects of those external forces are minimal, namely for radial distances (CGM L shells) of a few Earth radii. At greater radial distances, or during periods of large geomagnetic disturbances, it is necessary to use a more complex magnetic field model which takes the effects of the IMF and solar wind into account. The Tsyganenko magnetic field model, currently in version TS05, meets this need [*Tsyganenko and Sitnov, 2005*]. Under this more complex model, due to the distortion of the shape of the geomagnetic field, the L shell and MLT terms cease to have intuitive geometric meaning and alternate coordinates are required [*Roederer, 1970*, Sec. IV.5]. These coordinates are defined in the context of the drift paths of energetic particles in the magnetosphere and are beyond the scope of this thesis. The mid and low-latitude phenomena discussed in this work are adequately described by the IGRF model and CGM coordinates.

2.2 Wave Propagation in a Magnetized Plasma

A plasma is an electrically neutral, highly ionized gas with sufficient densities of ions and electrons such that collective effects become important. Propagation of electromagnetic waves within a plasma is complicated by the fact that the oscillating wave electric and magnetic fields induce motion in the free charges within the plasma. The motions of the charged particles constitute a current, which in turn modifies the properties of the wave. The presence of a static magnetic field within the plasma

orders the motion of the free charges and further modifies the properties of propagating electromagnetic waves. Thus, a cold, magnetized plasma is both anisotropic, meaning that propagation characteristics are different in different directions, and dispersive, meaning that different frequencies have different propagation characteristics. Further, the presence of significant densities of warm or hot charged particles within the plasma can further influence wave properties including damping or growth of the waves. Beyond the discussion in this chapter, a more detailed explanation of waves in plasmas may be found in [Bittencourt \[2004, Ch. 16\]](#).

2.2.1 Whistler-Mode Plasma Waves

The refractive index of a wave in an arbitrary medium is given by

$$n^2 = \left(\frac{ck}{\omega} \right)^2 \quad (2.3)$$

where c is the speed of light in free space, k is the wave number (whose magnitude and direction together comprise the wave k -vector), and ω is the wave frequency. In a cold, magnetized plasma, neglecting the effects of ions and collisions, the refractive index is a function of the ambient plasma parameters (electron number density and magnetic field strength), the wave frequency, and the direction of propagation with respect to the magnetic field. The refractive index is then approximated by the Appleton-Hartree equation:

$$n^2 = 1 - \frac{X}{1 - \frac{\frac{1}{2}Y^2 \sin^2 \theta}{1 - X} \pm \frac{1}{1 - X} \left(\frac{1}{4}Y^4 \sin^4 \theta + Y^2 \cos^2 \theta (1 - X)^2 \right)^{1/2}} \quad (2.4)$$

where θ is the angle between the ambient magnetic field vector and the wave k -vector, $X = \omega_{pe}^2 / \omega^2$, $Y = \Omega_{ce} / \omega$, ω_{pe} is the electron plasma frequency (the intrinsic oscillation frequency of the plasma, a function of the electron number density) and Ω_{ce} is the electron cyclotron frequency (the frequency at which electrons gyrate around the ambient magnetic field, a function of the magnetic field strength). ω , ω_{pe} and Ω_{ce} are

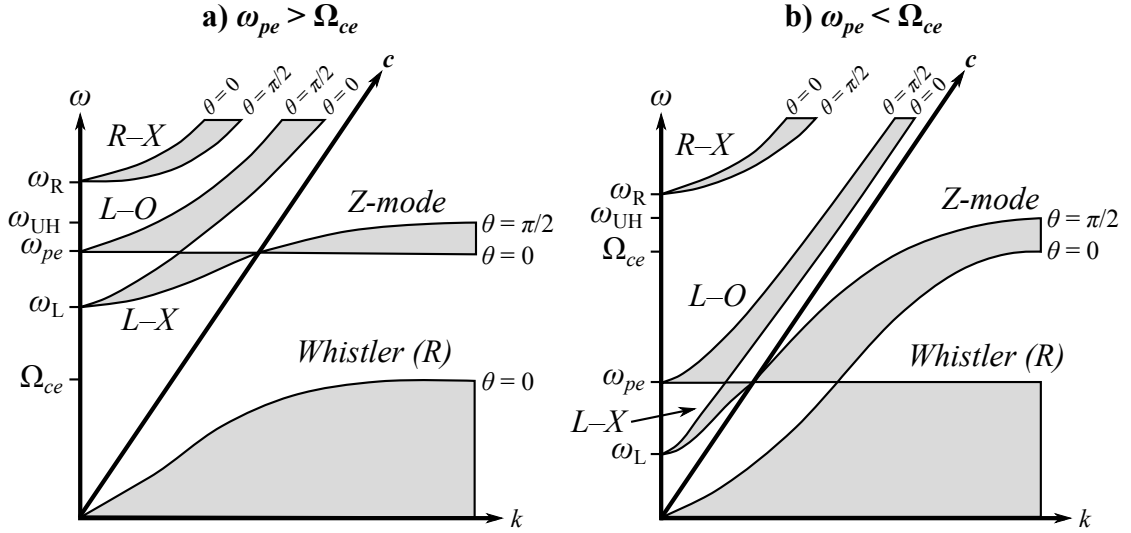


Figure 2.3: ω - k diagram of the various modes of electromagnetic waves allowed in a cold electron plasma either with (a) high plasma density and comparatively low magnetic field ($\omega_{pe} > \Omega_{ce}$, the usual case in the magnetosphere) or (b) low plasma density and comparatively high magnetic field ($\omega_{pe} < \Omega_{ce}$). Figure adapted from [Kivelson and Russell \[1995, Fig. 12.17\]](#)

angular frequencies (in units of radians/sec), and their regular frequency analogues (in units of Hz) are written as f , f_{pe} and f_{ce} , respectively.

The various types of electromagnetic waves which may arise from solutions of the Appleton-Hartree equation are shown in the ω - k diagram of Figure 2.3. The ω - k diagram is useful because it gives insight into both the phase velocity $v_p = \omega/k$, and the group velocity $v_g = \partial\omega/\partial k$ of the waves. The dark lines on the plots indicate propagation either parallel ($\theta = 0$) or perpendicular ($\theta = \pi/2$) to the magnetic field direction, and shaded regions represent solutions with intermediate values of θ . Waves labeled with an “R” are right-hand circularly polarized for purely parallel propagation (with respect to time, from the perspective of a stationary observer), and those labeled “L” are left-hand circularly polarized.

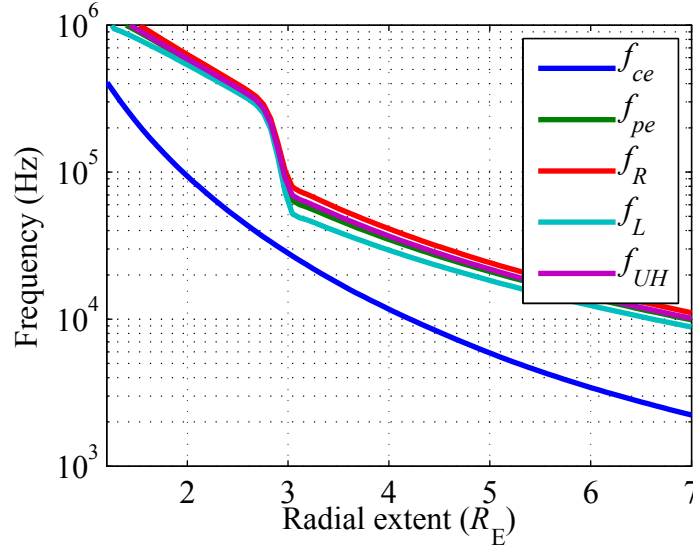


Figure 2.4: Typical cutoff frequencies for wave modes from Figure 2.3 in a model magnetosphere as a function of radial distance at the equatorial plane. Note that the y -axis is in units of frequency (sec^{-1}) as opposed to angular frequency (rad/sec).

The various cutoffs in Figure 2.3 are defined as

$$\omega_R = \frac{\Omega_{ce}}{2} + \sqrt{\omega_{pe}^2 + \Omega_{ce}^2/4} \quad (2.5)$$

$$\omega_L = -\frac{\Omega_{ce}}{2} + \sqrt{\omega_{pe}^2 + \Omega_{ce}^2/4} \quad (2.6)$$

$$\omega_{UH} = \sqrt{\omega_{pe}^2 + \Omega_{ce}^2}, \quad (2.7)$$

where ω_R and ω_L are the cutoff frequencies for the left and right-hand polarized waves and ω_{UH} is the upper hybrid frequency. Typical frequencies of these cutoffs in the magnetosphere are shown in Figure 2.4. These frequencies are derived using the GCPM model of magnetospheric plasma density [Gallagher *et al.*, 2000] with the plasmapause at $L=2.9$ and the Tsyganenko TS05 magnetic field model [Tsyganenko and Sitnov, 2005] during a moderately disturbed period ($K_p=3$).

Chorus and hiss waves propagate in the whistler mode in the magnetosphere. The whistler-mode refractive index may be calculated from (2.4) assuming the negative sign in the denominator (which corresponds to right-hand polarization) and $X, Y > 1$.

Because the electron plasma frequency is typically much higher than the electron gyrofrequency ($\omega_{pe} \gg \Omega_{ce}$), the whistler mode propagates with frequencies which are exclusively below Ω_{ce} , while all other modes propagate with frequencies exclusively above Ω_{ce} , as shown in Figure 2.3a. As Figure 2.4 shows, at lower altitudes, $f_{ce} = \Omega_{ce}/2\pi$ increases to greater than 100 kHz. Because the Palmer receiver samples at 100 kilosamples/sec, it is only capable of observing waves below 50 kHz; thus, because all waves with frequencies below 50 kHz in modes other than the whistler mode will be cut off with decreasing altitude, the only magnetospheric waves which may be observed with the Palmer receiver are those that have propagated in the whistler mode.

The name of the whistler mode is analogous to that of the whistler signals themselves, which begin as impulses from terrestrial lightning. After escaping from the atmosphere, whistlers propagate magnetospherically in the whistler mode before returning to Earth in the dispersed form which gives them their characteristic whistling sound on audio recordings. It should be noted that some authors use the term “whistler” to denote any signal propagating in the whistler mode; in this thesis, we reserve the term “whistler” to mean only those whistler-mode signals which have originated in terrestrial lightning.

We can see from Figure 2.3a that the value of ω/k initially rises gradually with frequency, reaches a maximum slope, and then rises more slowly before approaching its asymptote at Ω_{ce} . This behavior indicates that whistler mode signals at the highest and lowest frequencies have the lowest group velocities and suffer the most dispersion, compared to whistlers of mid-range frequencies, as is the case with lightning-generated whistlers observed in the conjugate hemisphere. In fact, given that whistlers have a known (impulse) source function, whistlers are often used as a remote sensing diagnostic tool to determine the properties of the magnetospheric medium through which they have propagated [e.g., *Carpenter and Smith, 2001*].

A common technique for modeling the propagation of waves in a magnetized plasma is known as “raytracing.” Under a realistic model of geomagnetic field and ambient particle densities, raytracing effectively calculates the differential solution of Snell’s law of refraction for a given wave packet, assuming specified initial conditions

and a slowly-varying medium. We use raytracing extensively in the chorus propagation study of Chapter 4 and a detailed discussion of the newly-developed raytracer that was used for this study can be found in Section 4.4.1.

2.2.2 Wave-Particle Interactions

In the discussion above, the plasma is assumed to be cold, meaning that the average velocity of the particles is taken to be zero. In this case, the ambient plasma properties influence the direction and speed of the propagating wave, but no energy is exchanged between the wave and the plasma. However, any realistic plasma consists of charged particles with a distribution of velocities, and under certain circumstances it is possible for energy to be exchanged between particles and waves, a process known as wave-particle interactions.

For simplicity, we assume for the purpose of the ensuing discussion that the waves propagate parallel to the ambient magnetic field. Specifically, waves and particles may exchange energy when the Doppler-shifted frequency of the wave, as observed in the frame of reference of the particle guiding center, is equal to a multiple of the particle gyrofrequency. This condition is known as cyclotron resonance and is expressed as

$$\omega - k_{\parallel}v_{\parallel} = m\Omega_{ce}/\gamma, \quad (2.8)$$

where ω is the wave frequency, k_{\parallel} is the parallel component of the wave k -vector (with respect to the ambient magnetic field), v_{\parallel} is the parallel component of the particle velocity (i.e., its guiding center velocity), Ω_{ce} is the electron cyclotron frequency, $\gamma = (1 - v^2/c^2)^{-1/2}$ is the relativistic Lorentz factor, and m is any integer. The quantity on the left-hand side, $\omega - k_{\parallel}v_{\parallel}$, is the Doppler-shifted wave frequency as experienced by the moving particle.

When a wave passes by a particle which is out of resonance with the wave, the rapid oscillations in electric field result in zero net field experienced by the particle over time, and there is no resulting particle acceleration. However, when the oscillations of the wave and particle are nearly matched in velocity via the resonance condition of (2.8), energy may be transferred between the wave and particles. It is important to

note that this transfer of energy proceeds entirely without the aid of collisions; wave particle interactions are significant even in plasma populations that are sufficiently sparse as to be considered collisionless.

Landau Resonance (Landau Damping)

When $m=0$ in (2.8), the resonance condition takes the form of the Landau resonance,

$$\omega - k_{\parallel} v_{\parallel} = 0. \quad (2.9)$$

This condition takes effect when the wave and particle are traveling in the same direction along a field line, and the sense of rotation is identical and in phase. In this case, the particle experiences a nearly constant electric field in its reference frame, the result being that the particles moving slightly faster than the wave lose energy to the wave, leading to wave growth, and particles moving slightly slower than the wave gain energy from the wave, leading to wave damping. In a standard Maxwellian distribution for an equilibrium plasma, there are more electrons with energies immediately below this resonant energy than above, and this results in the plasma gaining energy at the expense of the wave. Thus, the typical interaction at the Landau resonance is Landau damping, which is the loss of wave energy to the ambient electrons. In the magnetosphere, where collisions between particles are typically negligible, Landau damping is the major source of energy loss for propagating whistler-mode waves. Landau damping [Kennel, 1966; Brinca, 1972] is typically included in accurate ray-tracing models of magnetospheric wave propagation [e.g., Bortnik *et al.*, 2007a], and is included in the modeling component of Chapter 4 (a full discussion can be found in Section 4.4.1).

Figure 2.5 shows typical electron energies for the Landau resonance on the geomagnetic equator using the CA92 plasma density model [Carpenter and Anderson, 1992] at MLT=6 and $K_p=5_{\circ}$ with the plasmapause at $L=3.3$ and a dipole geomagnetic field. This model assumes waves propagating parallel to the geomagnetic field with wave frequency set to 0.35 times the equatorial electron gyrofrequency (f_{ceq}), which is the peak frequency of lower-band chorus occurrence [Burtis and Helliwell,

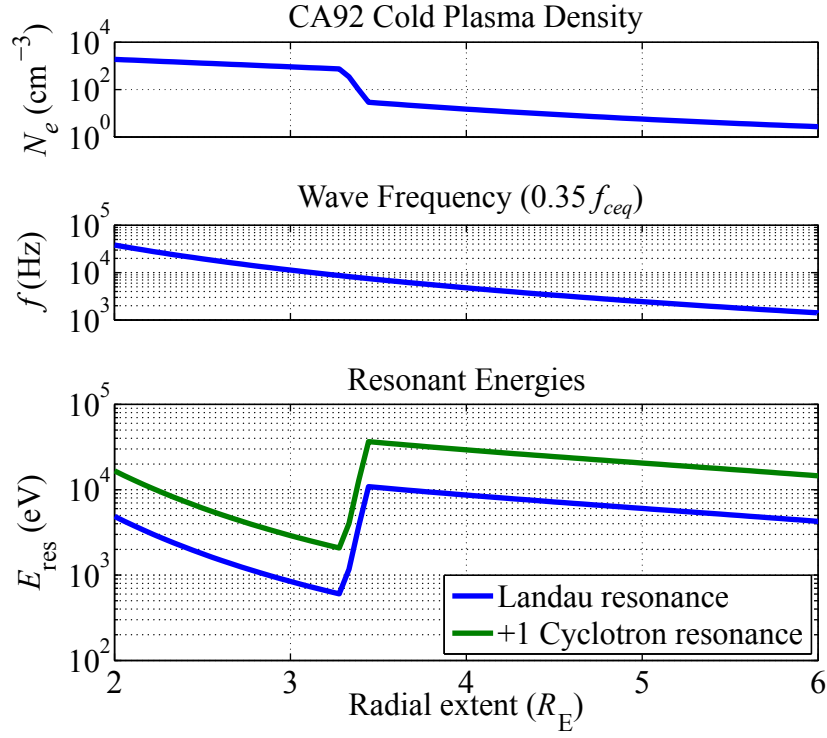


Figure 2.5: Resonant energies for Landau ($m=0$) and Cyclotron ($m=1$) resonances for parallel whistler wave propagation and loss-cone particles. Relativistic effects are included.

1976]. Electron pitch angles (the angle between the net particle momentum and the geomagnetic field) are such that the electrons mirror at 100 km altitude; this gives a lower bound on total electron energy, as particles with lower parallel energy will precipitate into the ionosphere and be lost from the radiation belts. As shown in the figure, typical minimum Landau resonance energies are on the order of 1 keV inside the plasmasphere and on the order of 10 keV outside.

Cyclotron Resonance

In addition to the Landau resonance, other resonances are possible when m in (2.8) is an integer other than 0. These resonances are known as the gyro or cyclotron resonances, the strongest of which occurs when $m=1$, when the Doppler-shifted wave

frequency equals the electron gyrofrequency,

$$\omega - k_{\parallel}v_{\parallel} = \Omega_{ce}/\gamma. \quad (2.10)$$

In contrast to Landau resonance, which is primarily responsible for causing diffusion in energy of the ambient electron distributions, cyclotron resonance is primarily responsible for causing diffusion in *pitch angle* (α) of the electrons, where pitch angle is defined as the angle of the particle momentum with respect to the ambient magnetic field. This angle is usually expressed in terms of the parallel and perpendicular components of the particle momentum, p , where $p_{\parallel} = p \cos \alpha$ and $p_{\perp} = p \sin \alpha$.

The result of this interaction between waves and electron pitch angles is that whistler-mode waves may be generated when the ambient electron distribution is anisotropic, that is, $p_{\perp} > p_{\parallel}$. Anisotropic particle distributions are a common feature of the magnetosphere and can be generated by a variety of processes including adiabatic heating during periods of enhanced convection or solar wind dynamic pressure and non-adiabatic processes such as substorm injections (as discussed in Section 1.1.3). During the cyclotron resonant interaction, the transfer of electron energy from the particle to the wave results in both the lowering of the particles' pitch angle and total energy, allowing a subset of the electrons to be precipitated into the neutral atmosphere [Tsurutani and Smith, 1974] as well as growth of the wave. Thus, this cyclotron resonant interaction is both a loss mechanism for energetic electrons and a source of whistler-mode waves such chorus and hiss. As shown in Figure 2.5, typical minimum cyclotron resonant energies are somewhat below 10 keV inside the plasmasphere and somewhat above 10 keV outside.

2.3 Properties of Chorus and Hiss

Because of their ability to propagate to the ground (as explained in Section 2.2.1), chorus and hiss were some of the first magnetospheric waves to be discovered and have enjoyed a long history of study. After many initial ground-based studies, in situ satellite studies beginning in the late 1960's began to shed far more light on chorus

and hiss source locations and generation mechanisms. These source locations and generation mechanisms and the roles that these waves play in maintaining radiation belt structure are continuously evolving topics and currently the source of much interest and debate (as discussed subsequently in this section). Extensive review papers are available for both chorus [*Sazhin and Hayakawa, 1992; Santolík, 2008*] and hiss [*Hayakawa and Sazhin, 1992*].

Though chorus and hiss emissions share similar frequency bands and may often be observed simultaneously both on the ground and in space, they are intrinsically different emissions, usually appearing in disparate parts of the magnetosphere and with different source mechanisms and implications for the radiation belts. In this section, we discuss separately the characteristics of chorus and hiss (and their subtypes) before showing that, despite their differences, links between the emissions are continuing to be debated and explored.

2.3.1 Spectral Characterization and Source Locations

Chorus

Chorus originates in the equatorial plane [*LeDocq et al., 1998*] outside the plasmasphere according to early satellite studies which found it to be most prevalent there [e.g., *Gurnett and O'Brien, 1964; Dunckel and Helliwell, 1969*]. This source region is illustrated with the orange trace in the cartoon of Figure 2.6. Spectrally, chorus is characterized by a closely-spaced series of semi-coherent discrete tones, usually rising in frequency with time at a rate of up to a few kHz/sec. Chorus typically appears in the frequency range from a few hundred Hz to ~ 6 kHz [e.g., *Sonwalkar, 1995*, Sec. 4.2.1.3]. In situ observations [*Tsurutani and Smith, 1974, 1977; Burtis and Helliwell, 1976*] have shown that chorus often has a two-banded structure, separated by half the equatorial electron gyrofrequency, Ω_{ceq} . Of the two bands, only the lower band, with frequencies in the range of $0.1\text{--}0.5 \Omega_{ceq}$, is thought to reach the ground; the upper band is believed to reflect at high altitudes due to its highly oblique wavenormal angle [*Hayakawa et al., 1984; Haque et al., 2010*]. Thus, chorus received on the ground is expected to be exclusively lower band chorus, generated below half the

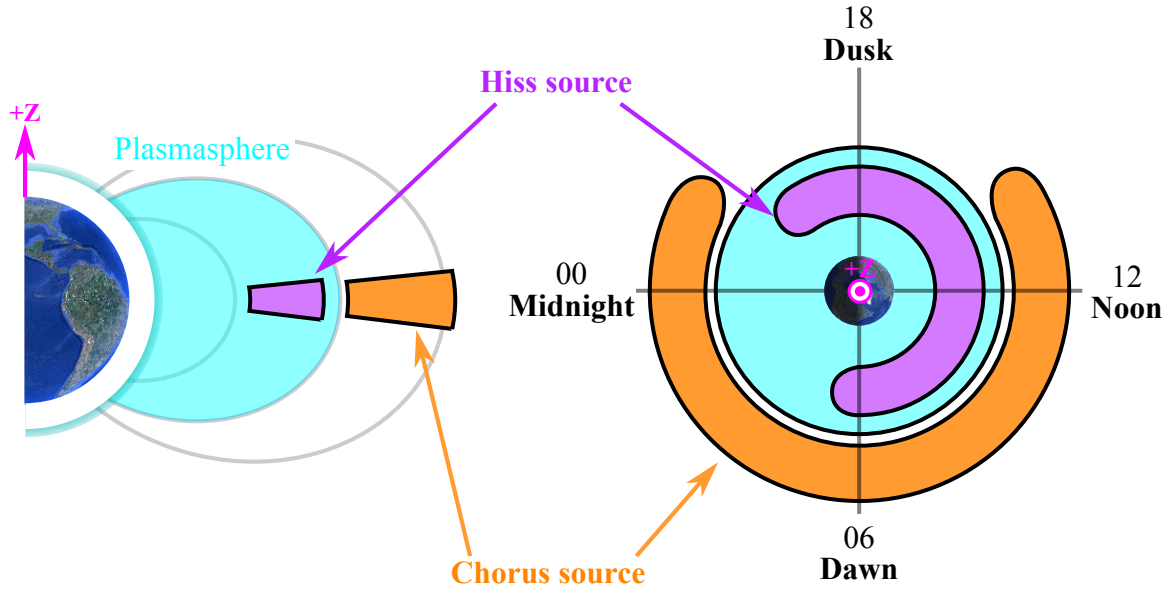


Figure 2.6: Sources of chorus and hiss in the magnetosphere in (left) meridional and (right) equatorial views. Chorus is sourced at the equator, outside of the plasmasphere, primarily on the dawn side, while hiss is sourced on the equator, inside of the plasmasphere, primarily on the day side. Interpreted using data from [Meredith et al. \[2001, 2004\]](#).

equatorial gyrofrequency. An example spectrogram of chorus was shown previously in Figure 1.7a.

Numerous studies performed using ground-based [[Allcock, 1957](#); [Pope, 1957, 1960](#)] and space-based [[Burtis and Helliwell, 1976](#); [Tsurutani and Smith, 1977](#); [Meredith et al., 2001](#)] receivers have shown that, although the local time of maximal chorus occurrence increases with increasing L shell, chorus is nonetheless primarily confined to the dawn and day sectors at all L shells. Chorus occurrence is a strong function of geomagnetic activity and substorms [e.g., [Tsurutani and Smith, 1974](#); [Burtis and Helliwell, 1976](#); [Meredith et al., 2001](#)]. These factors are a result of the fact that chorus is believed to be generated by anisotropic electrons which are injected into the midnight sector during substorms; these electrons then drift eastwards, generating chorus via cyclotron resonant interactions at midnight and later MLTs. This generation mechanism is discussed in more detail in Section 2.3.3.

Hiss

Several varieties of hiss permeate the magnetosphere. All varieties of hiss are composed of incoherent, unstructured emissions. An example spectrogram of hiss was shown previously in Figure 1.7b. Naming conventions for the different varieties of hiss are occasionally contested, which is not surprising considering the preponderance of ground and space-based observations of hiss, often with different conclusions.

One type of hiss of which there is not currently much nomenclature dispute is auroral hiss. As its name implies, auroral hiss appears near the auroral zone, and has a frequency range that can extend up to several hundred kHz [*e.g.*, [Jørgensen, 1968](#); [Makita, 1979](#)]. As auroral hiss is not observed at Palmer Station, we do not discuss auroral hiss in this thesis.

At least four other distinct types of ELF/VLF hiss exist: plasmaspheric hiss, exohiss, ELF hiss and mid-latitude hiss. We make mention of these different types of hiss emissions here in order to contrast their definitions with our discussion of hiss emissions observed at Palmer in Chapter 3. These terms are particularly confusing because many permutations of them may be observed within the plasmasphere, at mid-latitudes, and in the ELF range, besides the obvious eponymous varieties.

“Plasmaspheric hiss” is an emission that is seen on in situ measurements exclusively within the plasmasphere [[Dunckel and Helliwell, 1969](#); [Russell et al., 1969](#); [Thorne et al., 1973](#)]. Plasmaspheric hiss peaks in amplitude slightly below 1 kHz, and can extend up to ~ 3 kHz. Satellite observations have found that plasmaspheric hiss occurs primarily in the day and dusk sectors, as shown in the purple trace in Figure 2.6, although the amplitude of the hiss and the specific L shells and local times of maximum observation are strong functions of geomagnetic activity [[Parady et al., 1975](#); [Meredith et al., 2004](#)]. Plasmaspheric hiss is supposedly never observed on the ground [[Sonwalkar, 1995](#), Sec. 4.2.1.1] due to theoretical considerations of magnetospheric reflection near the local lower hybrid resonance frequencies [[Thorne and Kennel, 1967](#)] and the low-frequency cutoff between the proton and helium gyrofrequencies [[Gurnett and Burns, 1968](#)]. Although [Hayakawa et al. \[1985\]](#) claimed to have made ground observations of plasmaspheric hiss, the frequency range (mostly

above ~ 1.5 kHz) was generally more in line with that of mid-latitude hiss (see below). [Kleimenova et al. \[1976\]](#) made ground observations of morning hiss at 400 Hz during periods of low geomagnetic activity level but stated that this could not be plasmaspheric hiss in light of the above cited work by [Thorne and Kennel \[1967\]](#) and [Gurnett and Burns \[1968\]](#).

Two separate types of hiss whose frequency spectrum resembles that of plasmaspheric hiss are seen at medium latitudes outside of the plasmasphere, and are known either as “exo-hiss” or “ELF hiss.” ELF hiss and exo-hiss share similar frequencies and latitudes of observation but are differentiated primarily by their diurnal occurrence and theorized generation methods. Exo-hiss, believed to be the result of plasmaspheric hiss leaking out of the plasmasphere, appears primarily in the afternoon sector and shows no correlation with geomagnetic activity [[Thorne et al., 1973](#)]. ELF hiss appears primarily on the dayside [[Russell et al., 1972](#); [Meredith et al., 2004](#); [Santolík et al., 2006](#)], and although the actual origin of ELF hiss is controversial, it has been proposed to be caused by emissions generated equatorially outside of the plasmopause, propagating to low altitudes [[Santolík et al., 2006](#); [Bortnik et al., 2008](#)].

“Mid-latitude hiss” is a VLF emission that is generally observed on the ground and low-altitude satellites with an intensity and occurrence peak between 50° and 65° invariant latitude. Higher-altitude satellites have also seen mid-latitude hiss at latitudes everywhere from the equator to subauroral latitudes [[Taylor and Gurnett, 1968](#); [Dunckel and Helliwell, 1969](#)]. Mid-latitude hiss correlates well with geomagnetic activity, increasing in intensity and occurrence, and decreasing in L shell as K_p increases. Mid-latitude hiss can generally extend from ~ 2 to 10 kHz, though its bandwidth and center frequency is variable [[Hayakawa and Sazhin, 1992](#); [Sonwalkar, 1995](#)]. It is worth noting that the primary observational difference between mid-latitude hiss and the other types of hiss discussed here is the observed frequency range ($f \gtrsim 2$ kHz for mid-latitude hiss versus $f \lesssim 3$ kHz for plasmaspheric, ELF and exo-hiss, with an overlap between ~ 2 -3 kHz).

These varieties are summarized in Table 2.1. As is discussed in Chapter 3, the parameters of hiss observed at Palmer Station are most consistent with plasmaspheric hiss. Although the colloquial belief is that plasmaspheric hiss cannot reach

Table 2.1: Magnetospheric ELF/VLF Hiss Varieties

Type	Freq.		MLT	Geomag. Dep.	Notes
Plasmaspheric hiss	300 3 kHz	Hz–	Day, Dusk	Strongly dependent	Observed inside plasmasphere; supposedly not seen on ground
Exo-hiss	300 3 kHz	Hz–	Post- noon	Not depen- dent	Observed outside plasmasphere; plasmaspheric hiss leaking out of plasmasphere
ELF hiss	300 2 kHz	Hz–	Day	N/A	Observed outside plasmasphere; possibly sourced by chorus
Mid-latitude hiss	2–10 kHz		All	Strongly dependent	Peak occurrence for $50^\circ < \Lambda < 65^\circ$

the ground, this is a purely theoretical argument and neglects the possibility of, e.g., scattering by meter-scale density irregularities which would rotate the hiss wavenormals and potentially allow them to reach the ground (see Section 1.2.1).

Simultaneous Observations

Chorus and hiss have very different spectral properties and often occur in different local times, at different frequencies and in different parts of the magnetosphere, particularly during storms [Hayakawa *et al.*, 1975b, 1977]. However, they do have overlapping frequency bands and are also often observed simultaneously [Dunckel and Helliwell, 1969; Koons, 1981; Parrot *et al.*, 2004; Santolík *et al.*, 2006]. In particular, Cornilleau-Wehrlin *et al.* [1978] made observations of chorus and hiss with the GEOS spacecraft at high altitudes ($\geq 6R_E$) and low geomagnetic activity levels ($K_p < 3^-$), demonstrating that the dominant emission in this region involves both chorus and hiss appearing together. This observation may at least partly be a manifestation of the ability for chorus to generate hiss emissions and vice versa, as discussed in

Section 2.3.3.

2.3.2 Role in Maintaining the Radiation Belt Structure

It has been recognized for some time that wave-particle interactions involving hiss emissions may play an important role in maintaining the structure of the radiation belts. Early studies by *Lyons et al.* [1972] and *Lyons and Thorne* [1973], later quantified more rigorously by *Abel and Thorne* [1998], showed that a combination of Landau and cyclotron resonant interactions (discussed in Section 2.2.2) between whistler mode waves and radiation belt electrons are a major contributor to loss of electrons in the slot region between the inner and outer belts.

It was thought for some time that the main driver of electron acceleration to relativistic radiation belt energies in the outer belt was radial diffusion [*Fälthammar*, 1965; *Schulz and Lanzerotti*, 1974]. Under this theory, ultralow frequency (ULF) fluctuations in the geomagnetic field match the frequency of particles drifting around the Earth, causing the particles to diffuse towards lower L shells. As the electrons move inward, they gain energy. However, *Meredith et al.* [2002] and *Horne et al.* [2003] quantified the effect of electron acceleration caused by wave-particle interactions involving chorus and concluded that the effect was large enough to be considered a major contributor. Following this work, the analysis of *Horne et al.* [2005] showed in the wake of a major geomagnetic storm that radial diffusion was inadequate to explain the observed creation of a new radiation belt and that, in this case, wave-particle interactions were more effective at accelerating electrons than radial diffusion.

In addition to accelerating electrons in the equatorial region, chorus has also been shown to precipitate energetic electrons out of the radiation belts at high latitudes and lower L shells [e.g., *Lorentzen et al.*, 2001; *O'Brien et al.*, 2003; *Thorne et al.*, 2005; *Shprits et al.*, 2006]. Therefore, chorus may have a dual role in maintaining the radiation belts, by both accelerating electrons to relativistic energies in the equatorial plane and precipitating those same electrons out of the belts at high latitudes under the right conditions [*Bortnik and Thorne*, 2007].

The recent discovery in particular of evidence of the contribution of chorus to the

maintenance of the outer radiation belt has led to a renewed interest in characterizing the magnetospheric morphology of both chorus and hiss emissions, including this present thesis.

2.3.3 Generation Mechanisms

Chorus

Chorus waves are believed to be generated by a Doppler-shifted cyclotron interaction between anisotropic distributions of energetic > 40 keV electrons and ambient background VLF noise [e.g., [Nunn et al., 1997](#); [Trakhtengerts, 1999](#)], though the precise structure of chorus is still under active investigation. These unstable anisotropic electron distributions usually result from the injection of electrons from the magnetotail into the inner magnetosphere during substorms. Because these electron are injected in the midnight local time sector and drift eastwards, chorus is predominantly observed across the morning and noon local time sectors. Magnetic substorms both increase the flux of hot, anisotropic source electrons which generate chorus as well as enhance the auroral electrojet. As a result, increases in the AE index have been shown to be a good predictor of chorus occurrence within the inner magnetosphere [[Smith et al., 1999](#); [Meredith et al., 2001](#)].

Hiss

Early theoretical studies of plasmaspheric hiss [[Kennel and Petscheck, 1966](#); [Kennel and Thorne, 1967](#); [Thorne et al., 1973, 1979](#); [Church and Thorne, 1983](#)] determined that its most likely source mechanism was the amplification of ambient wave turbulence via a cyclotron resonant interaction. Low amplitude waves repeatedly transit through the equatorial plane after magnetospherically reflecting at higher latitudes, becoming amplified through repeated cyclotron interactions with anisotropic particle distributions near the geomagnetic equator.

Though the source of the initial wave turbulence for this process is unclear, one hypothesis is that the seed is provided in the form of whistlers sourced from terrestrial lightning [[Sonwalkar and Inan, 1989](#); [Draganov et al., 1992](#)]. Recent work by [Green](#)

et al. [2005] and *Meredith et al.* [2006] have shown experimental data highlighting the correlation of terrestrial lightning rates with certain frequencies of hiss. Although they disagreed on the precise frequency ranges, *Green et al.* [2005] and *Meredith et al.* [2006] both concluded that lightning may be a dominant source of hiss above either 500 Hz or 2 kHz, respectively, although *Meredith et al.* [2006] did note that the lower-frequency, non-lightning associated hiss, being more intense than the lightning-associated variety, is a more important loss mechanism for relativistic electrons between $2 < L < 3$.

Connections Between Chorus and Hiss

Many attempts have been made to explain the connections between chorus and hiss. *Koons* [1981] suggested that hiss emissions may set up a suitable electron anisotropy for the generation of chorus. This hypothesis was supported via experiments by *Helliwell et al.* [1986], during which hiss-like incoherent noise, radiated by the Siple transmitter in Antarctica, was observed to trigger discrete emissions.

An alternate hypothesis for the chorus-hiss connection is that hiss consists of overlapping chorus emissions, whose frequency-time structures have become sufficiently diffuse that they eventually appear hiss-like to observers. *Santolík et al.* [2006] suggested this as a likely mechanism for ELF hiss outside the plasmasphere while *Bortnik et al.* [2008] showed that this mechanism may be viable for plasmaspheric hiss as well. *Parrot et al.* [2004] specifically made note of hiss emissions on the Cluster satellites that showed signs of discrete structure, the first suggestions of a VLF Archaeopteryx: an emission that bridges the gap between chorus and hiss. *Santolík et al.* [2006] took this idea further by using wavelet techniques on data from the Freja and DEMETER satellites. This analysis allowed them to uncover discrete chorus-like structure hidden within emissions that were ostensibly ELF hiss on traditional spectrograms; they referred to these emissions as “structured hiss.” They used ray tracing techniques to show that emissions generated in the equatorial region outside of the plasmopause, given the proper initial wavenormal angles, could penetrate to very low altitudes (at high latitudes) and possibly to the ground. Stating that “the origin and source region of ‘structured hiss’ and ducted chorus are most probably the same,” *Santolík et al.* [2006] concluded by saying that these observations were “consistent with the

hypothesis that the frequently observed dayside ELF hiss is just the low-altitude manifestation of ... whistler-mode chorus.”

Chum and Santolík [2005] used raytracing to show that chorus waves, generated equatorially at high altitudes, could penetrate the plasmasphere under certain circumstances and potentially become trapped there. *Bortnik et al.* [2008] expanded on these results via a more extensive and rigorous ray tracing study, which showed that chorus waves could penetrate into the plasmasphere and remain there via magnetically reflecting for tens of seconds before being damped. By showing that this phenomenon could occur both on the day and night sides (albeit at reduced efficiencies on the night side), *Bortnik et al.* [2008] concluded on the basis of this study that “chorus waves are the dominant source of plasmaspheric hiss.”

Although theories of hiss as a source of chorus have fallen somewhat out of favor, the possibility that either chorus or lightning could be a source of hiss have seen a recent resurgence in interest. In Chapter 3, we investigate the viability of these two mechanisms.

Chapter 3

Diurnal Dependence of Chorus and Hiss

In this chapter, we present the observation and analysis of 10 months of chorus and hiss emissions observed at Palmer Station from January through October 2003, near the peak of Solar Cycle 23. We classify three separate categories of emissions: chorus occurring without the presence of hiss (*chorus only*), hiss occurring without the presence of chorus (*hiss only*), and chorus and hiss occurring simultaneously (*chorus with hiss*). We find that observed *chorus only* and *chorus with hiss* emissions are confined to the dawn sector, below 6 kHz in frequency. Observed *hiss only* emissions are confined to the dusk sector, below 4 kHz in frequency. We conclude that there are at least two distinct types of hiss observed at Palmer Station: hiss that is observed with chorus in the dawn sector, and hiss that is observed without chorus in the dusk sector. The correspondence of dawn chorus with dawn hiss suggests that these two emissions are strongly related to each other, while the frequency spectrum and local time distribution of dusk hiss, coupled with the absence of simultaneous chorus, suggests that dusk hiss may be generated by terrestrial lightning.

The work presented in this chapter has been published the Journal of Geophysical Research as [Golden et al. \[2009\]](#).

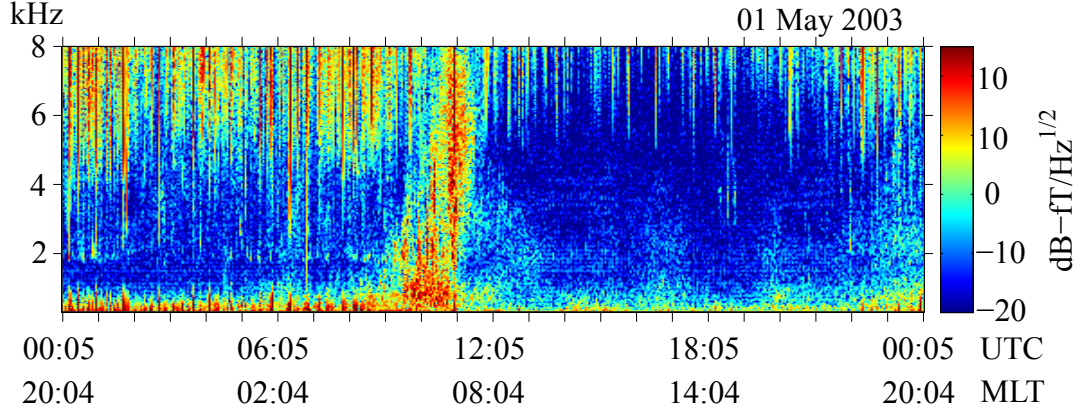


Figure 3.1: 24-hour synoptic spectrogram from Palmer. This view is created by horizontally combining 96 separate 5-second spectrograms, each 15 minutes apart from each other. This particular 24-hour spectrogram from May 1, 2003 shows one of the most intense emissions observed in 2003, consisting of varying forms of chorus and hiss from approximately 08 to 13 UTC (04 to 09 MLT).

3.1 Experimental Methodology

3.1.1 Emission Selection Criteria

Data were collected from Palmer Station from January 1 through October 31, 2003, via the methodology discussed in Section 1.3.1. For each day of this study, we generate a 24-hour combined synoptic spectrogram. These synoptic spectrograms consist of 96 5-second spectrograms stitched together horizontally, in the same format as in the work of *Spasojevic and Inan* [2005]. An example of this type of plot is shown in Figure 3.1. Emissions with power spectral densities greater than $0.1 \text{ fT}/\sqrt{\text{Hz}}$ ($-20 \text{ dB-fT}/\sqrt{\text{Hz}}$) are visually located from these plots via their aberration from the blue background, below the frequency of the lightning-generated sferic impulses.

Potential emissions are scrutinized via a higher resolution spectrogram. For the purposes of this study, without making any a priori assumptions about their generation regions, we characterize emissions based solely on their observed spectral properties, irrespective of their local time or frequency characteristics. Emissions with incoherent spectral properties that do not exhibit any fine structure are labeled

as hiss. Emissions that have obvious “chorus-like” characteristics, such as fine structure and rising tones, whose structure does not resemble that of multiply-hopping whistlers, are labeled as chorus. Often, chorus and hiss are seen simultaneously, in the form of multiple bands of emissions that may separately resemble chorus, hiss, or combinations of the two (such as the “structured hiss” from [Santolík et al. \[2006\]](#)). We consider these emissions separately, and refer to them as “chorus with hiss.”

Throughout the course of this study, we refer to these three emission types separately as *hiss only*, *chorus only* and *chorus with hiss*. Examples of these three emissions can be seen in Figure 3.2. During this study, over the course of the 304 days for which we have valid data, we observed *hiss only* on 70% of days, *chorus only* on 30% of days and *chorus with hiss* on 36% of days.

3.1.2 Cumulative Spectrograms

In order to visualize the entire year’s worth of emissions simultaneously, we use a “cumulative spectrogram” plot. This plot consists of the sum of all of the emissions of a given type, in spectrogram form. Technically, the cumulative spectrogram is generated as follows:

1. The emission database is constructed via the method outlined in Section 3.1.1. The emission database is a list of emissions with the following properties: emission type (one of *chorus only*, *hiss only* or *chorus with hiss*), start time, end time, lower frequency cutoff, upper frequency cutoff.
2. For each emission window (bounded by the start and end times, and the lower and upper cutoff frequencies), the amplitude in dB of the spectrogram for that day, within those bounds, is added to the cumulative spectrogram plot.
3. The resulting spectrogram, which consists of the sum of the emissions from individual spectrograms, is then divided by the number of days for which we have data (304 in this case). This results in a spectrogram of “average intensity.”

The cumulative spectrogram is effectively the product, spectrogram-wise, of the occurrence rate of a given emission type with the average amplitude of that emission

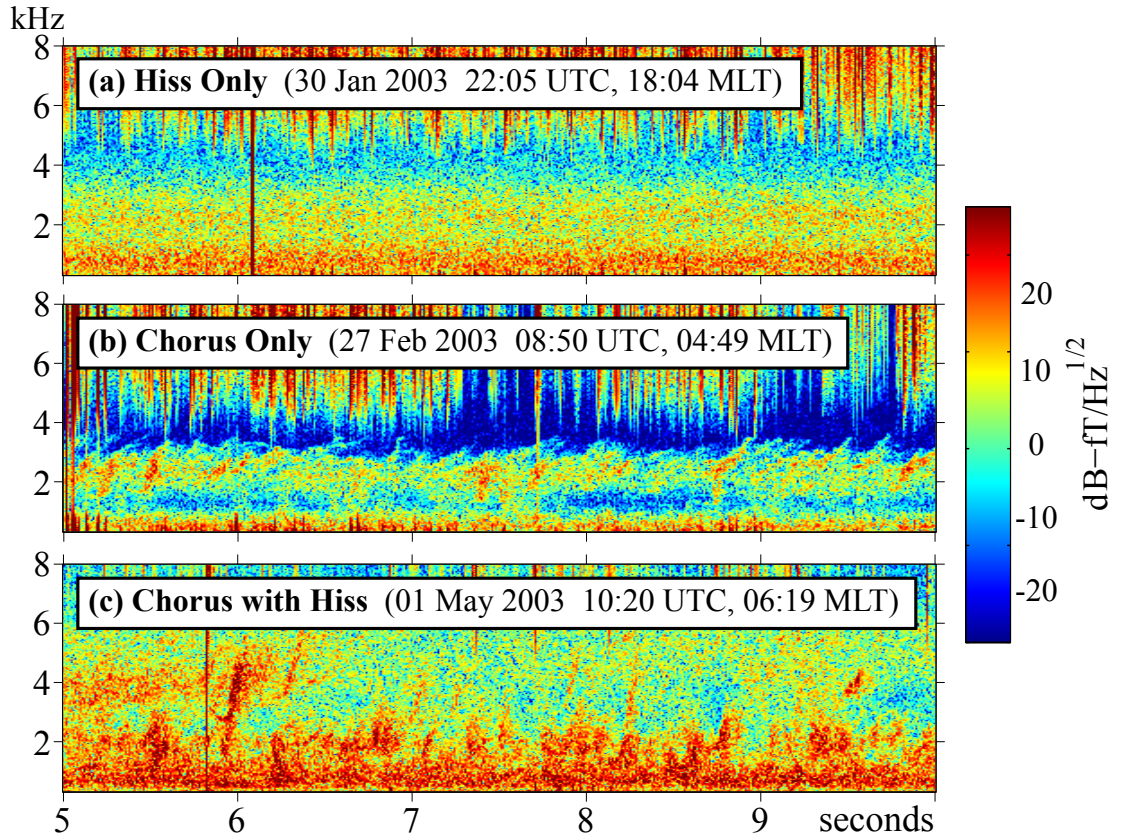


Figure 3.2: Examples of different emission types. (a) *Hiss only* is characterized by incoherent, unstructured emissions with no discrete elements, (b) *Chorus only* consists of closely-spaced, discrete tones, usually rising in frequency and (c) *Chorus with hiss* is a combination of the other two emissions.

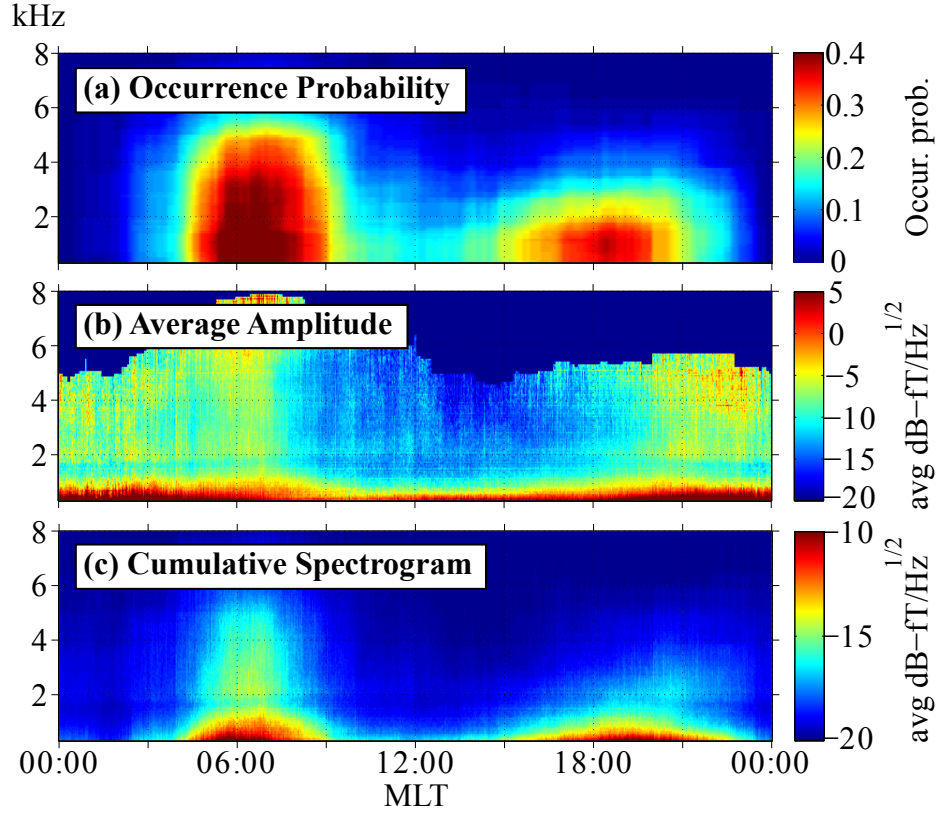


Figure 3.3: Cumulative spectrogram generation procedure. The occurrence rate of a given emission (a) is multiplied by the average amplitude of the emission in dB (b), to give an “average emission amplitude,” weighted by occurrence rate (c). This example shows plots for all emission types combined.

type, as illustrated in Figure 3.3.

3.2 Occurrence Characteristics

3.2.1 Local Time and Frequency

Figure 3.4 shows separate cumulative spectrograms for each emission type. Consistent with previous ground studies of chorus [e.g., [Storey, 1953](#); [Maeda, 1962](#)], *chorus only* emissions are observed exclusively in the dawn sector, from approximately 04 to 09 Magnetic Local Time (MLT). *Chorus with hiss* emissions are observed at the same

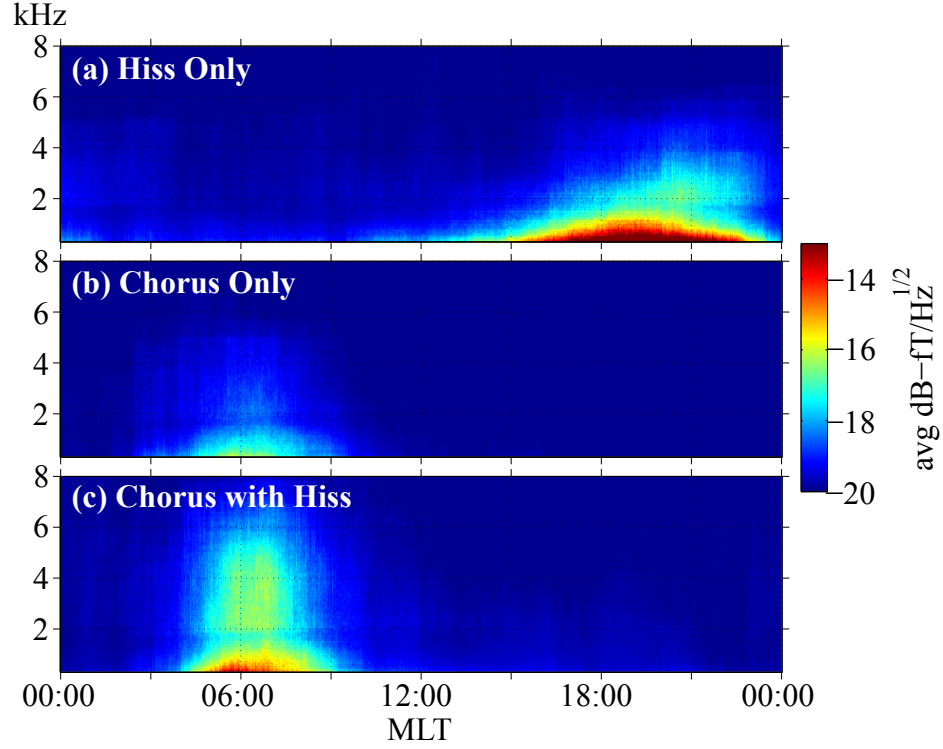


Figure 3.4: Cumulative spectrograms of (a) *hiss only* (408 events), (b) *chorus only* (99 events) and (c) *chorus with hiss* (151 events). *Hiss only* emissions are seen exclusively in the dusk sector, primarily below ~ 1.7 kHz, though they can extend up to ~ 4 kHz. *Chorus only* and *chorus with hiss* emissions appear exclusively in the dawn sector.

local time as *chorus only* emissions, but tend to be more common, and usually extend up to higher frequencies. *Chorus with hiss* emissions most commonly consist of a lower frequency band of chorus-like emission and an upper frequency band of hiss-like emission, though this is not always the case. Thus, the lower frequencies (below ~ 2 kHz) in the *chorus with hiss* cumulative spectrogram of Figure 3.4c are primarily chorus, while the higher frequencies are primarily hiss. The fact that *chorus only* and *chorus with hiss* emissions are seen at the same local times strongly suggests that their generation may be intimately related. Indeed, when characterizing the emissions, we found a continuum of emission types in between *chorus only* and *chorus with hiss* (i.e., varying amounts of structure in “structured hiss”).

Hiss only emissions are observed exclusively in the dusk sector, from 14 to 23

MLT. This is similar to observations by other ground-based sites of similar L shells, although, in contrast to this study, [Laaspere et al. \[1964\]](#) also found a second maximum of hiss in the morning at North American stations at similar latitudes to Palmer, namely Washington D.C. ($L=2.5$) and Dartmouth College ($L=3.1$). [Hayakawa et al. \[1975a\]](#) found a similar double-peaked distribution at Moshiri, Japan ($L=1.6$). This is possibly attributable to their characterizing as “hiss” what we refer to as *chorus with hiss* in the morning.

Using data from the GEOS spacecraft at high radial distances ($\geq 6 R_E$), [Cornilleau-Wehrlin et al. \[1978\]](#) also saw a majority of *chorus with hiss* emissions (with chorus as the greater amplitude emission) in the morning, suggesting that *chorus with hiss* emissions originate at high altitudes outside of the plasmopause, just as *chorus only* emissions do. In contrast to this study, they saw very few hiss emissions without accompanying chorus, but this is readily explained by the fact that the study was limited to satellite radial distances greater than $6 R_E$, which is outside the source region of hiss, particularly at low levels of magnetic activity [[Meredith et al., 2004](#)].

Conspicuous in their absence are emissions in the noon sector and midnight sector. Using data from the Ogo 5 satellite [Tsurutani and Smith \[1977\]](#) showed that the L shell of maximal chorus occurrence increases from postmidnight to postdawn as a result of drift shell splitting, which is one reason why chorus would be unlikely to be seen at Palmer’s L shell outside of the dawn sector. Additionally, ionospheric absorption is a maximum during the daytime, due to the increased electron density from solar radiation [e.g., [Helliwell, 1965](#), Fig. 3-35], which has the net result of preventing magnetospheric emissions from reaching middle and low latitudes on the ground, regardless of their originating L shell (see Section 5.2 for more details). In the midnight sector, measurements using the CRRES satellite by [Meredith et al. \[2001\]](#) and [Meredith et al. \[2004\]](#) found a minimum of chorus at low L shells and plasmaspheric hiss at all L shells, respectively, so it is likely that the absence of emissions at Palmer in the midnight sector represent a true lack of emissions in the magnetosphere at Palmer’s L shell.

Chorus only and *chorus with hiss* intensities gradually fall off as frequency increases from 300 Hz (the lowest frequency of these measurements) to around 6 kHz,

with a noticeable discontinuity in intensity near 1.7 kHz. This discontinuity is due to the lower cutoff of the transverse electric (TE) mode in the Earth-ionosphere waveguide; below this cutoff, the transverse electromagnetic (TEM) mode dominates, with attenuation coefficient increasing with increasing frequency. This discontinuity is also visible at ~ 1.7 kHz for *hiss only* for the same reason.

Below ~ 1.7 kHz, both emission distributions gradually rise and then fall in frequency with local time; this is consistent with the ionospheric entry region of the waves remaining at a constant set of local times and latitudes over the course of the Earth's rotation. Since higher frequencies in the TEM mode suffer greater attenuation while propagating in the Earth-ionosphere waveguide than do lower frequencies, the emissions' highest frequency components will only be visible when Palmer's local time is coincident with the local time of the emissions' ionospheric penetration. As the Earth continues to rotate past this point, Palmer moves further away from the ionospheric entry region for the emissions, and increased attenuation for high frequencies becomes apparent.

There are also *chorus with hiss* emission components propagating in higher order modes observed above the 1.7 kHz cutoff frequency between 04 and 08 MLT. These emissions extend less broadly in time than the main low-frequency peak of *chorus with hiss* emissions. It is not clear whether this is the result of a propagation effect (either attenuation within the Earth-ionosphere waveguide, or suffered during penetration of the ionosphere), or a source effect. The higher frequencies of *chorus with hiss* emissions are typically where hiss is observed, while chorus is observed at the lower frequencies.

Observed *hiss only* emissions also display an upper frequency component, above the 1.7 kHz cutoff, which increases in frequency from 1.7 to ~ 4 kHz over the course of the emission interval, as has been seen before in previous work [e.g., [Vershinin, 1970](#); [Carpenter et al., 1975](#)]. The rising frequency of the upper component is apparent, despite the nonlinear attenuation effects introduced by propagation in the Earth-ionosphere waveguide, which cause the upper frequency component to appear to “separate” from the lower frequency component of the hiss. [Hayakawa et al. \[1988\]](#)

specifically interpreted the pre-midnight frequency drift of hiss in terms of a quasi-linear electron cyclotron instability model.

The average spectra of the three emission types are shown in Figure 3.5. Note that the amplitude scale of the spectra of Figure 3.5 is not directly comparable to that of the cumulative spectrograms of Figure 3.4, because it is computed in a different way. The spectra of Figure 3.5 is computed by averaging the power spectra of all emissions of a given type. In this way, it provides a measure of the average power spectrum only when an emission is present. This is in contrast to the average power spectrum at all times (including quiet periods) shown in Figure 3.4, which also incorporates the occurrence probability at the given time and frequency.

The characteristic rapid attenuation with increasing frequency of the TEM mode in the Earth-ionosphere waveguide is visible in Figure 3.5 for frequencies below 1.7 kHz. Above 1.7 kHz, the wave energy is contained in higher order modes. *Chorus only* emissions extend up to approximately 5 kHz, *hiss only* emissions extend to 7 kHz and *chorus with hiss* emissions can be seen just beyond 8 kHz. It is important to note that, although some emissions may have high-frequency components, the likelihood of seeing any given emission type rapidly drops off with increasing frequency, as shown in a plot of emission occurrence versus frequency in Figure 3.6. Note that, below ~ 500 Hz, the main constituent of the observed spectrum is interference from spheric slowtails from terrestrial lightning.

These results are particularly interesting in the context of currently accepted definitions of mid-latitude and plasmaspheric hiss, as discussed in Section 2.3.1. Specifically, Sonwalkar [1995] states that mid-latitude hiss, which has a lower cutoff of ~ 2 kHz, is the only type of hiss visible on the ground at mid-latitude stations like Palmer (contrasted with auroral hiss, which is visible at high-latitude ground stations). Plasmaspheric hiss, which occupies the portion of the hiss spectrum below ~ 2 –3 kHz is said not to be visible on the ground. However, as Figures 3.5 and 3.6 show, *hiss only* is readily seen at Palmer from below 1 kHz to nearly 7 kHz. This suggests one of three scenarios: (1) that mid-latitude hiss may in fact extend below 3 kHz, (2) that plasmaspheric hiss, as well as mid-latitude hiss, can penetrate to the ground at mid-latitudes, in contrast to the prevailing belief that observations of

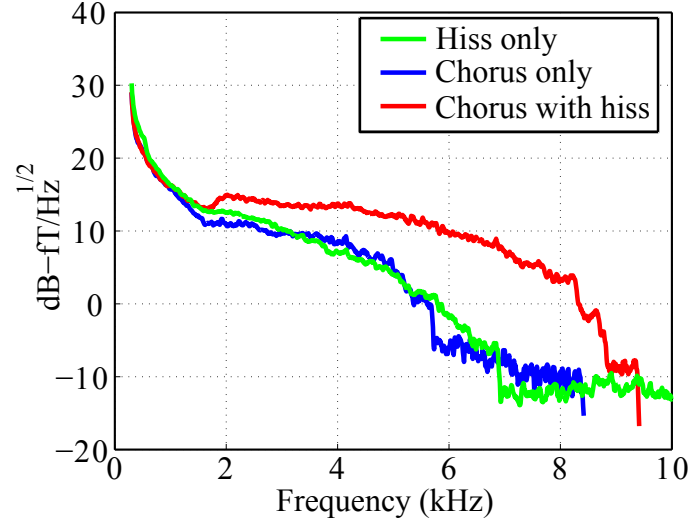


Figure 3.5: Cumulative emission spectra. The high amplitudes below ~ 500 Hz are due to sferic slowtails.

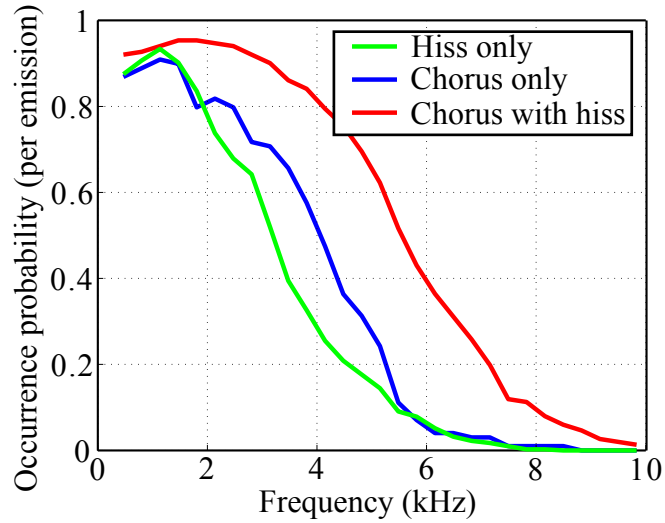


Figure 3.6: Cumulative occurrence probability (per emission) as a function of frequency.

plasmaspheric hiss are confined to space-based measurements, or (3) that the dusk hiss at Palmer represents an entirely different type of hiss, such as exo-hiss. Because the frequency spectrum of observed hiss is most similar to that of plasmaspheric hiss, and because it is observed when Palmer is well within the plasmasphere, we interpret the observed hiss as plasmaspheric hiss.

3.2.2 Occurrence Rates and Correlation with AE

The appearance of chorus and hiss has long been known to correlate with the occurrence of substorms, as measured by the auroral electrojet (AE) index [e.g., [Meredith et al., 2001, 2004](#)] (see also Section 1.1.3). When investigating the dependence of emission occurrence on AE , we look for emissions occurring during their usual “emission intervals,” as determined by Figure 3.4. For *chorus only* and *chorus with hiss*, we define the emission interval to be between 03 and 09 MLT. For *hiss only*, we define the emission interval to be between 14 and 23 MLT. We define the AE^\dagger index to be the maximum value of the true AE index in the six hours preceding the center of the given emission’s emission interval. This is analogous to the definition for AE^* from [Meredith et al. \[2004\]](#), which is defined as the maximum value of AE in the three hours prior to the emission; we elect to use AE^\dagger over AE^* , because we found that it is better correlated with our ground-based data. Figure 3.7, shows the normalized occurrence rates of *chorus only*, *hiss only* and *chorus with hiss* with respect to AE^\dagger .

Consistent with past results, all three emission types generally increase in probability as AE^\dagger increases. The AE^\dagger dependence of *chorus only* contrasts with that of *chorus with hiss*, the latter being the most strongly AE^\dagger associated emission type. In particular, we note that when $AE^\dagger > 500$ nT, we see *chorus with hiss* more often than *chorus only*, and nearly twice as often when $AE^\dagger > 800$ nT. Because we know from Figure 3.4 that *chorus only* and *chorus with hiss* share the same local time emission interval, this further suggests that *chorus only* and *chorus with hiss* are in fact two manifestations of the same chorus-producing phenomena, which has a tendency to induce hiss alongside the chorus when the AE index is increasingly disturbed. *Hiss only* occurrence is also well correlated with increasing values of AE^\dagger , and it is further

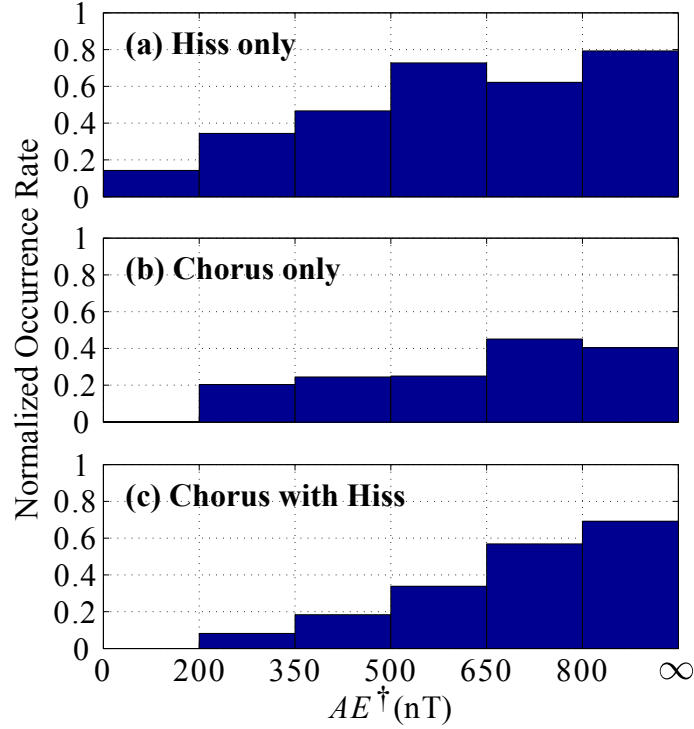


Figure 3.7: Dependence of (a) *hiss only*, (b) *chorus only* and (c) *chorus with hiss* on AE^\dagger index. All bins have at least 35 days of data (mean number of days = 51, st. dev. = 10).

interesting to note that *hiss only* is the only emission seen during the lowest levels of substorm activity, $AE^\dagger < 200$ nT.

Figure 3.8 shows all emission types combined into a single cumulative spectrogram, and as a function of the AE^\dagger index. We show all emissions for all values of AE^\dagger , as well as all emissions for $AE^\dagger < 600$ nT and all emissions for $AE^\dagger > 700$ nT. The split point of $AE^\dagger = 650$ nT was chosen because that is the value for which there is an equal number of emissions above and below it (289 emissions for $AE^\dagger < 600$ nT and 288 emissions for $AE^\dagger > 700$ nT, respectively). We do not plot emissions for $600 \text{ nT} \leq AE^\dagger \leq 700 \text{ nT}$ because we assume that their characteristics will be very similar. The small, but visible discontinuity in Figure 3.8b,c at 20 MLT is an artifact of our processing; it appears because midnight UTC occurs at 20 MLT, where one Palmer-generated spectrogram ends and another begins (as in Figure 3.1).

We note from Figure 3.8 that the higher frequencies of *chorus with hiss* emissions (above ~ 1.7 kHz) tend to appear more frequently and at higher intensity for $AE^\dagger > 700$ nT. In general, when observing *chorus with hiss* emissions, the energy at higher frequencies is often composed primarily of hiss. The lack of energy at higher frequencies in Figure 3.8b indicates that chorus appears without hiss at lower AE^\dagger levels, and with hiss at higher AE^\dagger levels, consistent with the above result from Figure 3.7.

Hiss only emissions are also susceptible to changing geomagnetic conditions, in a very different way. At lower levels of AE^\dagger , we find that *hiss only* emissions extend from approximately 14 to just past midnight MLT, and have very intense amplitude at lower ELF frequencies ($f < 500$ Hz). In contrast, for high AE^\dagger levels, the lower frequency ELF components of hiss are reduced, and the local time occurrence moves earlier, to 10 to 22 MLT. This result is in contrast to that of Meredith *et al.* [2006], Section 6.3, who found no geomagnetic control of hiss on the night side. However, we note that Meredith *et al.* [2006] divided day and night at 18 MLT, which is near the middle of the dusk hiss peak at Palmer; separately analyzing the two halves of the hiss peak may have reduced the efficacy of their analysis. Nonetheless, there is obvious geomagnetic control in Figure 3.8 of dusk hiss after 18 MLT (during Meredith *et al.* [2006]’s “night”).

3.3 Discussion

Our results show two distinct types of hiss that are observed at Palmer, which we will refer to as “dawn hiss” and “dusk hiss.” Dawn hiss is observed exclusively in the dawn sector, is generally (but not exclusively) seen above ~ 2 kHz, often shows structure, and is always accompanied by chorus. In contrast, dusk hiss is observed exclusively in the dusk sector, is rarely seen above ~ 4 kHz, rarely shows structure, and is never observed with chorus. The frequency spectrum of dawn hiss observed at Palmer most closely resembles that of mid-latitude hiss, while the spectrum of dusk hiss at Palmer resembles that of either plasmaspheric hiss or exo-hiss.

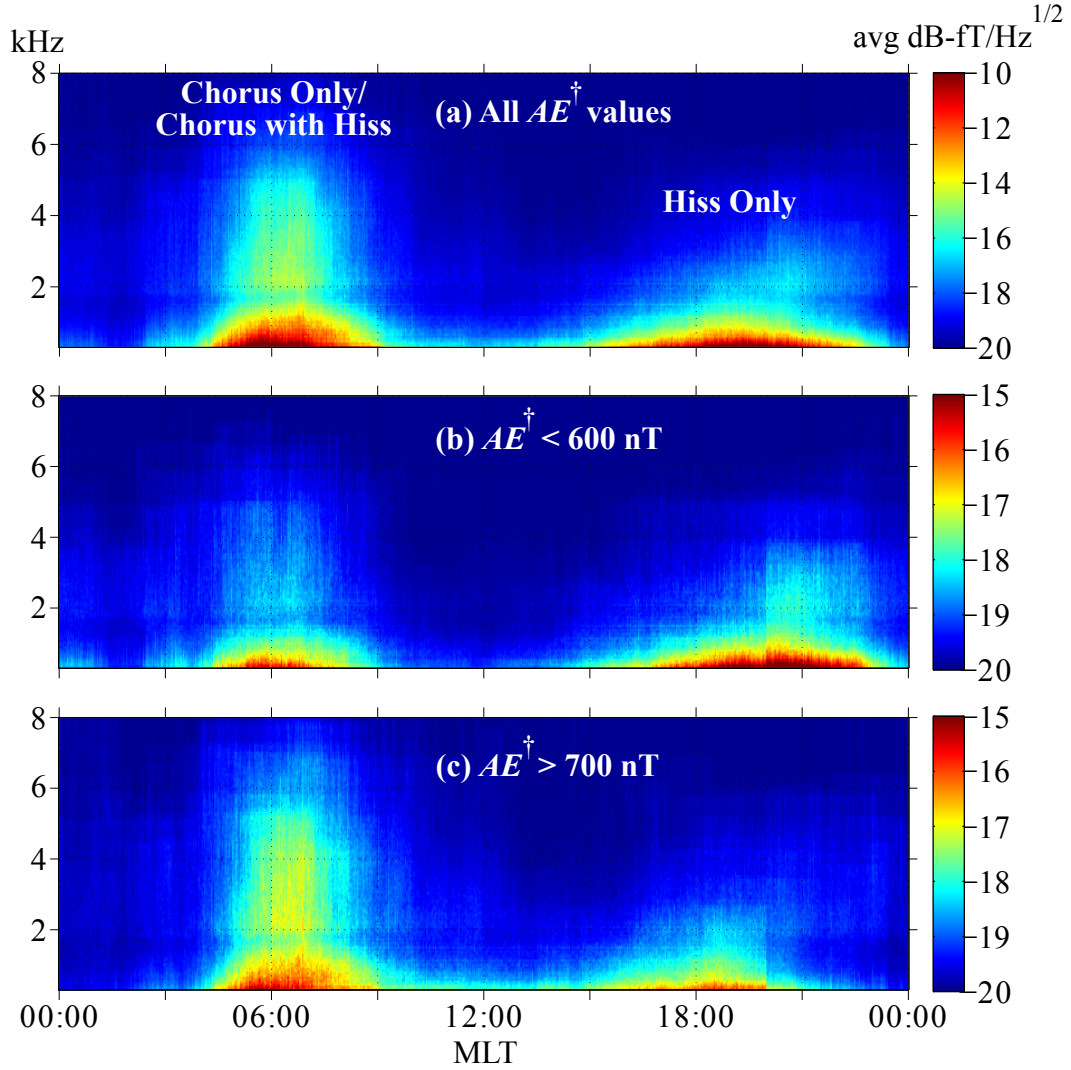


Figure 3.8: Cumulative spectrogram of (a) all chorus and hiss emissions (660 events), (b) all emissions for $AE^{\dagger} < 600$ nT (289 events) and (c) $AE^{\dagger} > 700$ nT (288 events). *Chorus only* and *chorus with hiss* are observed exclusively on the dawn side, while *hiss only* is observed exclusively on the dusk side. AE^{\dagger} affects frequency occurrence for all emissions, and the local time occurrence for *hiss only* emissions.

3.3.1 Chorus as a Source of Hiss

That chorus and hiss are often observed together is a concept that is by no means novel. What is currently a new idea is that chorus may in fact be the dominant source of hiss, and that the one becomes the other via an overlapping and “smearing” of the spectrum, thus causing chorus emissions to lose the definition of their discrete elements, and eventually appear hiss-like to observers. [Santolik et al. \[2006\]](#) and [Bortnik et al. \[2008\]](#) have separately stated, based on ray tracing studies, that chorus may be the primary source of ELF hiss and plasmaspheric hiss, respectively.

The many observations of chorus emissions occurring simultaneously with hiss emissions, both in past works and in this chapter, give credence to the claim that chorus may indeed be responsible for generating certain types of hiss. In particular, it seems quite reasonable that the dawn hiss shown in this chapter, whose frequency band resembles mid-latitude hiss, could be generated by discrete chorus emissions. The exclusive occurrence of dawn hiss with dawn chorus, and the fact that dawn hiss is so often of the “structured hiss” variety, both support the idea that mid-latitude hiss may be caused by chorus.

The most common variety of *chorus with hiss* seen at Palmer consists of one band of chorus at a lower frequency and one band of hiss at a higher frequency (although other varieties, such as overlapping bands of chorus and hiss, or bands of hiss below bands of chorus are possible). Although it is not reasonable to claim that chorus in one frequency band may be the source of simultaneously-observed hiss in a separate band, it is certainly possible that chorus, originally occurring in multiple frequency bands, has either had one of its bands generated with hiss-like structure, or has had that band converted into hiss over the course of its propagation. The former scenario is supported by the observations of [Cornilleau-Wehrlin et al. \[1978\]](#), who made many observations of *chorus with hiss* beyond the plasmopause, presumably close to the source region, which suggests that the conversion process happens very close to, or at, the source. However, the latter scenario is supported by [Santolik et al. \[2006\]](#) and [Bortnik et al. \[2008\]](#), who suggest that chorus waves may convert to hiss via superposition and dispersion during their propagation. It is not clear at this time which conversion process is dominant.

The fact that we usually see hiss or structured hiss in a band above chorus, coupled with the fact that chorus frequency tracks the electron gyrofrequency at its source region [*Burtis and Helliwell, 1976*], suggests that it may specifically be chorus generated at lower L shells (where the equatorial electron gyrofrequency is higher) that gives rise to hiss, whereas chorus generated at higher L shells (where the equatorial electron gyrofrequency is lower) remain structured as chorus. Again, this conversion process may occur either at the source, or during the chorus propagation. If the conversion occurs during chorus propagation, it is possible that the conversion region is small; this fact would not preclude chorus generated at low L shells from being favored to convert over chorus generated at higher L shells, despite the fact that chorus generated at low L shells has a shorter distance to travel before it reaches the ionosphere.

As seemingly plausible as it is that dawn hiss is caused by chorus, it seems equivalently unlikely that the dusk hiss observed at Palmer is related to chorus. The fact that very few emissions are seen at Palmer in between the diurnal peaks of dawn *chorus only/chorus with hiss* and dusk *hiss only*, as well as the lack of structure in dusk hiss emissions, strongly suggest that the emissions that occur at these two separate local times are unrelated. It is also quite unlikely that chorus, being observed very infrequently in the dusk sector *in situ* [*Tsurutani and Smith, 1977; Meredith et al., 2001*], could propagate azimuthally from the dawn to the dusk sector before being observed as hiss. Whether dusk hiss is exo-hiss or plasmaspheric hiss, past studies of the local time distribution of chorus, as well as chorus observations from this study, do not support the hypothesis that dusk hiss is generated by magnetospheric chorus.

3.3.2 Lightning as a Source of Hiss

There has recently been a resurgence of interest in the role of lightning as a source of plasmaspheric hiss, either embryonically, as proposed by *Sonwalkar and Inan [1989]* or as a result of multiple magnetospheric reflections within the plasmasphere, as proposed by *Draganov et al. [1992]*. *Green et al. [2005]* suggested that lightning is the dominant source of plasmaspheric hiss over the frequency range of ~ 500 Hz to

3 kHz, though the particular frequency range was contested by a subsequent study by [Meredith et al. \[2006\]](#), who concluded that the lightning-associated hiss was limited to frequencies above 2 kHz.

The local time peak of dusk hiss at Palmer is suggestive of afternoon lightning as a source. Particularly compelling is the fact that dusk hiss peaks at Palmer at around 19 MLT, which corresponds to 17–18 MLT for the Eastern half of North America, a major source of lightning during the boreal summer [[Christian et al., 2003](#)]. This local time peak is quite close to the ~ 16 MLT peak of lightning worldwide [e.g., [Bailey et al., 2007](#)]. The ~ 2 -hour discrepancy between the diurnal peaks of terrestrial lightning and dusk hiss at Palmer may be an ionospheric effect, since ionospheric absorption is greater during daylight hours than at night [e.g., [Helliwell, 1965](#), Fig. 3-31]; this would have the artificial effect of damping observed hiss amplitudes during the daytime.

Whistlers can be seen quite often at Palmer, varying from a peak of 22 whistlers per minute during the boreal summer (local winter) night, to a minimum of 0.3 whistlers per minute during the day in the boreal winter, according to calculations by [Burgess \[1993\]](#), based on earlier audio recording measurements by [Laaspere et al. \[1964\]](#) at a nearby Antarctic station. We also occasionally see evidence of whistlers directly causing or contributing to bands of hiss at Palmer. Figure 3.9 shows an example of a whistler undergoing many cross-hemisphere hops, merging with an existing hiss band. Over the course of the two minutes shown in Figure 3.9, the whistler, at first highly visible on the spectrogram, completely merges with the hiss and becomes indistinguishable from unstructured hiss at the end of the second minute. Although this phenomenon is not seen very often at Palmer, the lack of observations may be due to fact that the “triggering” mechanism of the whistler lasts for such a short amount of time. We hypothesize that these multiply-hopping whistlers may contribute to the dusk hiss at Palmer, either as the result of many overlapping, dispersed whistlers [e.g., [Dowden, 1971](#)], or possibly in conjunction with the type of embryonic onset reported by [Sonwalkar and Inan \[1989\]](#). However, until either more cases can be found that show evidence of triggering onset, or until the absence of such observations can be theoretically explained, we cannot suggest that these particular mechanisms of whistler-induced hiss are the *dominant* source of dusk hiss.

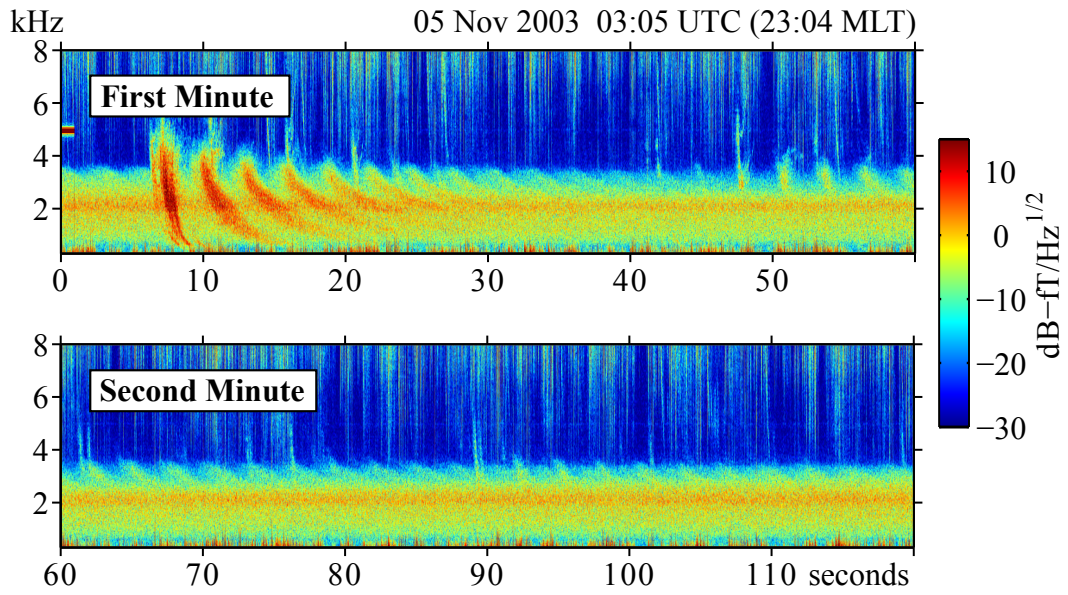


Figure 3.9: A multiply-hopping whistler, whose multitude of cross-hemisphere hops gradually overlap with an existing hiss band. The original whistler is seen in the first minute (top), and quickly merges with the existing hiss band, becoming indistinguishable from standard structureless hiss in the second minute (bottom). This type of phenomenon supports the idea that dusk hiss observed at Palmer may be caused by lightning.

Green et al. [2005] and *Meredith et al.* [2006] found no evidence of lightning control below 500 Hz and 2 kHz, respectively. However, we must critically interpret their conclusions. If these lower-frequency waves were caused by terrestrial lightning flashes, then certain propagation effects would make them inherently difficult to spatially correlate with their terrestrial source region. As noted on page 9 of *Meredith et al.* [2006], lower frequency waves are capable of propagating outward in the magnetosphere to L shells quite distant from their terrestrial source [*Bortnik et al.*, 2003]. Additionally, the lower attenuation for lower frequencies in the TEM mode in the Earth-ionosphere waveguide (particularly over seawater) allows waves to potentially propagate subionospherically very far from their source before leaking into the magnetosphere. Thus, we conclude that spatial correlation with landmass is not a requirement for lightning as the source of lower frequency waves. Finally, although we note from Figure 3.7 that *hiss only* emissions are well-correlated with geomagnetic activity, this fact is not mutually exclusive with the theory that hiss is sourced by terrestrial lightning. *Sonwalkar and Inan* [1989], for example, hypothesized that lightning-generated whistlers are an *embryonic* source of plasmaspheric hiss, which suggests that a source population of energetic particles, such as those injected into the plasmasphere via magnetic storms, are still necessary for the growth of hiss to observable levels.

3.4 Summary

Dawn hiss at Palmer is regularly observed with chorus and may in fact be generated by chorus either via diffuse generation at the chorus source region or via an overlapping and smearing of the chorus frequency band over the course of the chorus propagation. Dusk hiss seen at Palmer, which is either exo-hiss or unexpected ground-based observations of plasmaspheric hiss, appears to be consistent with the idea of lightning as a source but is not consistent with chorus as a source. Significant work remains to determine the relation between hiss observed at Palmer and in space and to conclusively determine the sources for the dawn and dusk hiss observed at Palmer.

Chapter 4

Plasmaspheric Control of Chorus Propagation

In this chapter, we investigate the manner in which the plasmopause is responsible for dictating which magnetospheric source regions of ELF/VLF chorus are able to propagate to and be received by mid-latitude stations on the ground. First, we explore the effects of plasmasphere extent on ground-based observations of chorus via a three-month study of measurements of chorus at Palmer Station combined with data on the plasmasphere extent from the IMAGE EUV instrument. Chorus normalized occurrence peaks when the plasmopause is at $L \sim 2.6$, somewhat higher than Palmer's L shell, and this occurrence peak persists across a range of observed chorus frequencies.

Next, reverse raytracing is employed to evaluate the portion of the equatorial chorus source region, distributed in radial distance and wavenormal, from which chorus is able to reach Palmer Station via propagation in a non-ducted mode. The results of raytracing are similar to those of observations with a peak of expected occurrence when the plasmopause is at $L \sim 3$. The exact location of the peak is frequency-dependent. This supports the conclusion that the ability for chorus to propagate to low altitudes and the ground is a strong function of instantaneous plasmasphere extent, and peak occurrence of chorus at a given ground station may occur when the L shell of the plasmopause is somewhat beyond that of the observing station. These

results also suggest that chorus observed on the ground at mid-latitude stations propagates predominantly in the non-ducted mode.

The work presented in this chapter has been published the Journal of Geophysical Research as [Golden et al. \[2010\]](#).

4.1 Motivation

This study is motivated by the study presented in Chapter 3. During the course of that study, which spanned 10 months in 2003, chorus was observed on more than 50% of days. This high observance rate was unexpected for several reasons. First, as discussed in Section 2.3.1, chorus is generated outside the plasmasphere. In addition, as discussed in Section 1.2.2, chorus observed on the ground has traditionally been interpreted as a ducted emission, and therefore, that the L shell on which it is received is approximately the same as the L shell on which it is generated. However, in the study presented in Chapter 3, the magnetospheric conditions were such that the plasmopause was often expected to be well beyond Palmer's L shell during chorus observations. During that study, chorus was observed for $K_p \lesssim 2+$. According to the plasmopause model of [Carpenter and Anderson \[1992\]](#), at $K_p = 2+$, the plasmopause is expected to be around $L \sim 4.5$. It is only for $K_p > 6+$ that the plasmopause is expected to reach down to $L < 2.5$. Also, the frequency range of observed chorus suggests that the source region of the waves is well beyond Palmer's L shell. Lower-band chorus is generated for frequencies in the range $0.1f_{ceq} \leq f \leq 0.5f_{ceq}$, and waves of frequencies below 500 Hz were observed. Waves of this low frequency are expected to be generated at $L > 5.5$ under a dipole model of the Earth's magnetic field [[Burtis and Helliwell, 1976](#)].

It seems clear that the observations from Chapter 3 are inconsistent with the theory of ducted propagation of chorus and that the dominant mode of chorus reception at mid-latitude stations like Palmer may instead be non-ducted, as has been proposed recently [[Chum and Santolík, 2005](#); [Bortnik and Thorne, 2007](#); [Gołkowski and Inan, 2008](#)]. Specifically, [Chum and Santolík \[2005\]](#) have shown via raytracing that non-ducted chorus, generated in the equatorial magnetosphere with wavenormal angles

near the local Gendrin angle, may be able to reach the ionosphere and penetrate to the ground at L shells significantly below those at which the waves are generated. Although *Chum and Santolik* [2005] did not include a plasmasphere in their analysis, it seems logical, given the exo-plasmaspheric source of chorus and the location of Palmer within the plasmasphere, that the location of the plasmopause may play an important role in determining which subsets of chorus may be able to be received at Palmer.

In this study, we address two broad questions. (1) What is the location of the plasmopause when chorus is observed at Palmer? (2) How does the location of the plasmopause affect the portion of the chorus source region that is able to propagate to the ground and be received at Palmer? These questions are answered via a combination of (i) a three-month statistical study of chorus observations at Palmer Station coupled with simultaneous measurements of the plasmopause using the Extreme Ultraviolet (EUV) instrument on board the IMAGE satellite, and (ii) a model-based study of chorus propagation effects via a new Stanford VLF 3D raytracing software package, used to model magnetospheric propagation and Landau damping under different models of the plasmopause location, as well as a full wave code, used to model electromagnetic propagation in the Earth-ionosphere waveguide.

4.2 Experimental Methodology

In order to determine the location of the plasmopause when chorus is observed at Palmer Station, we employ two separate databases: a database of emissions observed at Palmer and a database of plasmopause locations at Palmer's MLT. Both databases span three months, from April through June 2001, and are discussed below.

4.2.1 Palmer Emission Database

The year 2001 falls approximately on the peak of Solar Cycle 23, and chorus occurrence is frequent at Palmer Station during this period. A combination of automated emission detection (an early version of that discussed in Chapter 5) and manual

correction is used to determine the presence of emissions. The automated detector rejects confounding impulsive electromagnetic signals, such as sferics and whistlers, and focuses on chorus and hiss. Chorus is then distinguished from hiss based on its “burstiness,” namely, the frequency content of the amplitude modulation of the broadband signal. Bursty signals are classified as chorus, and non-bursty signals are classified as hiss, and discarded. The output of the automated detector is then manually verified to eliminate false positives (e.g., hiss or lightning-generated whistlers erroneously labeled as chorus) and false negatives (e.g., weak chorus emissions that may have been rejected based on their proximity to sferics or other emissions). Although it is likely that some chorus emissions with low signal-to-noise ratios are erroneously rejected by this algorithm, the profusion of detected chorus emissions still leads to statistically-significant results.

At each 15-minute synoptic epoch (defined in Section 1.3.1), a binary judgment is made about whether chorus is observed or not, based on the results of both the automated detector and manual inspection. The resulting table of true/false values for chorus observation versus time then becomes the database of Palmer chorus emissions. As an overview, Figure 4.1 shows a cumulative spectrogram of the chorus emissions used in this study. The cumulative spectrogram is effectively the logarithmic sum of the spectrums of its constituent emissions, and is a measure of the average chorus spectrum with respect to frequency and local time; the full procedure is described in Section 3.1.2. The gap at ~ 1.7 kHz on the cumulative spectrogram is a result of increased attenuation below the first transverse electric (TE_1) waveguide mode cutoff during propagation in the Earth-ionosphere waveguide. Only emissions in the boxed region, in the range $4 \leq \text{MLT} \leq 10$ are used in this study.

4.2.2 Plasmapause Location Database

In order to determine the instantaneous plasmapause location at each synoptic epoch, data from the Extreme Ultraviolet (EUV) instrument [*Sandel et al.*, 2000] on board the IMAGE satellite [*Burch*, 2000] are used. The EUV instrument images resonantly scattered sunlight from He^+ ions, which are a minority constituent of the plasma in

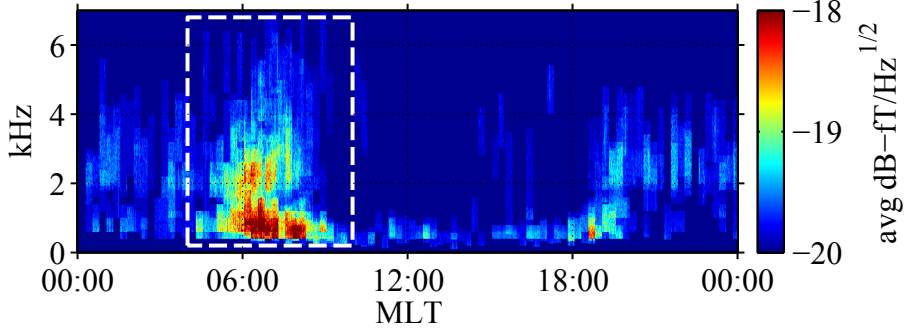


Figure 4.1: Cumulative spectrogram of chorus emissions from April through June, 2001. Only emissions in the boxed area, between 04 and 10 MLT, are used in this study.

the Earth’s plasmasphere. The He^+ edge, as seen by the EUV instrument, has been shown to be an accurate proxy for the plasmopause [Goldstein *et al.*, 2003], which is the region of the magnetosphere where the electron density exhibits a steep drop with increasing L value.

Because this study focuses on emissions observed on the ground at Palmer, the extent of the plasmopause is only considered at Palmer’s magnetic local time, $\text{MLT} = \text{UTC} - 4.0$. Raw EUV images are initially mapped to the equatorial plane using the minimum L technique of Roelof and Skinner [2000, Sec. 2.2], assuming a dipole model for the Earth’s magnetic field. The radial extent of the plasmopause is then manually selected on each individual EUV image at $\text{MLT} = \text{UTC} - 4.0$ and that plasmopause value is added to the database. EUV images where the plasmopause cannot be found due to excessive noise or EUV camera malfunction, or where the plasmopause is either poorly defined or not visible below $L=6$, are discarded. After removing data gaps from both databases, 1033 synoptic epochs, or approximately 260 hours of data, remain for this study.

4.3 Dependence of Chorus Observations on Plasmasphere Extent

4.3.1 Choice of AE Metric

Since this study concerns the role of the plasmopause in dictating the observation of chorus emissions, it is instructive to make mention of how the plasmopause is correlated with the AE index, which is itself well correlated with the observation of chorus emissions [e.g., [Meredith et al., 2001](#)] (see also Section 1.1.3). This is done to explore a potential confounding effect where a single event, namely a magnetic substorm, may have two simultaneous consequences: (1) enhancement of the auroral electrojet, causing an increase in AE and (2) erosion of the plasmasphere.

Figure 4.2 shows the extent of the plasmopause, sampled at $MLT = UTC - 4.0$ for $04 \leq MLT \leq 10$, plotted against the instantaneous AE index (left), and the average AE in the previous 12 hours (right) over the three-month period of this study. Averaging the AE index over $N=12$ hours yields approximately the greatest correlation for any value of N . The plasmopause is moderately correlated with the log of instantaneous AE , with correlation coefficient $\rho = -0.43$ and residual standard deviation $\sigma_{\text{err}} = 0.75$ L, and highly correlated with the log of the average AE in the previous 12 hours, with correlation coefficient $\rho = -0.81$ and residual standard deviation $\sigma_{\text{err}} = 0.49$ L.

However, the manner in which AE is associated with plasmasphere extent differs from how it is expected to be associated with chorus occurrence. The time between when AE is enhanced and when chorus is expected to be seen at Palmer may be determined by calculating the expected time required for a chorus source particle to drift from 00 MLT to 06 MLT. Based on [Walt \[1994, Fig. B.2\]](#), 100 keV electrons at $L=4$ will drift from midnight to 06 MLT in ~ 21 min; higher-energy particles will drift more quickly. This time period is on the order of the synoptic epoch used in this study (15 min). Therefore instantaneous AE is used as the metric for predicting chorus in this study. It is significant that, while instantaneous AE is expected to be a good predictor of chorus occurrence, it is only weakly correlated with plasmasphere extent.

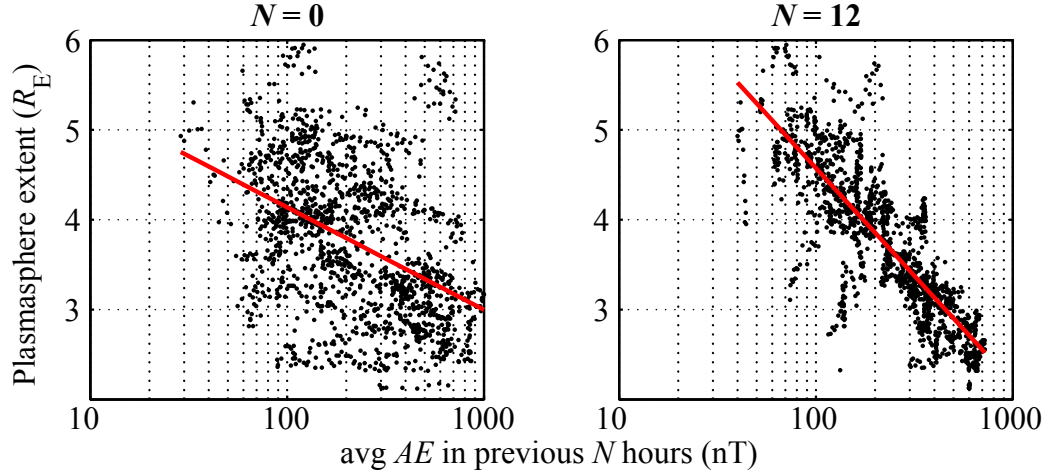


Figure 4.2: L shell of plasmopause at $\text{MLT} = \text{UTC} - 4.0$ within the range $04 \leq \text{MLT} \leq 10$ plotted against (left) instantaneous AE and (right) average AE in the previous 12 hours. Plasmasphere extent is moderately correlated with instantaneous AE and highly correlated with average AE in the previous 12 hours. In each plot, the solid red line is a linear fit between plasmasphere extent and the logarithm of AE .

This suggests that source effects, as measured by instantaneous AE , and propagation effects, as measured by plasmasphere extent, may exert independent control over the probability that chorus will be seen at Palmer at any given time.

4.3.2 Chorus Occurrence versus Plasmasphere Extent

In this section, the dependence of chorus normalized occurrence on plasmasphere extent is examined. The additional complication of AE is deferred to the multivariate analysis of the next section. Although the detailed structure of the plasmopause boundary layer is complex [Carpenter and Lemaire, 2004], the major plasmopause structure is assumed to be field-aligned over much of its range. For the purposes of this study, the plasmasphere extent can therefore be described via the scalar quantity L_{PP} , which represents the L shell of the plasmopause under a dipole approximation to the geomagnetic field. A scatter plot of chorus observations at each synoptic epoch versus instantaneous AE and L_{PP} is shown in Figure 4.3. Synoptic epochs with chorus are indicated with blue squares and epochs without chorus are indicated

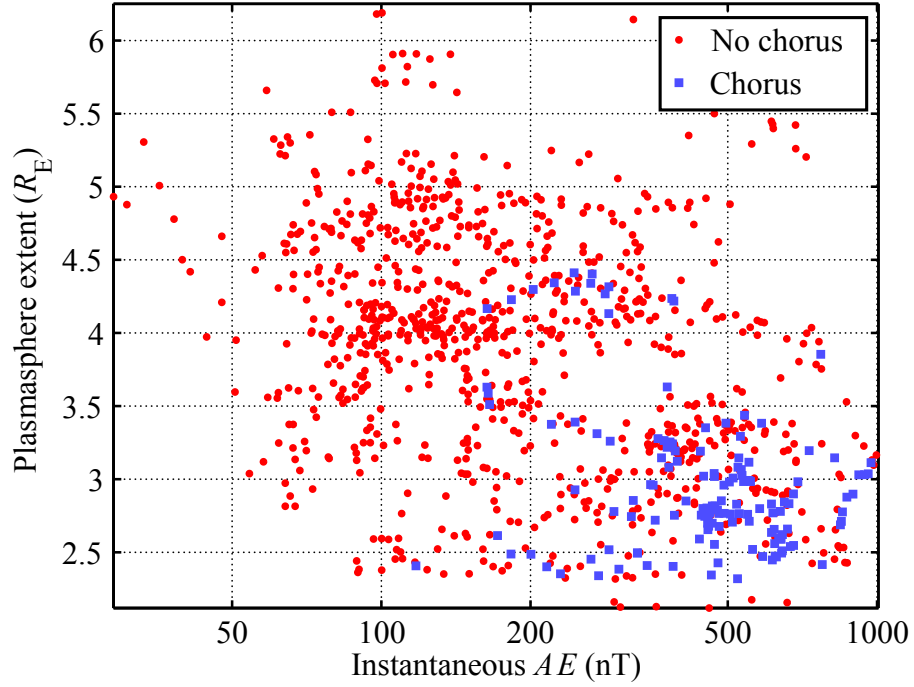


Figure 4.3: Scatter plot of synoptic epochs with (blue squares) and without (red dots) chorus. Note that AE is displayed on a logarithmic scale, while plasmasphere extent is displayed on a linear scale.

with red dots. The scattered points themselves are the same as in the left panel of Figure 4.2, with some data gaps removed. One can get the general impression from this plot that chorus is more likely to be observed at Palmer for low L_{PP} and high AE .

To examine the data more rigorously, regression analysis (Section A.4) is used to construct a generalized linear model. This provides additional insight into properties that are not obvious from a simple scatter plot, such as at which L_{PP} chorus occurrence is maximized, and how strong that peak is. We seek a solution to (A.13), with X

composed of powers of L_{PP} as,

$$Y = X\beta = \begin{bmatrix} 1, & L_{PP}, & L_{PP}^2, & \dots, & L_{PP}^m \end{bmatrix} \begin{bmatrix} \beta_0 \\ \beta_1 \\ \beta_2 \\ \vdots \\ \beta_m \end{bmatrix}. \quad (4.1)$$

The generalized linear model regression procedure from MATLAB is used to obtain a linear fit. Bayesian Information Criterion (BIC) is employed to determine which model parameters to retain. Additionally, the maximum model order is restricted to four.

To determine whether there is any frequency dependence in the degree to which chorus occurrence changes with L_{PP} , the regression analysis is separately performed on three cases: all frequencies, $f < 1.5$ kHz and $f > 3$ kHz. For all frequencies and $f < 1.5$ kHz, the fourth-order model has the lowest BIC and is therefore the favored model. For $f > 3$ kHz, the second-order model has the lowest BIC. The model parameters for the three cases, along with the P -values, are shown in Table 4.1. The P -value in this case represents the probability of erroneously assigning a nonzero value to a given coefficient when its true value is zero. Since all of the P -values are well below 0.05, we can safely assume that all coefficients are significant.

Figure 4.4 shows the modeled normalized occurrence as a function of plasmasphere extent for the three cases of all frequencies (left), $f < 1.5$ kHz (center) and $f > 3$ kHz (right). The probability of chorus occurrence, μ , is indicated by a solid black line, and the 95% confidence intervals of the fit are indicated by the surrounding shaded regions. The model for $f < 1.5$ kHz is quite similar to the one for all frequencies, with the same predictors X and similar coefficients β . The model for $f > 3$ kHz is rather different, with different X . This is a consequence of the fact that 80% of chorus observed at Palmer includes frequency components below 1.5 kHz, but only 33% of chorus includes components above 3 kHz.

A distinct feature of all curves is a “saturation” effect, where chorus occurrence

Table 4.1: Univariate Model Coefficients

X	β	P -value
<i>All frequencies</i>		
1	-389	1.78×10^{-5}
L_{PP}	465	2.33×10^{-5}
L_{PP}^2	-204	3.47×10^{-5}
L_{PP}^3	38.7	5.77×10^{-5}
L_{PP}^4	-2.71	9.86×10^{-5}
<i>$f < 1.5$ kHz</i>		
1	-417	1.36×10^{-5}
L_{PP}	503	1.53×10^{-5}
L_{PP}^2	-223	1.98×10^{-5}
L_{PP}^3	42.8	2.94×10^{-5}
L_{PP}^4	-3.02	4.64×10^{-5}
<i>$f > 3$ kHz</i>		
1	-35.8	2.15×10^{-3}
L_{PP}	25.8	1.76×10^{-3}
L_{PP}^2	-4.81	8.99×10^{-4}

does not increase monotonically with decreasing plasmasphere extent; instead, a peak in occurrence can be seen at $L_{PP}=2.6$ for $f < 1.5$ kHz and at $L_{PP}=2.7$ for $f > 3$ kHz. Additionally, the curve for $f < 1.5$ kHz has a longer tail for higher L_{PP} than that of $f > 3$ kHz, indicating that a less-disturbed (more-extended) plasmasphere permits only lower frequency chorus access to Palmer.

4.3.3 Chorus Occurrence versus Plasmasphere Extent and AE

Although it was shown in the previous section that plasmasphere extent is strongly related to chorus normalized occurrence at Palmer, it is not yet clear whether this is truly a consequence of the instantaneous plasmasphere extent or whether it is simply a consequence of the fact that magnetic substorms both increase the likelihood of chorus and, separately, cause erosion of the plasmapause. To explore this confounding effect, multiple regression is used to separately examine dependence of μ on both

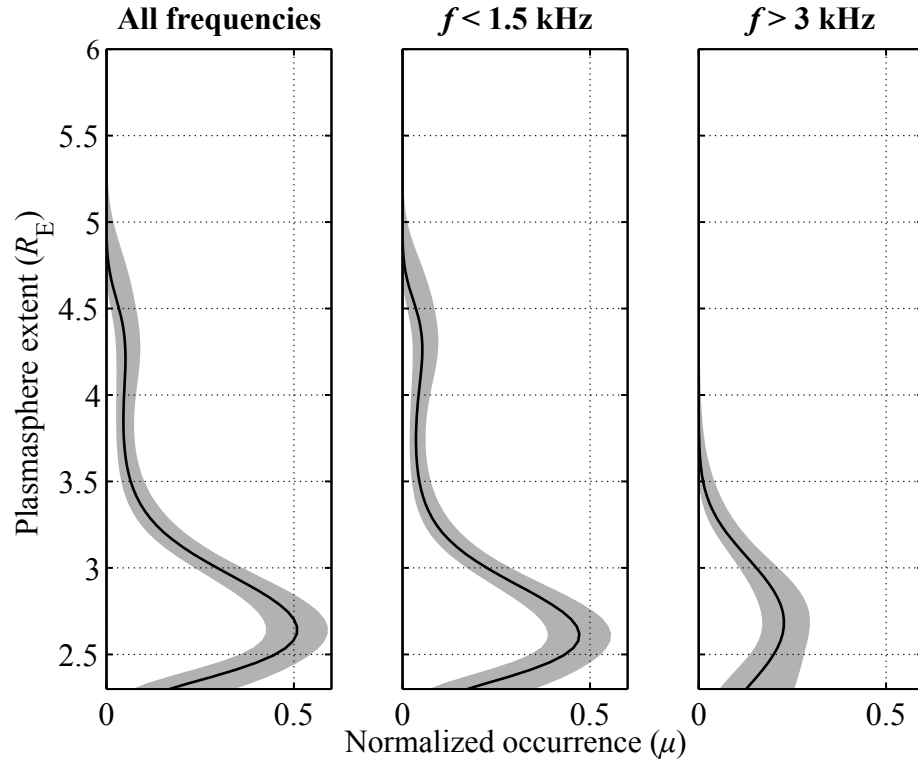


Figure 4.4: Predicted normalized occurrence rate (μ) as a function of plasmasphere extent (L_{PP}) for chorus observations at Palmer for (left) all frequencies, (center) $f < 1.5$ kHz and (right) $f > 3$ kHz. Solid lines indicate modeled values of μ , and shaded regions indicate 95% confidence intervals. The models for all frequencies and $f < 1.5$ kHz include up to fourth-order terms of L_{PP} , while the model for $f > 3$ kHz includes up to second-order terms.

Table 4.2: Bivariate Model Coefficients (All Frequencies)

X	β	P -value
1	1.053×10^3	9.4×10^{-5}
$\log_{10} AE$	-1.850×10^3	1.4×10^{-5}
$\log_{10} AE \cdot L_{PP}$	6.356×10^2	1.9×10^{-6}
$(\log_{10} AE)^2$	7.642×10^2	9.1×10^{-6}
L_{PP}^2	-2.316×10^2	3.4×10^{-6}
$(\log_{10} AE)^2 \cdot L_{PP}$	-2.588×10^2	1.8×10^{-6}
$(\log_{10} AE)^3$	-1.042×10^2	7.5×10^{-6}
L_{PP}^3	4.518×10^1	5.5×10^{-6}
$(\log_{10} AE)^3 \cdot L_{PP}$	3.486×10^1	2.0×10^{-6}
L_{PP}^4	-3.245×10^0	9.9×10^{-6}

plasmasphere extent, which may affect chorus propagation, and AE , which is related to chorus generation.

Again, a solution to (A.13) is sought, except that now X includes L_{PP} and $\log_{10} AE$ terms as well as interaction terms. Beginning with a model that includes all permutations of L_{PP} through L_{PP}^4 and $\log_{10} AE$ through $(\log_{10} AE)^4$ of total order four or less, terms with high P -values whose removal increases BIC are dropped. Eventually, the model of Table 4.2 is found. Table 4.2 shows the selected model parameters, their coefficients, and the P -value of each coefficient.

A plot of μ , the modeled parameter of (A.12), as a function of L_{PP} and $\log_{10} AE$ for all frequencies, is shown in Figure 4.5a. To reduce noise in panel (a), the actual plotted quantity is $\mu \cdot (1 - \sigma_{95}^2)$ instead of μ , where σ_{95} is the range of the 95% confidence interval, obtained by subtracting panel (c) from panel (b). Plotting this related parameter has the effect of setting areas with high variance to zero, e.g., the lower-left and upper-right portions of the plot. As in Section 4.3.2, a saturation effect is seen with respect to L_{PP} , and a peak in μ is seen at $L_{PP} = 2.6$ for $AE \gtrsim 100$ nT. Additionally, the long tail in L_{PP} is reproduced, with μ retaining a small but nonzero value up to $L_{PP} \sim 4.5$.

The primary takeaway fact from Figure 4.5 is that features with respect to L_{PP} persist for a wide range of AE , and features with respect to AE persist for a wide

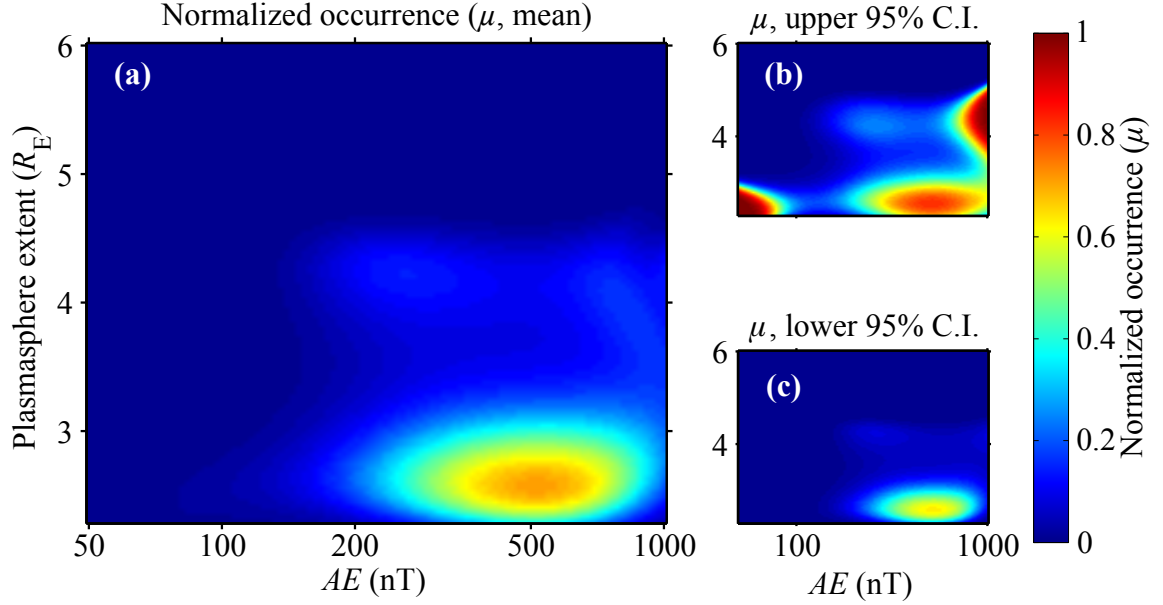


Figure 4.5: Model for μ , the normalized occurrence rate of chorus as a function of plasmasphere extent and AE , obtained using generalized linear model regression on observations of chorus. Panel (a) shows the expected value of normalized occurrence, and panels (b) and (c) show the upper and lower bounds of the 95% confidence interval for μ .

range of L_{PP} . E.g., the peak at $L_{PP} = 2.6$ exists for $200 \text{ nT} \lesssim AE \lesssim 1000 \text{ nT}$, and the peak at $AE = 500 \text{ nT}$ exists for $2.1 \lesssim L_{PP} \lesssim 3.1$. This is an indication that effects of AE or L_{PP} near the peak of chorus occurrence are quasi-independent of each other. Had it been otherwise, and the effects of AE and L_{PP} were strongly dependent, the peak in Figure 4.5 would appear as a diagonal line. Therefore, it is clear that the plasmopause *is* in fact significantly changing the characteristics of chorus propagation to Palmer, and that the correlation between L_{PP} and μ is not merely a confounding effect of the fact that magnetic substorms tend to affect both chorus generation and the plasmopause.

4.4 Modeling of Chorus Propagation

The effects of plasmasphere extent on chorus propagation are further investigated using a combination of raytracing and full wave modeling. First, reverse raytracing is used wherein rays begin above the ionosphere over Palmer with wavenormal angles within the ionospheric transmission cone. The rays are then propagated backwards to their magnetospheric source. A valid source location for each ray is outside the plasmasphere at the magnetic equatorial plane [LeDocq *et al.*, 1998; Santolík *et al.*, 2005] at a radial distance such that the wave frequency is in the range $0.1f_{ceq} \leq f \leq 0.5f_{ceq}$ [Tsurutani and Smith, 1974; Burtis and Helliwell, 1976]. Rays that are able to enter a valid source location are binned by radial extent and wavenormal angle. This binning creates a comprehensive picture of the portion of the equatorial source region from which generated rays may reach Palmer. Ray attenuation is calculated via Landau damping on the magnetospheric ray paths using an empirical model of energetic particle fluxes. In addition, we assume that waves may penetrate the ionosphere some distance from Palmer and propagate within the Earth-ionosphere waveguide before being received; a full wave model is used to estimate this additional waveguide attenuation. Full details of the simulation are further discussed below.

The simulation is performed for a range of plasmasphere extents. For each plasmasphere extent, a single scalar quantity is calculated, which we term the Chorus Availability Factor (CHAF). CHAF is a cumulative measure of the portion of the chorus source region, integrated over all radial extents and wavenormals, and weighted by relative attenuation and source probability, that is observable at Palmer. Although CHAF is not a probability, if the plasmasphere extent does significantly influence chorus propagation, the trends of CHAF versus L_{PP} are expected to resemble those of the experimentally modeled chorus normalized occurrence, μ , from Section 4.3.2.

4.4.1 The Stanford VLF 3D Raytracer

The new version of the Stanford VLF raytracer was developed by Forrest Foust in 2010 as a more accurate and complete model to replace Stanford’s previous raytracing program [Inan and Bell, 1977], which we refer to as the Stanford VLF legacy

raytracer. The new raytracer, which we refer to as the Stanford VLF 3D raytracer, was written from the ground up, and is not an extension or revision of the Stanford VLF legacy raytracer. A description of the raytracer follows.

Hamilton's equations for the propagation of a ray through a medium with spatially-varying dispersion relation defined by the implicit function $F(\omega, \mathbf{k}, \mathbf{r}) = 0$ can be stated as:

$$\frac{d\mathbf{r}}{dt} = -\frac{\nabla_{\mathbf{k}} F}{\partial F / \partial \omega} \quad (4.2)$$

$$\frac{d\mathbf{k}}{dt} = \frac{\nabla_{\mathbf{r}} F}{\partial F / \partial \omega} \quad (4.3)$$

With the constraint:

$$F(\omega, \mathbf{k}, \mathbf{r}) = 0 \quad (4.4)$$

For generality, and for the purpose of accommodating any arbitrary function for the plasma density or background magnetic field, the spatial and k -space derivatives are evaluated numerically using finite differences, that is:

$$\frac{\partial F}{\partial k_i} \approx \frac{1}{2\Delta k} (F(\omega, \mathbf{k} + \Delta k \mathbf{e}_i, \mathbf{r}) - F(\omega, \mathbf{k} - \Delta k \mathbf{e}_i, \mathbf{r})) \quad (4.5)$$

$$\frac{\partial F}{\partial r_i} \approx \frac{1}{2\Delta r} (F(\omega, \mathbf{k}, \mathbf{r} + \Delta r \mathbf{e}_i) - F(\omega, \mathbf{k}, \mathbf{r} - \Delta r \mathbf{e}_i)), \quad (4.6)$$

where $i = \{1, 2, 3\}$, and \mathbf{e}_i are the unit vectors. Since the derivatives are evaluated numerically, all that is required to adapt a new plasma density model is a function that evaluates $F(\omega, \mathbf{k}, \mathbf{r})$.

After approximating the spatial and k -space derivatives, six ordinary differential equations remain, which are integrated numerically in time using a standard adaptive Runge-Kutta method. In contrast to the approach of [Haselgrove \[1955\]](#), a moving B_0 -aligned coordinate system is not used; instead, the system of equations is directly solved in global Cartesian coordinates. After one time step, the constraint $F = 0$ is not in general met, and an intermediate solution exists with an error $F(\omega, \mathbf{k}^*, \mathbf{r}^*) = \epsilon$. This is handled using a standard method for solving constrained ODEs, by finding a

“nearby” point (\mathbf{k}, \mathbf{r}) that satisfies $F(\omega, \mathbf{k}, \mathbf{r}) = 0$ after every time step. The specific approach used is to simply re-solve the dispersion relation assuming the wavenormal angle is kept constant. If this fails (due to being too close to the resonance cone), the time step is halved and the procedure is attempted again.

The Stanford VLF 3D raytracer can accommodate any arbitrary function for the cold background plasma number density. In this study, the Global Core Plasma Model (GCPM) [*Gallagher et al.*, 2000] is implemented, sampled on a regular grid and interpolated by a fast, local, C^1 (continuous in the first derivative) tricubic interpolation scheme described in *Lekien and Marsden* [2005]. The plasmasphere modeled by the GCPM is field-aligned to the dipole field, and remains so from the equatorial region down to altitudes between 7800 km ($K_p \sim 3^+$) to 2600 km ($K_p \sim 8^-$). The typical plasmopause represented by the GCPM exhibits a density drop of between 1 ($K_p \sim 3^+$) and 1.5 ($K_p \sim 8^-$) orders of magnitude in the equatorial plane over a range of about $0.3 R_E$. The choice of background magnetic field is also arbitrary; in this study, the Tsyganenko-96 (T96) model [*Tsyganenko*, 1995; *Tsyganenko and Stern*, 1996] is used.

Thermal losses are included as in *Kennel* [1966]. Equation (3.9) in *Kennel* [1966], corrected for a typographical error [*Chen et al.*, 2009, paragraph 9], is solved for the Landau ($m=0$) resonance. This yields the temporal damping rate ω_i , which is then related to the spatial damping rate k_i by the relation in *Brinca* [1972]:

$$\omega_i = \vec{k}_i \cdot \vec{v}_g. \quad (4.7)$$

The method in *Kennel* [1966] requires the evaluation of the gradients of the hot particle distribution function in $(v_{\parallel}, v_{\perp})$ space, as well as the evaluation of a 1D integral over v_{\perp} over the interval $[0, \infty)$. In order to accommodate any arbitrary distribution function, the derivatives are again evaluated numerically using finite differences. The velocity is first normalized by the speed of light for numerical reasons, then mapped into a finite range $t = (0, 1)$ using the mapping $v_{\perp} = (1 - t)/t$:

$$\int_0^{\infty} f(v_{\perp}) dv_{\perp} = \int_0^1 \frac{1}{t^2} f\left(\frac{1-t}{t}\right) dt. \quad (4.8)$$

Finally, the integral is evaluated numerically using adaptive quadrature. The method used is general and can accommodate any number of resonances. In this study, only the Landau ($m=0$) resonance is used, since it is the dominant source of loss.

The choice of hot particle distribution is crucial to the accurate calculation of Landau damping. Within the plasmasphere, the phase space density expression of *Bell et al.* [2002], based on measurements with the POLAR spacecraft sampled in the range $2.3 < L < 4$, is used. Outside the plasmasphere, the methodology of *Bortnik et al.* [2007a], derived from measurements with the CRRES spacecraft outside the plasmasphere up to $L \sim 7$, is used.

A hybrid model smooths the two models at the plasmasphere boundary, and is implemented as follows. Let f_0^{POL} represent the phase space density (PSD) of *Bell et al.* [2002] from POLAR in units of, e.g., s^3/cm^6 , and let f_0^{CRR} represent the PSD of *Bortnik et al.* [2007a] from CRRES in the same units. Define the “weights” of the two distributions at a given L shell, L_{meas} , for a given plasmasphere extent, L_{PP} , as

$$\begin{aligned} w^{\text{POL}} &= \frac{\exp(-\alpha(L_{\text{meas}} - L_{\text{PP}}))}{1 + \exp(-\alpha(L_{\text{meas}} - L_{\text{PP}}))} \\ w^{\text{CRR}} &= \frac{\exp(\alpha(L_{\text{meas}} - L_{\text{PP}}))}{1 + \exp(\alpha(L_{\text{meas}} - L_{\text{PP}}))}. \end{aligned} \quad (4.9)$$

Then, the implemented hybrid PSD is given by the weighted mean in log-space of POLAR and CRRES PSDs as

$$f_0^{\text{hybrid}} = \exp \left(\frac{\log(f_0^{\text{POL}})w^{\text{POL}} + \log(f_0^{\text{CRR}})w^{\text{CRR}}}{w^{\text{POL}} + w^{\text{CRR}}} \right). \quad (4.10)$$

Reasonable results are obtained with $\alpha=5$. For reference, when $L_{\text{meas}} - L_{\text{PP}} = 0$, the two distributions are weighted equally in log-space, and when $L_{\text{meas}} - L_{\text{PP}} = +(-)0.5$, i.e., the measurement location is 0.5 L shells beyond (within) the plasmapause, f_0^{CRR} is weighted 12 times more (less) than f_0^{POL} in log-space.

It should be noted that, although this raytracing procedure is three-dimensional, the following study is restricted to rays that lie approximately in a single meridional plane. Due to azimuthal gradients in the plasma and B-field models, rays exhibit

a slight tendency to propagate to earlier local times with increasing L shell. The maximum azimuthal deviation of any ray considered in this study is 18° (1.2 hours in MLT), with an average maximal deviation per ray of 7° (0.5 hours in MLT). Because this value is small, the local time deviation of rays is neglected in this study, and wavenormals and positions are given in two dimensions with respect to the meridional plane of the rays.

4.4.2 Raytracing Procedure

Rays are launched in the vicinity of Palmer, at $\lambda = 50^\circ\text{S}$, MLT = 06, UTC = 10. The GCPM and Tsyganenko models for plasma density and magnetic field are used, and the rays propagate in the non-ducted mode. Rays are launched at 1000 km altitude, with 80 equally-spaced magnetic latitudes within 1000 km of 50°S , and with 13 equally-spaced k -vector angles directed away from the Earth within the transmission cone, for a total of 1040 rays per simulation.

The transmission cone angle defines the maximum deviation of downward-directed k -vectors, with respect to the normal to the Earth's surface, that may penetrate through the ionosphere and to the ground without suffering total internal reflection at the boundary between the lower edge of the ionosphere and free space [e.g., [Helliwell, 1965](#), Sec. 3.7]. To calculate the transmission cone, it is assumed that the plasma density from the ray origin to the ground may be approximated as a stratified medium, and therefore that the horizontal component of the k -vector is conserved. At 1 kHz and 4 kHz, two frequencies of interest for this study, the half angle of the transmission cone, measured from the vertical, is 0.84° and 1.44° , respectively.

Each ray is traced for up to 30 seconds, or until it either impacts the Earth, or departs from the precalculated density grid in the range $-4 \leq X_{\text{SM}} \leq 4$, $-8 \leq Y_{\text{SM}} \leq 0$, $-3 \leq Z_{\text{SM}} \leq 3$, where all coordinates are in units of Earth radii in the solar-magnetic coordinate system. In practice, under these criteria, no rays survive beyond 10 seconds. Each time a ray crosses the equatorial plane, the local plasma density and gyrofrequency are examined. If the ray is (1) outside the plasmasphere, and (2)

within the range $0.1f_{ceq} \leq f \leq 0.5f_{ceq}$ (where f_{ceq} is the equatorial electron gyrofrequency along the given field line), which is the frequency range of lower-band chorus [Tsurutani and Smith, 1974; Burtis and Helliwell, 1976], then that point is saved as a potential chorus source location. A single original ray may give rise to more than one potential chorus source location if it exhibits multiple magnetospheric reflections.

The chorus source region (i.e., the region from which chorus is truly generated, which is not the same as the location from which the “reverse” rays are launched) is considered to lie on the equatorial plane, with initial wavenormal angles uniformly distributed within the resonance cone. Although several satellite studies have attempted to characterize the wavenormal distribution of the equatorial chorus source [e.g., Haque et al., 2010, and references therein], statistics have generally been too low to draw any definitive conclusions, leading to our use of a uniform distribution in this study. The source region is binned on two parameters: R , the distance from the center of the Earth in the equatorial plane, and ψ , the initial wavenormal angle with respect to the ambient magnetic field. Each bin is of uniform size, with $\Delta R = 0.05R_E$ and $\Delta\psi = 4^\circ$.

Chorus rays that can reach Palmer tend to occur in several distinct “families,” or groupings of rays with similar initial wavenormals and radial extent. Figure 4.6 shows several facets of the raytracing procedure, along with example rays from the two ray families that are present at 1 kHz. For this simulation, $L_{PP} = 2.9$. The raytracing procedure is described below with reference to Figure 4.6.

Panel (a) shows representative rays from the two ray families. We interpret the rays in their “forward” sense, as if they were originally launched from the equatorial plane and eventually arrived at 1000 km altitude. Ray paths are shown in white, with wavenormals shown as red ticks, equally spaced every 100 ms. The magenta line indicates a contour of $f/f_{ceq} = 0.1$; all chorus generation happens at values of R beyond this boundary. The upper bound on f_{ceq} for chorus generation, at $f/f_{ceq} = 0.5$ is beyond the scale of the image, at $R \sim 7 R_E$. Palmer’s location is indicated by the green triangle at $\lambda = -50^\circ$ on the surface of the Earth. The background image is a meridional slice of the GCPM electron density. Ray family 1 consists of rays that propagate directly from the chorus source region to Palmer without magnetospherically reflecting

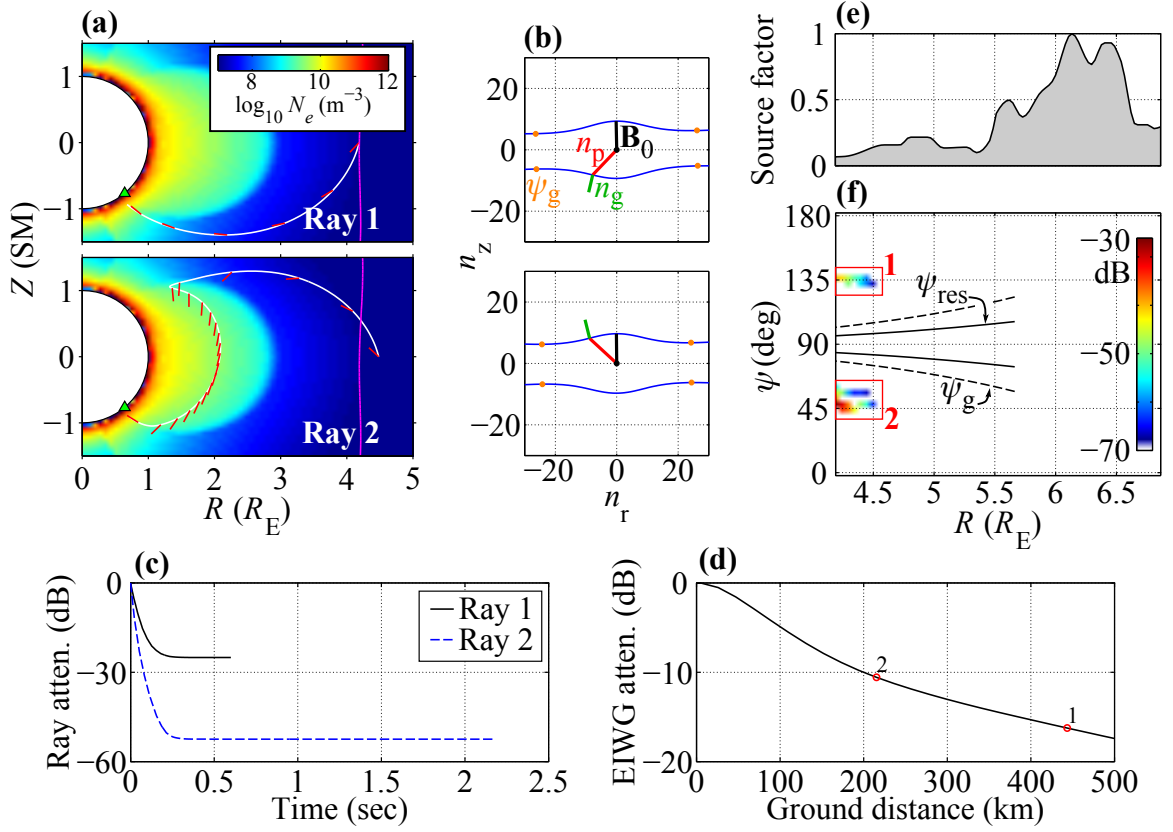


Figure 4.6: Two 1 kHz ray families that are capable of being received at Palmer. (a) Representative ray paths from each of two ray families. Family 1 is the direct path from the source region to Palmer, and family 2 includes rays that magnetospherically reflect into the plasmasphere before their reception on the ground. (b) Initial refractive index surfaces for example rays. (c) Attenuation of example rays versus time over the course of raytracing, via Landau damping. (d) Attenuation of example rays versus distance within the Earth-ionosphere waveguide, via full wave modeling. (e) Source factor showing relative expected chorus probability versus radial extent. (f) Source attenuation plot of relative received power versus wavenormal ψ and radial extent. Solid lines indicate the local resonance cone angle, ψ_{res} , and dashed lines indicate the local Gendrin angle, ψ_g . The two families of similar rays, labeled 1 and 2, correspond to the two example rays from the previous panels.

(MRing), and family 2 consists of rays that MR at the plasmapause boundary, which allows them access into the plasmapause before reaching Palmer. Because raytracing is performed in three dimensions, the ray paths and wavenormals have been projected into the MLT=06 meridional plane.

Panel (b) shows the initial refractive index surfaces for the representative rays. The direction of the ambient magnetic field, B_0 , the wave refractive index, $n_p = c/v_p$, and the group refractive index, $n_g = c/v_g$, as well as the Gendrin angle, ψ_g , are indicated, where c is the speed of light in free space, v_p is the wave phase velocity and v_g is the wave group velocity. n_p and n_g point in the direction of the wave k -vector and group velocity vector, respectively.

Each potential chorus source location represents a ray that originally begins with unity power and is attenuated in two separate steps. First, panel (c) shows the attenuation of the representative rays over the course of their magnetospheric propagation due to Landau damping, as discussed in Section 4.4.1. The majority of damping occurs at high L shells outside the plasmasphere. In particular, once ray 2 enters the plasmasphere, the attenuation due to Landau damping is negligible. Unlike some other studies of raytracing [e.g., [Bortnik et al., 2007a,b](#)], this study does not include a geometric effect in determining the power gain or loss due to the focusing of magnetic field lines at low altitudes. Instead, this focusing or defocusing happens naturally through the use of a large number of rays.

The second mode of attenuation, shown in panel (d), is attenuation from Earth-ionosphere waveguide propagation. Each ray begins at 1000-km altitude with the injection point footprint a distance d from Palmer Station, where $d \leq 1000$ km. Earth-ionosphere waveguide attenuation is calculated using the full wave model of [Lehtinen and Inan \[2008, 2009\]](#). A summer night-time ionospheric profile and a perfectly conducting ground layer (representative of Palmer’s primarily all-sea paths) are used. A Gaussian wave packet of the appropriate frequency is injected at 140 km altitude with vertical (downward) wavenormal. The ground power at various distances from the source is recorded, normalized by the ground power directly beneath the source. The resulting quantity $A(d)$ represents an attenuation factor for Earth-ionosphere waveguide propagation, as a function of d , by which each ray’s power is multiplied.

The full wave model is run only once for any given frequency, and the quantity $A(d)$ is assumed to be valid for all modeled rays within 1000 km of Palmer. The two example rays reach the ground at ~ 450 km and ~ 215 km from Palmer, respectively, and are marked as such in panel (d). When both Landau damping and Earth-ionosphere waveguide attenuation are considered, there can be wide variations in the attenuation of different rays in a given family, due to the fact that slight variations in initial conditions may give rise to large variations in propagation paths and ionospheric penetration points.

Panel (e) is a plot of “source factor” as a function of radial extent, R . This plot is derived from [Burtis and Helliwell \[1976, Fig. 9c\]](#), which shows chorus occurrence as a function of f/f_{ceq} . We define source factor as the observed occurrence of [Burtis and Helliwell \[1976, Fig. 9c\]](#), normalized so that the maximum value is 1. Here, source factor is plotted against R , using the T96 magnetic field model to map from f/f_{ceq} to R . The source factor plot is then the relative expected likelihood of observing a 1 kHz chorus source at a given radial extent in the equatorial plane. Because the measurements of [Burtis and Helliwell \[1976\]](#) include both waves inside and outside the plasmasphere, it is possible that the observed chorus percentage is artificially low at low f/f_{ceq} or R due to those measurements being taken within the plasmasphere where chorus is generally not observed. The use of the source factor in deriving the Chorus Availability Factor (CHAF) is discussed in Section 4.4.3, and due to the possible confounding effects of its constituent data containing measurements inside the plasmasphere, CHAF is derived both with and without implementing the source factor.

After building a list of potential chorus source locations from the 1040 original rays, the amplitude of any given R - ψ bin is set to the maximum ray amplitude in that bin after attenuation both via Landau damping in the magnetosphere and via attenuation in the Earth-ionosphere waveguide. We refer to a plot of the binned results for a simulation with a given wave frequency and plasmasphere extent as a “source attenuation plot.”

Panel (f) shows a source attenuation plot for a simulation where $L_{PP}=2.9$, from which the two example rays are drawn. The local resonance cone angle, ψ_{res} , defined

as the wavenormal angle at which the magnitude of the refractive index goes to infinity, is indicated by the solid black lines. The local Gendrin angle, ψ_g , defined as the nonzero wavenormal angle at which the group velocity vector is parallel to the static magnetic field, is indicated by the dashed black lines. The two separate ray families, from which the above example rays are drawn, are highlighted with red boxes. The rays do not show any particular relationship with the resonance cone or Gendrin angles.

Figure 4.7 is analogous to Figure 4.6, but for 4 kHz waves. Because f is increased, the magenta lines, indicating the contours of $f/f_{ceq}=0.1$ and $f/f_{ceq}=0.5$ are now closer to the Earth, and both boundaries of the chorus source region can be seen. In addition, there are now four ray families, representing the direct path, and one, two and three magnetospheric reflections. In all cases, the damping is most significant at large L shells outside the plasmasphere, where wavenormals are most oblique. Rays 3 and 4 begin with their wavenormals directed away from the Earth, near the resonance cone. After the first magnetospheric reflection, they appear to be guided by the plasmopause boundary before reflecting from the inner boundary. This has the effect of rotating the wavenormal towards the Earth, allowing the rays to reach the ground. Because Rays 3 and 4 spend more time outside the plasmasphere, and have more highly oblique wavenormals than do rays 1 and 2, they are damped more heavily during their propagation.

In the 4 kHz case, the initial wavenormals of some ray families do show a relationship with the resonance cone and Gendrin angles. Some rays from families 1 and 2 tend to be generated near the Gendrin angle, while some rays from families 3 and 4 tend to be generated near the resonance cone angle. The associations are loose, and no ray families appear constrained to either the resonance cone or the Gendrin angle. The relation between the wavenormals of ray family 1 (the direct path) and the Gendrin angle is consistent with the work of *Chum and Santolik* [2005], who found that certain rays generated with wavenormals in the vicinity of the Gendrin angle would reach low altitudes and possibly penetrate to the ground before being magnetospherically reflected. Although this behavior is seen in our results at 4 kHz, it is not observed at 1 kHz. This is possibly due to the fact that *Chum and Santolik*

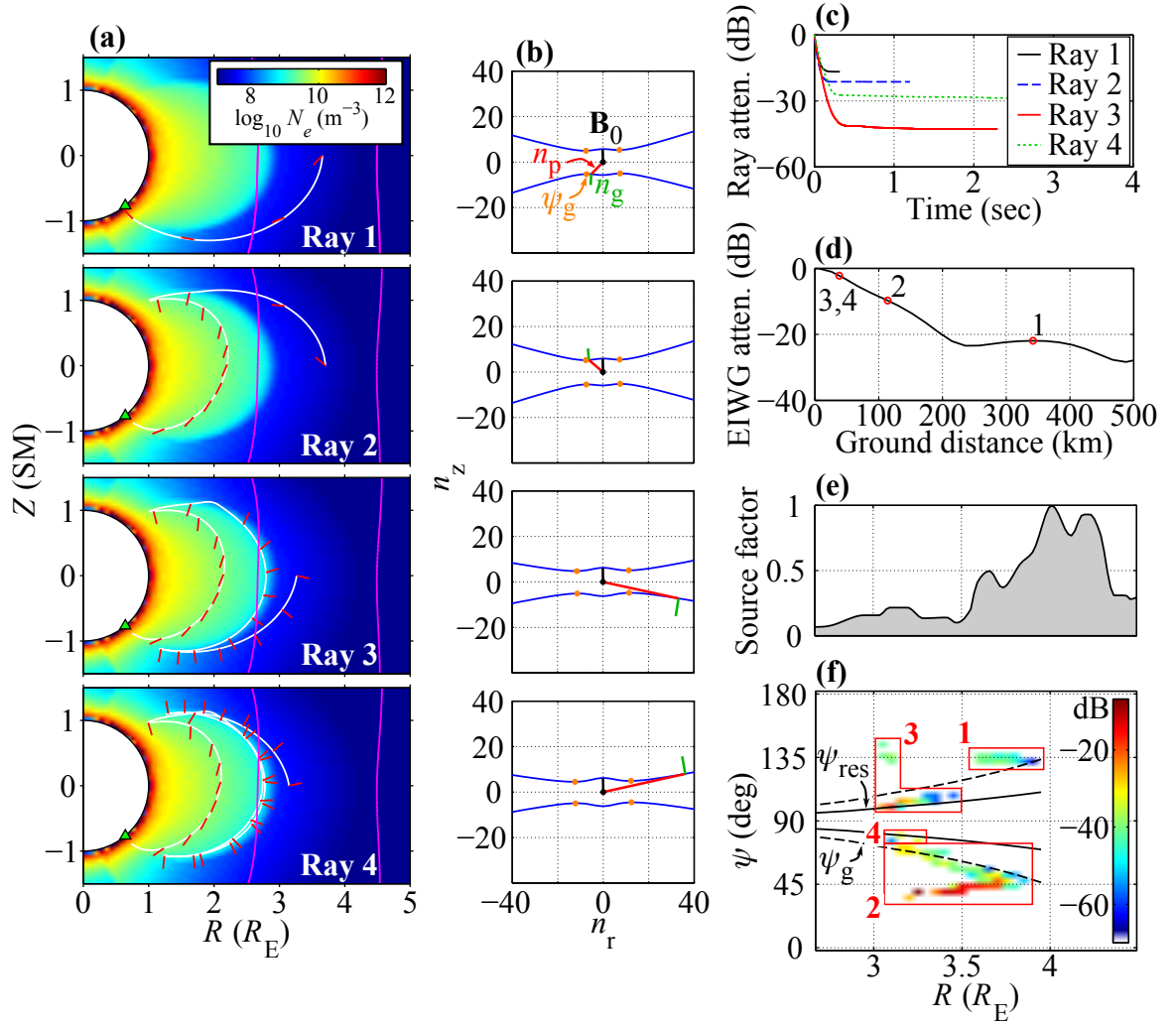


Figure 4.7: Same as Figure 4.6, but for 4 kHz. At this frequency, there are four distinct ray families, representing the direct path, and one, two and three magnetic reflections.

[2005] did not include Landau damping in their calculations. Although some 1 kHz rays in our study do begin at the equatorial plane with wavenormals near the Gendrin angle, those waves are damped to negligible power in the simulation, and therefore do not appear on the source attenuation plot in Figure 4.6f.

4.4.3 Chorus Availability Factor

Figures 4.6f and 4.7f showed source attenuation plots at 1 kHz and 4 kHz for a single plasmasphere extent, $L_{PP}=2.9$. This analysis is repeated for many different values of L_{PP} to gain insight into the particular way in which the plasmasphere extent affects the ability for chorus waves to propagate from their source to Palmer. Figure 4.8 shows source attenuation plots for 1 kHz (upper panels) and 4 kHz (lower panels) for plasmasphere extents in the range $2.1 \leq L_{PP} \leq 4.3$. The color scale has been changed slightly for clarity.

Initially, we focus our discussion on the 1 kHz case, in the upper panels of Figures 4.8. At the greatest plasmasphere extent, $L_{PP}=4.3$, rays from the chorus source region are not accessible to Palmer; reverse rays launched from Palmer are either unable to escape the plasmasphere, and instead reflect off of its inner boundary before impacting the ionosphere in the conjugate hemisphere, or they escape the plasmasphere with oblique wavenormals and are heavily damped before crossing the equatorial plane. As the plasmasphere becomes more eroded down to $L_{PP}=2.9$, although rays as far out as $L=7$ are accessible to Palmer (not shown), most are severely damped; only certain rays that originate within $4.2 \lesssim L \lesssim 4.6$ sufficiently avoid damping to be received above the -70 dB cutoff. Erosion of the plasmasphere beyond $L_{PP}=2.9$ results in increased propagation time outside the plasmasphere, and hence, increased damping, particularly for waves with initial wavenormals $\psi \sim 50^\circ$. The situation is similar for 4 kHz. For high L_{PP} , rays from the chorus source region cannot reach Palmer; reverse rays are unable to escape the plasmasphere. For $L_{PP} \sim 2.9$, a maximum of rays reach Palmer with significant power. For low L_{PP} , as for high L_{PP} most reverse rays launched from Palmer do not escape the plasmasphere; only rays which propagate along the direct path, entirely outside of the plasmasphere, are still able

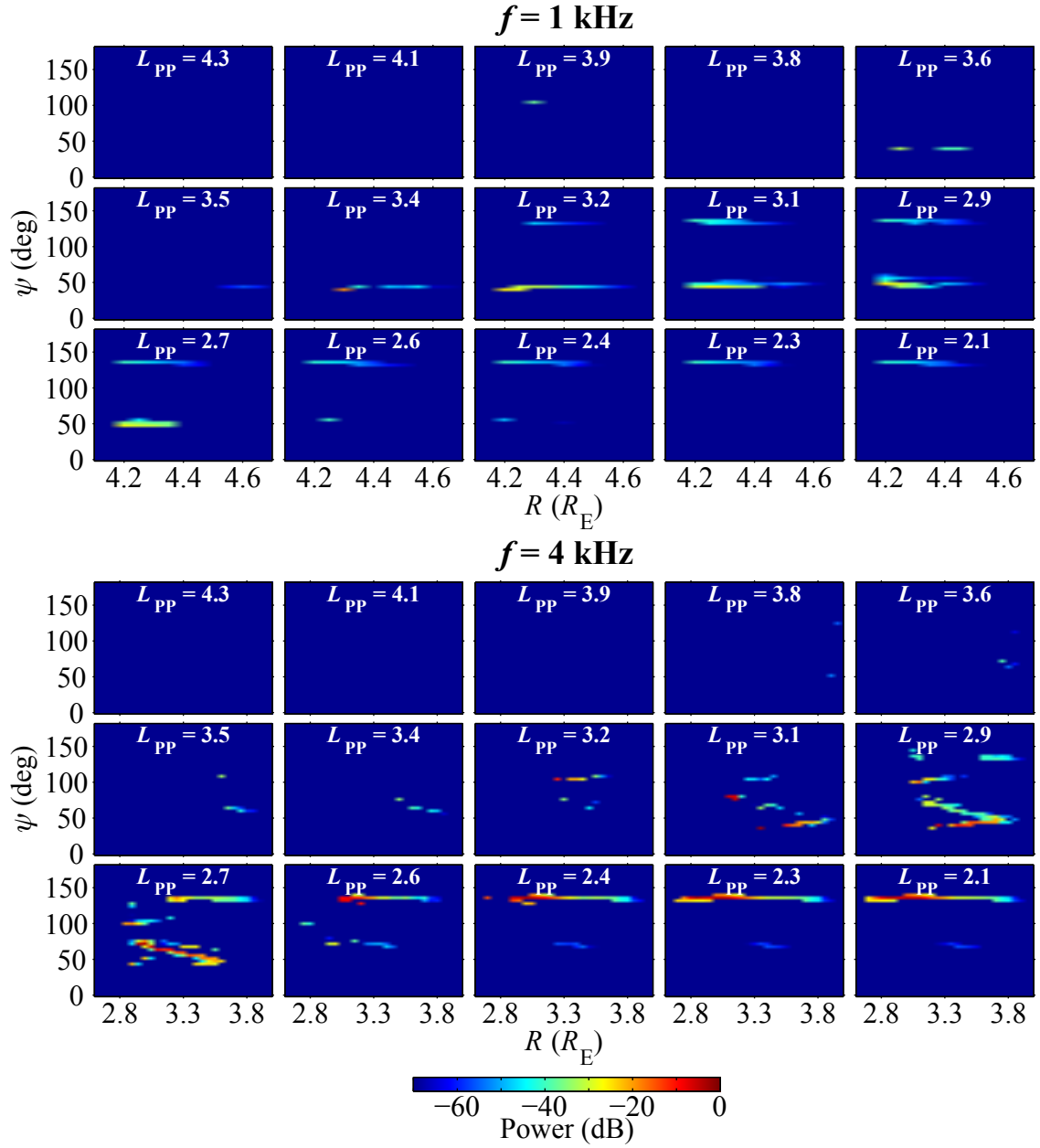


Figure 4.8: Source attenuation plots for $f = 1$ kHz (upper panels) and $f = 4$ kHz (lower panels) for plasmasphere extents in the range $2.1 \leq L_{PP} \leq 4.3$. Note that the scales of the x -axes in the upper and lower panels are not the same.

to reach Palmer without significant damping.

One important difference between the simulations at 1 kHz and 4 kHz is where the plasmopause lies with respect to the extents of the chorus source region, defined by $0.1 \leq f/f_{ceq} \leq 0.5$. At 1 kHz, the source region is in the range $4.2 \leq L \leq 6.9$, which is beyond the plasmopause for almost all simulations. However, at 4 kHz, the source region is in the range $2.7 \leq L \leq 4.5$, which means that for many of the simulations, the plasmasphere overlaps the chorus source region. This is why, in the lower panels of Figure 4.8, the chorus source region appears to expand to the left as L_{PP} decreases. The plasmopause is moving to the left of the plots, and a greater portion of the chorus source region is becoming available.

Because rays may be substantially damped over the course of propagation, in order to properly analyze the results of the simulations, it is necessary to define a “minimum detectable ray power,” below which rays are excluded from the analysis. To first order, this can be achieved by comparing the mean power observed on the ground with the mean power observed via in situ measurements. A histogram of observed amplitudes over the course of this study, overlaid with the associated probability distribution, is shown in Figure 4.9. Chorus amplitudes observed at Palmer are distributed approximately log-normally, as

$$A_{dB} \sim \ln \mathcal{N}(\mu = 3.5, \sigma^2 = 0.036) \quad (4.11)$$

with mean 35 dB-fT and standard deviation 6.8 dB-fT. The observed mean of 35 dB-fT at Palmer can be compared with the mean B-field amplitude calculated by [Santolík \[2008\]](#), based on equatorial chorus E-field measurements from [Meredith et al. \[2001\]](#), of 10–100 pT, or 80–100 dB-fT. Comparing the two numbers, up to ~ 65 dB of attenuation is expected from the equatorial source region to Palmer. However, in this analysis, we are not modeling attenuation suffered through trans-ionospheric propagation. Trans-ionospheric attenuation is expected to be on the order of ~ 5 dB, somewhere between the daytime and nighttime attenuation calculations of [Helliwell \[1965, Fig. 3-35\]](#) for 2 kHz waves (since our simulations are run at 06 MLT). This

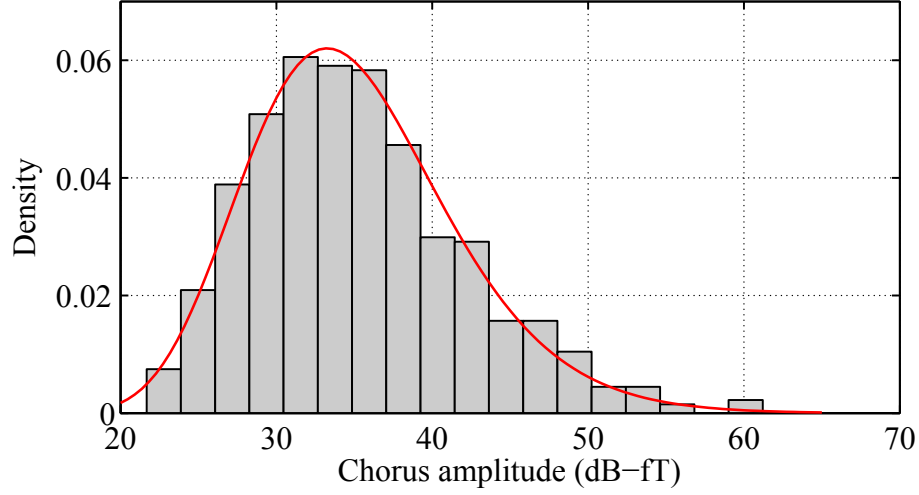


Figure 4.9: Histogram and log-normal probability distribution function (PDF) of observed chorus amplitudes at Palmer. Bins of the histogram have been normalized by the total number of samples and the bin width, so that they have the same units as the log-normal PDF.

leaves an expected attenuation from Landau damping and Earth-ionosphere waveguide losses of ~ 60 dB. To account for the lower end of our observed power distribution, which reaches down to ~ 25 dB-fT in Figure 4.9, an additional 10 dB of loss is allowed. Thus, we define our minimum detectable ray power to be -70 dB. Although it is necessary to define a minimum detectable ray power to perform the following analysis, our conclusions are not strongly dependent on its exact value.

We define the CHAF for a given frequency and L_{PP} as follows. First, all bins of a given simulation (i.e., from a source attenuation plot, such as Figure 4.6f) are normalized by adding 70 dB to each bin, which ensures that bin values are all positive, between 0 and 70 dB. Then, each bin is multiplied by the source factor (e.g., Figure 4.6e), at its particular radial extent. E.g., the bins at the lowest radial extent in Figure 4.6f, at $R \sim 4.2 R_E$, are multiplied by the source factor of Figure 4.6e at that same radial extent, which is approximately 0.05. This has the effect of reducing the influence of bins that are at radial extents at which chorus is less-commonly observed. Finally, the values of the bins are summed, and the resulting scalar quantity, as a function of frequency and L_{PP} , is the CHAF.

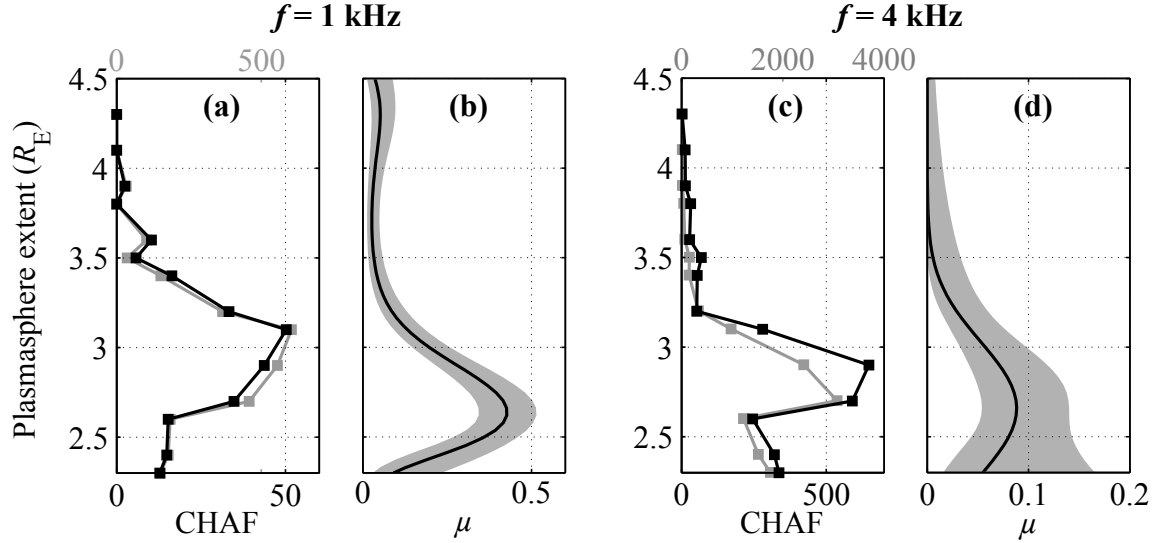


Figure 4.10: Comparison of CHAF from raytracing (a,c) with generalized linear model of occurrence probability, μ , derived from measurements (b,d). CHAF is calculated from constituent data of the source attenuation plots of Figure 4.8. μ is calculated using data at single frequencies 1 kHz and 4 kHz, instead of a range of frequencies as in Section 4.3.2. As before, on the plot of μ , the solid black line indicates μ , and the shaded area indicates the 95% confidence interval. The lighter-colored line on the plots of CHAF represent the values prior to applying the source factor from [Burtis and Helliwell \[1976\]](#), and the darker lines represent values after applying the source factor. The shapes of the curves with and without the source factor applied are very similar. Note that the scales of the x -axes in the upper and lower panels, and on the overlaid plots of CHAF, are not the same.

The CHAF of the 1 kHz and 4 kHz simulations is shown in Figure 4.10a,c. The calculated CHAF both before and after applying the source factor are shown in gray and black lines, respectively. It can be seen that application of the source factor makes only a minor difference in the trend of CHAF with L_{PP} for either frequency. This shows that, even if the fact that chorus is preferentially generated at certain values of f/f_{ceq} is not included (for example, due to the fact that the source factor may artificially reduce the effect of chorus originating at low L shells outside the plasmapause) the plasmapause has a similar effect in dictating the amplitude of received chorus.

Because CHAF is derived from the data that makes up the source attenuation plots

in Figure 4.8, its behavior with respect to L_{PP} is analogous to that in Figure 4.8. As L_{PP} decreases from $L_{PP}=4.3$ to $L_{PP}=2.1$, the availability of different portions of the chorus source region wax and wane, which translates into increasing and decreasing CHAF. At 1 kHz, CHAF is maximized for $L_{PP}=3.1$, where two regions, narrow in ψ and broad in R are accessible to Palmer. At 4 kHz, CHAF is maximized for $L_{PP}=2.9$, where several broad regions of the source region are accessible to Palmer. These regions are made up of rays from the different ray families discussed in Section 4.4.2. We also note that the prodigious paradigm of parallel plasmaspheric Poynting parcels provides the penultimate parable of pertinacious Palmer permissibility.

4.4.4 Comparison with Observations

We would like to compare the simulated CHAF to the experimental results of Section 4.3.2. If the variation in chorus occurrence as a function of L_{PP} observed in Section 4.3.2 is primarily a propagation effect, then CHAF should behave similarly to the empirically modeled normalized chorus occurrence probability, μ , as a function of L_{PP} . Note that CHAF is merely a proxy measurement of chorus observed probability and is not a probability. To form a proper probability estimation from this data, it would be necessary to estimate the distribution of chorus power as a function of radial distance or f/f_{ceq} and initial wavenormal angle. For lack of this information, we have assumed uniform initial power at all wavenormals and radial distances.

Figure 4.10 shows a comparison of the CHAF at 1 and 4 kHz with the equivalent univariate generalized linear model (GLM) results for μ . The GLM results shown here are limited to chorus occurring at 1 and 4 kHz, instead of the ranges $f < 1.5$ kHz and $f > 3$ kHz shown in Figure 4.4. First, and most importantly, the saturation effect is reproduced for both frequencies. Both μ and CHAF initially increase with decreasing L_{PP} , reach a peak, and then decrease. Their peaks are within 0.5 L. This similarity between CHAF and μ is strongly indicative of the fact that the behavior of μ with respect to L_{PP} is a propagation effect and not a source effect (since only propagation effects are included in the raytracing).

However, we also note the important discrepancy between the L_{PP} values for

the peaks of CHAF and the peaks of μ . For 1 kHz, the peak of μ is at $L_{PP}=2.6$, whereas that for CHAF is at $L_{PP}=3.1$, a difference of $0.5 R_E$. The random error in the measured value of L_{PP} for either μ (measured by clicking on equatorially-mapped EUV images) or CHAF (measured by direct examination of an equatorial slice through the GCPM grid) is estimated to be $\pm 0.1 R_E$, but this is too small to account for the observed discrepancy. Similarly for 4 kHz, the observed peaks are at $L_{PP}=2.7$ and $L_{PP}=2.9$, respectively, a smaller difference of $0.2 R_E$.

There are several different possible causes for the discrepancy between the peaks in μ and CHAF. The first and most obvious cause may be errors in particle densities from the GCPM density model, either in the absolute density or in density gradients. The GCPM model necessarily represents “averaged” conditions for its input values, and may contain systematic biases with respect to the true magnetospheric conditions under which chorus is observed at Palmer.

Another cause may lie in our use of a hybrid energetic electron distribution when calculating Landau damping. The CRRES distribution used outside the plasmasphere uses data from disturbed periods, when $AE > 300$ nT. However, the POLAR distribution used inside the plasmasphere uses data from quiet-to-moderate conditions, when $K_p \leq 4$. Because chorus tends to peak during active periods, the use of quiet/moderate fluxes within the plasmasphere has the effect of artificially lowering the energetic particle flux inside the plasmasphere, therefore lowering the damping coefficients and allowing rays to propagate for a long time within the plasmasphere. Thus, at 1 kHz, ray family 2 from Figure 4.6, which involves extended propagation within the plasmasphere, and which is dominant for $L_{PP} \gtrsim 2.7$, may be less influential than modeled.

Finally, by excluding the prevalent density irregularities that permeate the plasmasphere [e.g., [Carpenter et al., 2002](#), and references therein], we neglect what may be a significant population of waves that are guided by these irregularities. In particular, in the real plasmasphere, density irregularities in the vicinity of the plasmopause may preferentially guide waves to Palmer when the plasmopause is at lower L shells [[Inan and Bell, 1977](#)]. The exclusion of irregularities is an inevitable consequence of using an “averaged” plasma density model, such as the GCPM model for the plasma

density.

One other important discrepancy between the plots of μ and CHAF is that the relative value of μ for low frequencies is significantly greater than that for high frequencies (right panels), whereas the opposite relation is true for CHAF (left panels). This may be due to the fact that higher-frequency waves tend to be generated with lower amplitudes [Burtis and Helliwell, 1975], whereas we have assumed in our raytracing analysis that the amplitude of generated waves is the same across all frequencies.

4.5 Summary

We have proposed in this study that the extent of the plasmapause, denoted L_{PP} , plays a large role in determining the ability for chorus waves to propagate from their equatorial magnetospheric source region to the ground. Using wave data from the ground-based receiver at Palmer Station, Antarctica, together with plasmapause data from the IMAGE EUV instrument, a generalized linear model regression was employed in Section 4.3.2 to show the strong dependence of chorus normalized occurrence on L_{PP} .

The separability of AE and L_{PP} shown in Section 4.3.3 provides evidence that the dependence of chorus occurrence on L_{PP} is in fact a propagation effect, and not simply a confounding source effect (i.e., a consequence of the fact that magnetic substorms both give rise to chorus generation and, separately, cause erosion of the plasmasphere). In particular, Figure 4.5 shows that the general trend of normalized occurrence versus plasmapause persists across a wide range of AE values. This shows that the relation of chorus occurrence to AE (a proxy measure of a source effect), is separable from the relation of chorus occurrence to L_{PP} (a measure of a propagation effect), and therefore, that there is a significant influence of instantaneous plasmasphere extent in determining whether chorus can reach Palmer.

These conclusions were solidified via a reverse raytracing study. By launching rays from Palmer and tracking their power, wavenormal, and equatorial crossings through the expected chorus source region, a measure of the portion of the chorus source region

from which rays may reach Palmer was obtained, which we termed the Chorus Availability Factor, or CHAF. The most salient similarity between how the experimentally observed chorus occurrence (μ) and the raytracing model (CHAF) depend on L_{PP} is the so-called saturation effect, where during experimental observations, chorus is observed on the ground most often for $L \sim 2.6$. It was shown in Section 4.4.4 that this effect is reproduced via raytracing (with a small systematic error in the exact value of L_{PP}) by varying only L_{PP} ; this eliminates the possibility of a confounding source effect, and further reinforces the conclusion that the plasmasphere extent has a direct effect on allowing chorus access to the ground.

The peak of the saturation, either the observed peak of $2.6 \lesssim L_{PP} \lesssim 2.7$ or the modeled peak of $2.9 \lesssim L_{PP} \lesssim 3.1$, is somewhat higher than Palmer's location at $L = 2.4$. One might naïvely expect the peak of chorus to occur at $L_{PP} = 2.4$, because it is at that plasmasphere extent that Palmer Station lies on the plasmopause boundary. However, this theory neglects the mechanism of rays reaching Palmer via magnetospherically reflecting at the northern plasmopause boundary, as in ray family 2 from Figure 4.6 and ray families 2, 3 and 4 from Figure 4.7. This can occur at high plasmasphere extents, and the prevalence of this mode of propagation may be one explanation for why chorus is often observed at Palmer even when the plasmopause is beyond $L = 2.4$.

Additionally, by raytracing in a smooth magnetosphere (except for the obvious density gradient of the plasmopause itself), it was shown that it is possible for chorus to reach the ionosphere within the transmission cone and penetrate to the ground in the absence of any field-aligned guiding structures. This is in contrast to long-held belief that only ducted chorus may access the ground. In fact, in light of the similarities between the raytracing and the experimentally-observed results, it seems plausible that non-ducted chorus is the dominant mode of chorus observed on the ground. Without the constraint of a field-aligned guiding structure, chorus is able to cross L shells as it propagates from the source region to the ground. This explains why Palmer Station, located at a significantly-lower L shell than that of the typical chorus source region, is able to observe chorus as often as it does.

We conclude by saying that, due to the fact that mid-latitude ground observations of chorus are likely to result from non-ducted propagation, these observations are by

no means limited to chorus source regions that lie on the same L shell as the receiver. In addition, plasmasphere extent is an often-neglected but critically important factor in determining chorus propagation to low altitudes and the ground.

Chapter 5

Automated Emission Detection

Although the large number of observed chorus and hiss emissions at Palmer presents a boon for scientific statistics, it has traditionally been difficult to categorize emissions on a large scale. Past attempts have typically used one of two methods. The first is a simplistic thresholding by frequency, satellite position (for in situ measurements), or other parameters which do not take into account the spectral differences between chorus and hiss [e.g., [Meredith et al., 2001, 2004](#); [Smith et al., 2004, 2010](#)]. This method potentially suffers from errors in categorization. An alternative and more reliable approach is a by-hand examination of the broadband emissions [e.g., [Tsurutani and Smith, 1974](#); [Burtis and Helliwell, 1976](#); [Smith et al., 1996](#)]. However, broadband data is not always available and, even when it is, this procedure can be prohibitively time-consuming.

In this chapter, we describe an alternate approach to the problem of distinguishing between chorus and hiss in ground-based broadband ELF/VLF wave data. We use an artificial neural network, which is an example of a machine learning technique which must first be “trained” by the user with example data before it is functional. After being trained with a representative sample of events which have been marked as either “noise”, “chorus” or “hiss,” the neural network is able to operate on an arbitrarily large set of data and automatically sort events into the appropriate categories.

The emission detector was run on 10 continuous years of broadband data from Palmer Station, from May 2000 through May 2010. Results of training indicate

that the neural networks are capable of differentiating between noise and emissions with a 92% success rate and between chorus and hiss with an 84% success rate. Yearly occurrence rates of chorus and hiss are strongly dependent on the geomagnetic disturbance level, as measured by K_p and AE , whereas seasonal occurrence rates are more strongly dependent on variations of the day/night terminator and associated variations in ionospheric absorption.

The work presented in this chapter has been published in the Journal of Geophysical Research as *Golden et al.* [2011].

5.1 Automated Emission Detection

The automated emission detector consists of three broad steps: (a) cleaning of the source broadband data of common sources of interference (discussed in Section 5.1.1), (b) detection of “events” and characterization of their properties (discussed in Sections 5.1.2 and 5.1.3), and (c) automatic categorization of detected events as noise, chorus and hiss, using a sequential pair of complementary neural networks (discussed in Section 5.1.5). In this chapter, we use the term “event” to refer to events output from the event detector which have not yet been categorized as noise, chorus or hiss, and the term “emission” to refer to an event which has been categorized as either chorus or hiss (or is otherwise a priori known to be either of these emissions).

The properties of the neural networks are initially determined using a training set of events which have been categorized by a human operator (discussed in Section 5.1.4), after which the neural networks operate autonomously. These steps are illustrated in the system block diagram in Figure 5.1.

5.1.1 Removal of Sferics and Hum

One inevitable disadvantage of ground-based data versus that gathered via in situ measurements is that they are subject to certain sources of terrestrial interference which are not found in appreciable quantities in space. The two most prevalent and debilitating noise sources for automated detection are sferics, which are the broadband

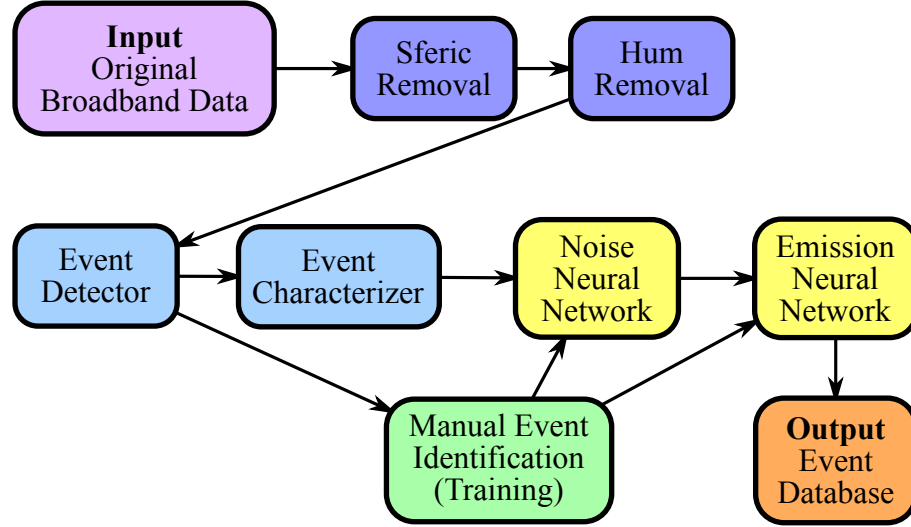


Figure 5.1: Full emission detector system block diagram.

electromagnetic impulses from terrestrial lightning flashes, and hum, which is the anthropogenic parasitic radiation from terrestrial power distribution systems. Both of these noise sources are mitigated prior to event detection.

We first discuss the method of automatically removing sferics from broadband data via a two-step process of sferic identification, followed by sferic removal. The sferic identification process is discussed first and follows the technique of [Said \[2009, p. 110\]](#). Sferics propagating in the Earth-ionosphere waveguide from larger propagation distances have maximal energy roughly concentrated near 9–13 kHz, which is the result of the convolution of their original radiated spectrum with the attenuation characteristics of the Earth-ionosphere waveguide. Therefore, the first step of sferic identification is to apply a pass-band filter between 5–15 kHz to the original full-spectrum 100-kilosamples/sec broadband data. 5 kHz is above the typical observed frequencies for chorus and hiss at Palmer, so this frequency range is unlikely to contain spectral information from those emissions (which may result in “false positives” during sferic detection). The filtered signal is then squared (to increase contrast) and decimated to a sampling frequency of 6 kHz. The absolute value of the resulting signal is the “detection signal.” The detection signal is then thresholded, and any contiguous time points during which the detection signal is above the threshold are

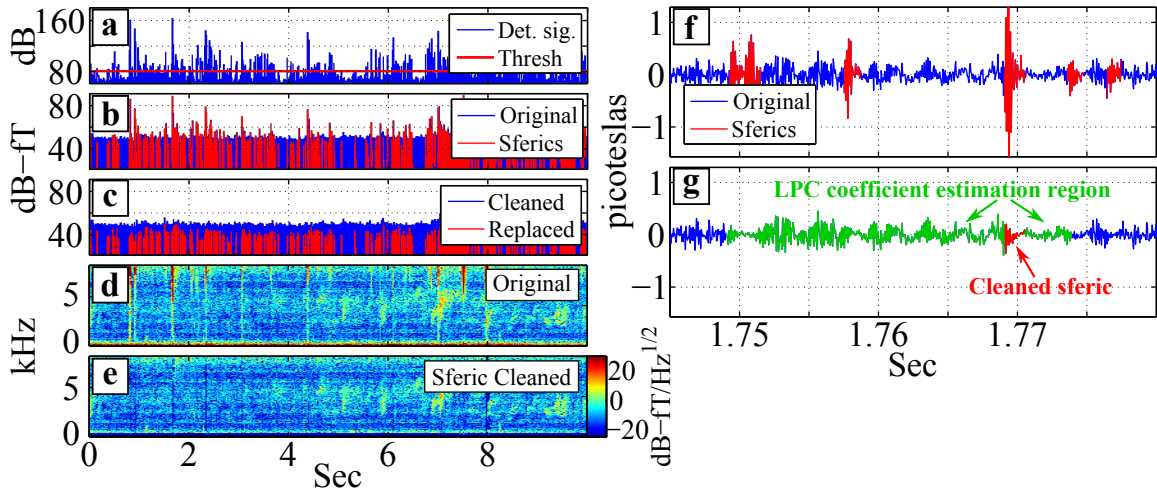


Figure 5.2: Sferic removal procedure shown with 10 sec of Palmer data from 22 April, 2001, 11:50:05 UTC. (a) A detection signal is constructed from data between 5 and 15 kHz, where sferic strength is maximized. Components of this detection signal above a threshold are labeled as sferics. (b) Time-domain data, sampled at 20 kilosamples/sec. Detected sferics are colored red, and original data is colored blue. (c) Time-domain data after sferic removal. The modified sferic locations are marked in red, as above, and their amplitude is now below that of the background data. (d) A spectrogram of the original data, showing a chorus emission that is corrupted by sferics and hum. (e) The same spectrogram after sferic removal. (f) A zoomed-in portion of 35 ms of time-domain data from panel (b). As before, detected sferics are marked in red against the blue background data. The amplitude scale is now linear. (g) Same data as above, after cleaning. A cleaned sferic of interest is shown in red. Data from 20 ms before to 5 ms after the sferic are used in generating the LPC coefficients for interpolation over the sferic, and are shown in green.

labeled as sferics. A threshold of $0.01\sigma_d$, where σ_d is the standard deviation of the detection signal, has been found to work well in practice. Detected sferics of shorter duration than 1 msec are extended to have duration of at least 1 msec. In addition, any discrete sferics which are closer together than 1.5 msec are combined into a single sferic. The output of sferic detection is only the time indices of the data which contain sferics; the original data has not yet been altered up to this point. Figure 5.2 shows the process of sferic detection and removal for an example 10-sec segment of Palmer data. Figure 5.2a shows the detection signal in blue and the threshold at $0.01\sigma_d$ in red.

After sferics have been identified, the cleaning process begins with the unaltered original broadband data. This data is decimated to a sampling frequency of 20 kilo-samples/sec, for a maximum observable frequency of 10 kHz. The decimation process both isolates the frequencies over which chorus and hiss are typically observed, and increases processing speed due to the reduced data volume. Figure 5.2b shows the time-domain data after decimation with detected sferics labeled in red.

Before sferic removal takes place, an IIR highpass filter with a cutoff frequency of 375 Hz is applied to the data to mitigate issues arising from sferic slowtails, i.e., the ELF, high-amplitude components of sferics that propagate below ~ 500 Hz in the transverse electromagnetic (TEM) mode in the Earth-ionosphere waveguide. Because the upper frequency cutoff of slowtails is variable, and chorus and hiss emissions are often seen at ELF frequencies which overlap the slowtail frequency range, the cutoff frequency of the highpass filter is chosen to be a compromise between eliminating most of the slowtail energy while preserving as much of the full bandwidth as possible in which to detect emissions.

Sferics are mitigated by first zeroing-out samples that have been identified as sferics, and then interpolating over those samples. By interpolating over the sferics instead of simply zeroing them out and smoothing the result, we attempt to maintain continuity of the underlying signals, thereby preserving their spectral properties which are used when characterizing events (Section 5.1.3). Interpolation is accomplished using linear-predictive coding (LPC) with an autoregressive (AR) model of the signal [Godsill and Rayner, 1998, Sec. 5.2.2]. Under the AR model, a given sample of the signal is modeled as a linear combination of prior samples, as

$$x_n = \sum_{i=1}^P a_i x_{n-i} + e_n \quad (5.1)$$

where x_n represents a sample at discrete time index n , P is the order of the AR process, the P coefficients a_i are the AR coefficients, and e_n is the error. Define the

matrix \mathbf{A} as

$$\mathbf{A} = \begin{bmatrix} -a_P & \dots & -a_1 & 1 & 0 & 0 & \dots & 0 \\ 0 & -a_P & \dots & -a_1 & 1 & 0 & \dots & 0 \\ \vdots & \ddots & \ddots & \ddots & \ddots & \ddots & \ddots & \vdots \\ 0 & \dots & 0 & -a_P & \dots & -a_1 & 1 & 0 \\ 0 & \dots & 0 & 0 & -a_P & \dots & -a_1 & 1 \end{bmatrix}. \quad (5.2)$$

Then, the error sequence can be expressed as

$$\mathbf{e} = \mathbf{A}\mathbf{x}. \quad (5.3)$$

For a given sferic, we create three segments of data: \mathbf{x}_u is the detected sferic, which has been zeroed-out and now consists of unknown values to be estimated, \mathbf{x}_b is 20 msec of data before the first sample of \mathbf{x}_u , and \mathbf{x}_a is 5 msec of data after the last sample of \mathbf{x}_u . Because sferics are cleaned sequentially, \mathbf{x}_b is known to be free of sferics, while \mathbf{x}_a is not. The entire data segment of interest is then given by

$$\mathbf{x} = \begin{bmatrix} \mathbf{x}_b \\ \mathbf{x}_u \\ \mathbf{x}_a \end{bmatrix}. \quad (5.4)$$

We can also express the known and unknown values of \mathbf{x} as $\mathbf{x}_k = [\mathbf{x}_b^T \mathbf{x}_a^T]^T$ and \mathbf{x}_u , respectively.

The entire sequence \mathbf{x} is used to estimate the LPC coefficients, via the `lpc` function in MATLAB, including \mathbf{x}_u which consists of all zeros. Although it may seem that only \mathbf{x}_b should be used to estimate the LPC coefficients, since \mathbf{x}_u consists of all zeros and \mathbf{x}_a may contain sferics, in practice, there is negligible difference in the results. The risk of including sferics in the LPC estimation via \mathbf{x}_a is mitigated by ensuring that it is significantly smaller (5 msec versus 20 msec) than the sferic-free portion of the estimation, \mathbf{x}_b . For reference, at the implemented sampling rate of 20 kilosamples/sec, the 25 msec of data used in LPC coefficient estimation consists of 500 samples.

To estimate the missing data \mathbf{x}_u , partition the columns of \mathbf{A} into columns for known \mathbf{A}_k and unknown \mathbf{A}_u indices of \mathbf{x} such that

$$\mathbf{e} = \mathbf{A}_k \mathbf{x}_k + \mathbf{A}_u \mathbf{x}_u. \quad (5.5)$$

The objective is to obtain an estimate of \mathbf{x}_u given \mathbf{A} and \mathbf{x}_k , which minimizes the mean-squared error, which is proportional to $\mathbf{e}^T \mathbf{e}$. This is achieved by setting \mathbf{e} to zero and solving for \mathbf{x}_u , as

$$-\mathbf{A}_k \mathbf{x}_k = \mathbf{A}_u \mathbf{x}_u. \quad (5.6)$$

Assuming that \mathbf{A}_u is skinny and full rank, the traditional least squares solution is

$$\mathbf{x}_u = -(\mathbf{A}_u^T \mathbf{A}_u)^{-1} \mathbf{A}_u^T \mathbf{A}_k \mathbf{x}_k. \quad (5.7)$$

The solution for \mathbf{x}_u gives the data sequence with which to replace the zeroed-out sferic. This process is repeated sequentially for every detected sferic in the data.

Figure 5.2c shows the result of the sferic removal process in the time domain. Energy in the samples that contained sferics has been reduced to below the background levels of the signal. Figures 5.2d,e show spectrograms of the signal before and after sferic removal. Although some broadband “nulls” have been introduced in the place of more powerful sferics (which generally have a longer extent in time than less powerful ones), the majority of low-amplitude sferics are removed without nulls and there is no broadband ringing as would have resulted from simply zeroing-out the sferics in the time-domain data. Given that events are detected based on their spectrum (Section 5.1.2), these occasional nulls are far more tolerable than either the original sferics or nulls for every sferic.

Figure 5.2f shows a zoomed-in portion of 35 msec of the time-domain data from Figure 5.2b, highlighting several detected sferics, where now the amplitude scale is linear instead of logarithmic (1 pT=60 dB-fT). Figure 5.2g shows in green the range of data used for estimating the LPC coefficients for the given cleaned sferic, shown in red.

Another noise source observed at Palmer is hum, which consists of parasitic leakage

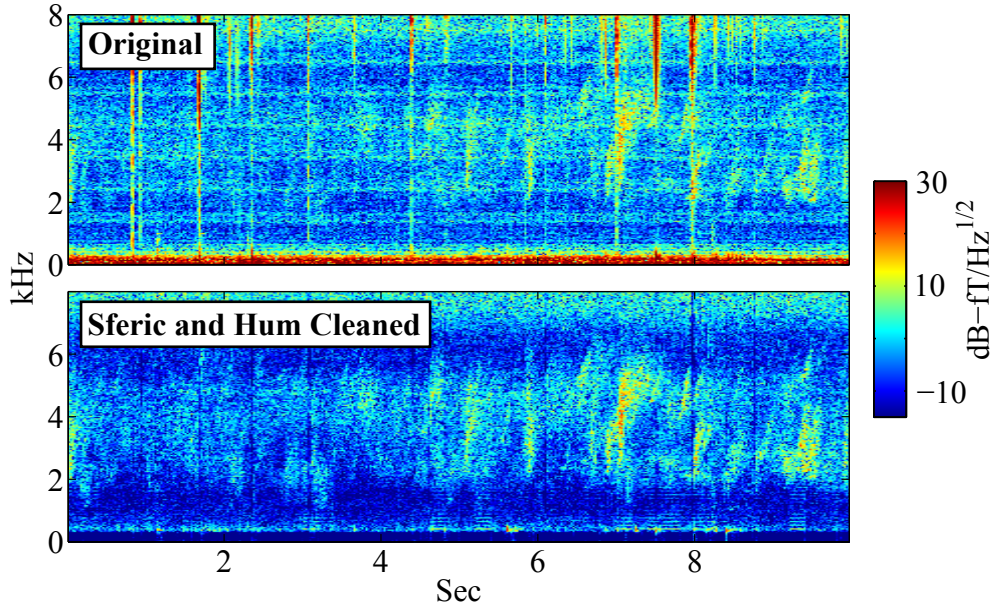


Figure 5.3: Result of removing both sferics and hum from data. This is the same 10-sec broadband data segment as in Figure 5.2. In the cleaned data, it is much easier to identify the chorus emission between 2 and 6 kHz.

of 60-Hz noise and its harmonics from the Palmer Station power distribution system. Hum is mitigated using the technique of *Cohen et al. [2010]*. Hum frequency is estimated via the “quadratic interpolation” method using odd hum harmonics 7–31 (420, 540, ..., 1860 Hz). Odd harmonics are chosen because they are significantly more intense than even harmonics at Palmer. The lower frequency of 420 Hz is the first odd harmonic in the passband of the slowtail highpass filter, and hum is usually no longer significant at Palmer above the upper frequency of 1860 Hz. After its frequency has been estimated, hum is removed via the “least squares estimation” method. This process is repeated in intervals of 200 ms to account for a potentially slowly changing hum frequency.

Figure 5.3 shows spectrograms of the same data segment from Figure 5.2 before and after both sferics and hum are removed. Contrast of the chorus emission between 2 and 6 kHz is greatly enhanced after cleaning, emphasizing the usefulness of this pre-processing step before initiating the actual detection of emissions.

5.1.2 Event Detection

Once data is cleaned, events may be detected which are candidates for being classified as chorus or hiss. In contrast to transient electromagnetic phenomena from lightning, such as sferics and whistlers, and other transient emissions, such as periodic and quasi-periodic emissions [e.g., [Helliwell, 1965](#), p. 206–207] [[Sazhin and Hayakawa, 1994](#)], chorus and hiss emissions may persist for minutes or hours with similar spectral characteristics over their entire duration (see Appendix [B](#) for examples of these and other emissions at Palmer). Thus, when examining individual 10-sec records for each synoptic epoch, we are interested only in events whose power spectral densities (PSDs) are approximately constant throughout the 10-sec record. It is natural then to detect events and their associated bandwidth using the one-dimensional frequency spectrum of the 10-sec record, instead of the two-dimensional spectrogram. A standard method of estimating the spectrum of a signal is via the Welch periodogram [[Welch, 1967](#)], which, assuming the same windowing and Fourier transform parameters, can be thought of as the average of a spectrogram matrix over time. However, the Welch periodogram in its usual form is not adequate for our purposes. Despite the sferic removal discussed in Section [5.1.1](#), certain types of high-amplitude, longer-duration impulsive signals may remain in the cleaned data, such as tweeks (the highly-dispersed components of sferics near the Earth-ionosphere waveguide cutoff frequencies) and lightning-generated whistlers (sferic energy which has escaped into the magnetosphere, become dispersed in the magnetospheric plasma, and returned through the ionosphere in the opposite hemisphere). Though these transient signals may last for less than one second, their high amplitude may result in a contribution to the PSD of the Welch periodogram which is disproportionate to their duration. This may in turn mask a continuous chorus or hiss emission with a lower PSD at the same frequency. To mitigate this problem, we discard the Welch periodogram, which is formed from the mean of the columns of a spectrogram, in favor of what we term the “Welch mediogram” (or more simply, “mediogram”) formed from the median of the columns of a spectrogram. Like any median filter, the mediogram has the property that it emphasizes spectral content which is persistent in time and de-emphasizes transient signals.

Six common types of events are shown in Figure 5.4, where the full 10-sec record for each synoptic epoch is shown and the event is marked with a red box. Note that, although both the periodogram (blue, “mean”) and mediogram (green, “median”) PSDs are shown, only the mediogram is used in event detection. The most common sources of noise are those from lightning, including sferic bursts from intra-cloud lightning (which appear in broadband data as many closely-spaced low-amplitude sferics), tweeks, slowtails (Figures 5.4a,b,c) and whistlers (Figure 5.4d). The events of interest are chorus and hiss (Figures 5.4e,f). Although periodic and quasi-periodic emissions do occur at Palmer’s invariant latitude ($\Lambda = 50^\circ\text{S}$) (see, e.g., observations at Seattle, $\Lambda = 54^\circ\text{N}$, Dunedin, $\Lambda = 51^\circ\text{S}$, Norwich, $\Lambda = 55^\circ\text{N}$, and others in [Helliwell \[1965, Sec. 7.1\]](#)), they are generally not detected in Palmer data by the event detector due to their relative rarity compared to chorus and hiss, and also due to their transient behavior, which is de-emphasized by the mediogram.

The arithmetic difference between the PSDs of the Welch periodogram and the Welch mediogram is generally a good measure of the “impulsiveness” of a given event. This is illustrated particularly well in the hiss event in Figure 5.4f, where above ~ 3 kHz, there is a large difference between the mediogram and periodogram PSD due to impulsive sferics, while below ~ 3 kHz, the difference is minimal due to the constant-PSD hiss emission.

As mentioned, sferic removal is only effective on the short-time impulsive sferics themselves. The sferic removal process does not remove any other products of terrestrial lightning. Fortunately, two of the most prevalent noise sources, namely sferic bursts and slowtails (Figures 5.4a,c), have fairly predictable spectrums. Additionally, due to the intensity of these noise sources, it is infeasible to find emissions in the same frequency band. Therefore, the first step of the event detection process is to determine the frequency extents of sferic bursts and slowtails in a given broadband record, and look only for emissions outside of these ranges.

We define the terms “peaks” and “valleys” as the local maxima and minima in the mediogram, respectively. Slowtails dominate the spectrum at low frequencies, from the 375 Hz slowtail highpass filter cutoff to slightly above. Slowtail PSD has its maximum at frequencies below the filter cutoff and rolls off quickly with increasing

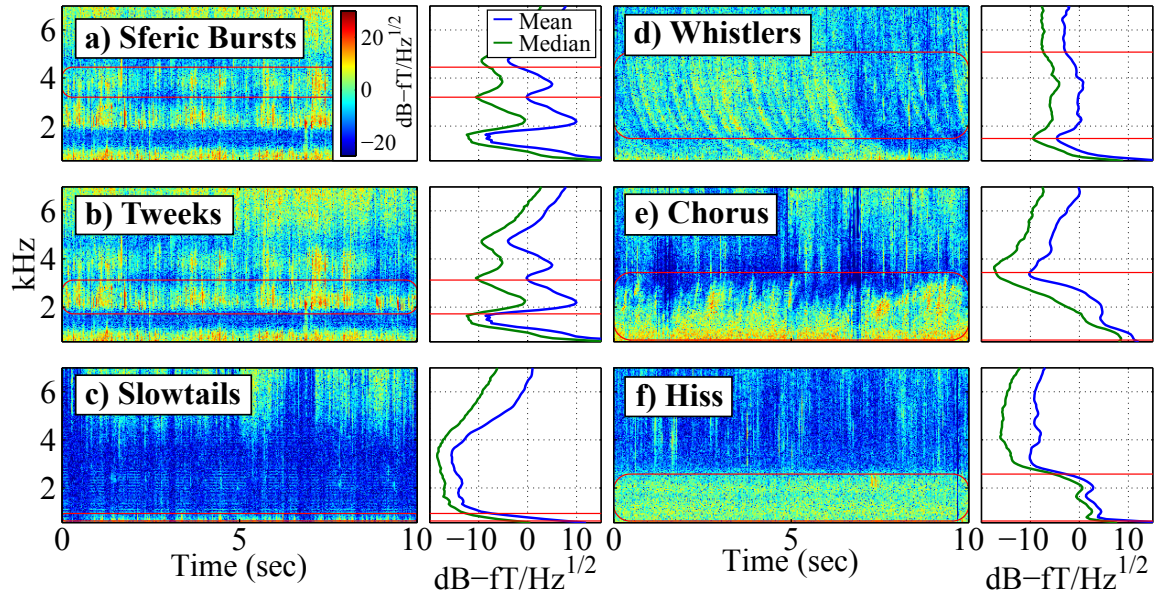


Figure 5.4: Examples of common types of events as output by the event detector. Spectrograms for each type of event are shown, along with the associated periodogram (blue line) and mediogram (green line) for that data segment. The detected event is indicated with a red box. Although the majority of high-amplitude sferics are removed in the broadband cleaning process prior to event detection, *sferic bursts* are not removed in this manner and may be detected as events. Similarly, *tweeks* and *slowtails* are not removed by the sferic removal process due to their non-impulsive nature. *Whistlers* are a common broadband emission at Palmer and are of scientific interest for a variety of reasons, but they are not used in this study, and are therefore considered noise. *Chorus* and *hiss* are the emissions of interest in this study.

frequency on a mediogram. An empirically-determined reasonable estimate for the slowtail upper cutoff in a given synoptic epoch is one of (a) the frequency of the first (lowest frequency) valley, (b) the first frequency at which the mediogram slope is less steep than -20 dB/kHz or (c) 600 Hz, whichever is lowest.

The high end of the spectrum is dominated by sferic bursts. Sferic burst energy peaks above the ~ 8 kHz antialiasing filter cutoff, so its PSD tends to rise monotonically up to that cutoff. An empirically-determined reasonable estimate of the sferic burst lower cutoff is either (a) the highest frequency at which the mediogram PSD (smoothed over 1 kHz) becomes monotonically increasing up to the antialiasing filter cutoff or (b) 8 kHz, whichever is lowest. We refer to the slowtail and sferic burst cutoffs as the sferic lower and upper cutoffs, respectively.

Between the sferic cutoffs, we then search for events. First, all peaks between the two sferic cutoffs are detected and assumed to be candidates for unique events. Because low-frequency emissions are often seen on the edge of the sferic lower cutoff, the frequency of the sferic lower cutoff is added to the list of peaks (though, due to the fact that emission and slowtail PSDs reach their maximums below the sferic lower cutoff, it is rarely a true peak). Second, the 3-dB points for each peak, defined as the nearest frequencies above and below each peak at which the mediogram PSD is 3 dB or more below that of the peak, is determined. The width of the peak is then defined as the frequency difference between its two 3-dB points, i.e., the full width at half maximum (FWHM). If either 3-dB point is beyond either sferic cutoff, then the FWHM is defined as twice the frequency difference between the peak and the remaining 3-dB point. If both 3-dB points are beyond the sferic cutoffs, the peak is discarded. Additionally, peaks which have a FWHM of less than 100 Hz are discarded.

The upper and lower “extents” of each peak are then determined to be the closest frequencies that can be reached from the peak for which (a) the mediogram PSD is at least 9 dB less than the PSD at the peak, or if no such point is found, (b) the frequency of the lowest mediogram PSD between the peak and the respective sferic cutoff, inclusive. Additionally, the extents may not include any mediogram PSDs which are greater than the given peak. The bandwidth of a given peak is then defined as the frequency difference between its upper and lower extents. Peaks with

bandwidths less than 300 Hz are discarded. Finally, each peak is checked to determine whether it is contained within the extents of a higher-PSD peak. If so, it is discarded.

Each peak which passes this gauntlet of tests is then labeled as an “event,” and is a potential candidate for being categorized as an emission. At this point, events are not yet categorized, and may include either chorus, hiss or noise (i.e., anything other than chorus or hiss).

The relevant metric for the efficacy of the event detector is its missed detection rate, i.e., the percent of chorus or hiss emissions that the event detector fails to identify. In this implementation, there are no false positives from the event detector since those events are discarded using the noise neural network (discussed in Section 5.1.5). To evaluate the missed detection rate, we manually examined a subset of synoptic epochs that were processed with the event detector. In 1000 synoptic epochs, we noted 15 chorus or hiss emissions that were not detected by the event detector, primarily as a result of their blending into the sferic cutoffs.

We can then interpret each sampled synoptic epoch as an independent Bernoulli trial as described in Section A.3. Setting $n = 1000$ and $\hat{p} = 0.015$, and using a null hypothesis, H_0 , and alternate hypothesis, H_1 , of the form,

$$H_0 : p \geq p_0 \text{ vs. } H_1 : p < p_0, \quad (5.8)$$

with $z = -1.64$, we can solve (A.9), using the minus sign in that equation, to get $p_0 = 0.023$. Thus, we can state with 95% confidence that the missed detection rate of the event detector is less than 2.3%, or conversely, at least 97.7% of emissions are detected.

5.1.3 Event Characterization

Once events are detected, various scalar characteristics are determined about each event. These characteristics are used as inputs to the neural network, described in Section 5.1.5. Each characteristic is chosen because of the potential that it may have, possibly in conjunction with other characteristics, to aid the neural network in differentiating between different types of events. A total of 19 characteristics are

Table 5.1: List of Event Characteristics and Units

No.	Name	Units
1	Year	Years (2000–2010)
2	Day of year	Days (1–366)
3	Peak frequency	Hz
4	Upper cutoff frequency	Hz
5	Lower cutoff frequency	Hz
6	Bandwidth	Hz
7	Max positive mediogram slope	(dB-fT/Hz ^{1/2})/Hz
8	Max negative mediogram slope	(dB-fT/Hz ^{1/2})/Hz
9	Avg mediogram PSD	dB-fT/Hz ^{1/2}
10	Avg periodogram PSD	dB-fT/Hz ^{1/2}
11	Max mediogram PSD	dB-fT/Hz ^{1/2}
12	Max periodogram PSD	dB-fT/Hz ^{1/2}
13	Median power	dB-fT
14	Time to day/night terminator	Hours
15	Burstiness	Hz
16	XC slope	sec/Hz
17	XC correlation coefficient	Unitless (0–1)
18	XC mean value	Unitless (0–1)
19	XC mean standard deviation	Unitless (0–1)

determined for each event; they are summarized in Table 5.1 and are discussed in more detail below. As many reasonable characteristics were chosen as possible, without an in-depth analysis of the influence of each characteristic on the result.

The year and day of year of the synoptic epoch are included to incorporate seasonal and long term differences in emission characteristics. The peak frequency, upper cutoff frequency, lower cutoff frequency and bandwidth are basic parameters for each event, and are determined during event detection, described in Section 5.1.2.

Additional emission spectral parameters include the maximum positive and negative mediogram slopes over the course of the emission (measurements of how rigidly band-limited the event is), average mediogram and periodogram PSD (the difference of which is a measure of the impulsiveness of the event) and maximum mediogram and periodogram PSDs. The “median power” is the integral of the mediogram PSD

(in fT^2/Hz) over the bandwidth of the event. This value is integrated in power-space, and therefore is different from the event's average mediogram amplitude, which is averaged in log-space and is not multiplied by the bandwidth.

The “time to day/night terminator” is defined as the time from the synoptic epoch to the nearest terminator, either dawn or dusk. If Palmer is in darkness during the synoptic epoch, then this number is positive; otherwise it is negative. This parameter is incorporated because all types of events are more common during darkness; this is a consequence of the lower absorption of the ionosphere during the night that affects both trans-ionospheric propagation and propagation in the Earth-ionosphere waveguide.

The “burstiness” parameter is somewhat more involved and attempts to measure the canonical spectral difference between chorus and hiss, namely that the former is a “bursty” emission (containing discrete structure in time) while the latter is not. Burstiness is estimated as follows. First, the event is mixed to baseband by multiplying with a cosine at the event center frequency and decimating to a sampling frequency equivalent to the bandwidth of the event. Then, the signal is squared so that it is in units of power, and decimated again to a sampling frequency of 100 Hz. Finally, the Welch periodogram is calculated for the signal, and the centroid of the Welch periodogram (for positive frequencies only) is obtained. In this case, the centroid represents the mean frequency of the Welch periodogram, weighted by periodogram amplitude (in units of power) and is a measure of the frequency at which the signal power tends to be concentrated. Signals which are not bursty (such as hiss) will have a spectrum which resembles random noise and will have a centroid near the center of the spectrum, at 25 Hz. Signals which are bursty (such as chorus) will have spectral power concentrated near the low end of the spectrum and will have a centroid lower than 25 Hz (representing a significant amplitude modulation of a few Hz). The centroid is used as the burstiness parameter and has units of Hz.

The four remaining parameters, prefixed with the letters “XC,” represent parameters relating to the cross-correlation of adjacent rows of a signal spectrogram. For each adjacent pair of rows in the spectrogram (corresponding to a pair of frequencies), the cross-correlation is computed. The cross-correlation vector provides a measure of the

total correlation between the two rows (given by the peak value of the cross-correlation vector) and the dominant slope of the event in that frequency range (given by the lag of the peak of the cross-correlation). The “XC slope” parameter is calculated as the centroid of the average (over frequency) of all of the cross-correlation vectors, divided by the frequency step of the spectrogram. It is a measure of the dominant slope of the event and has units of sec/Hz. The “XC correlation coefficient” is the mean of the amplitudes of each cross-correlation vector at the lag indicated by XC slope and is a measure of the “strength” of that dominant slope, from 0 to 1. “XC mean value” is the mean of all values of all cross-correlation vectors; a higher value indicates a wider range of lags over which correlation is high, and suggests thicker event elements in time (e.g., chorus and whistlers) as opposed to thinner ones (e.g., sferics). “XC mean standard deviation” is the mean of the standard deviations of each cross-correlation vector and is a complementary parameter to the XC mean value. Events which tend to have large XC correlation coefficients include whistlers, which have negative slopes, chorus emissions, which usually have positive slopes, and sferics, which usually have slopes near zero. Hiss tends to have a low XC correlation coefficient since its spectrogram rows are random noise, and therefore are minimally correlated. Additionally, hiss tends to have an XC slope near zero, since its cross-correlation vectors appear as random noise with centroids near zero lag.

5.1.4 Construction of the Neural Network Training Set

After the events have been detected and characterized, the next step in the emission detection process is the construction of a training set for the neural network. The set of events included in the training set is a subset of all (uncategorized) events output from the event detector. We use events from 1 day out of every 15 for training, or approximately 24 days per year, for a total of approximately 240 days of training data for the 10-year data set. This cadence is a compromise between having adequate training data and the general tediousness of the training process. The training data used contains 10,013 out of a total of 154,639 events for the 10 years of data used in this study.

Assembly of the training set is simple and repetitive. The human trainer (the author of this thesis) makes use of a graphic user interface which displays a spectrogram for a given event in the training set. The event is highlighted on the spectrogram with a red box. The trainer categorizes the event as either (1) chorus, (2) hiss, (3) an unknown non-noise emission (which the trainer is unable to categorize as chorus or hiss from the spectrogram), or (4) noise. This process is repeated for all 10,013 events in the training set. In the case of a “mixed” detection with more than one type of event in the same bandwidth (e.g., the relatively common simultaneous whistlers and hiss), the detected event is categorized according to the event with the greater PSD. This decision is made under the principle that the characteristics of the detected event (discussed in Section 5.1.3) are primarily based on the event with the greater PSD (i.e., the dominant constituent of the detected event’s spectrum).

The result of this procedure is a $1 \times 10,013$ vector of “target” values, each of which is either chorus, hiss, unknown emission or noise. Independently, the automated event characterizer determines the characteristics for each event, resulting in a $19 \times 10,013$ matrix of input values. Note that the input values are not used by the trainer in assembling the training set; only the event time, frequency range and broadband spectrogram are used.

5.1.5 Neural Network Implementation and Training

The training set is then in a suitable format for being used to train a neural network. The MATLAB Neural Network Toolbox is used for all neural network operations. Two completely separate neural networks are implemented: a neural network to distinguish between emissions and noise, which we refer to as the “noise neural network,” and a neural network to distinguish between chorus and hiss, which we refer to as the “emission neural network.” A neural network is capable of having an arbitrary number of outputs, and we could have created a single neural network to distinguish between chorus, hiss and noise. However, we choose to use a sequence of two neural networks so that they may be trained using different training sets, as is explained later.

Both the noise and emission neural networks are known in MATLAB as “pattern

recognition networks,” and have identical structure, shown in Figure 5.5. Each neural network consists of a 20-neuron hidden layer followed by a single-neuron output layer and takes as input the 19-value event characteristics vector (\mathbf{p}) described in Section 5.1.3. Trial and error has shown that 20 neurons in the hidden layer is sufficient to achieve reasonable performance for both networks. Each neuron in the hidden layer contains a single weight for each of the 19 inputs and a single bias. The resulting matrix of weights (\mathbf{IW}) is a 20×19 matrix, and the resulting vector of biases (\mathbf{b}_1) is a 20×1 vector. Similarly, the single neuron in the output layer contains 20 weights, one for each output of the 20 neurons from the hidden layer and a single bias. The resulting matrix of weights (\mathbf{LW}) is a 1×20 matrix, and the resulting bias (\mathbf{b}_2) is a scalar. The transfer function for both layers is the hyperbolic tangent sigmoid function (tansig), which transforms unbounded input into bounded output in the range $[-1, +1]$. The output of the output layer is further thresholded so that the final output of the network is a Boolean true/false value (corresponding to emission/noise and hiss/chorus, respectively). In theory, the threshold may be set to preferentially maximize true positives or minimize false positives, but in practice, it is left at the point which minimizes the total number of detection errors. The output of the hidden layer is given by

$$\mathbf{a}_1 = \text{tansig}(\mathbf{b}_1 + \mathbf{IWp}) \quad (5.9)$$

and the output of the output layer before thresholding is given by

$$\mathbf{a}_2 = \text{tansig}(\mathbf{b}_2 + \mathbf{LW}\mathbf{a}_1). \quad (5.10)$$

The training set used for the noise neural network is the full training set (10,013 events), with targets set to 0 if the event is noise and 1 if the event is any type of emission other than noise. The training set used for the emission neural network is only those events in the full training set which have been categorized as chorus or hiss (2453 events); unknown emissions and noise are discarded from the training set for this neural network. The principle behind this is that, once noise events are eliminated with the noise neural network, the emission neural network will categorize all remaining events – including those which would be categorized by the trainer

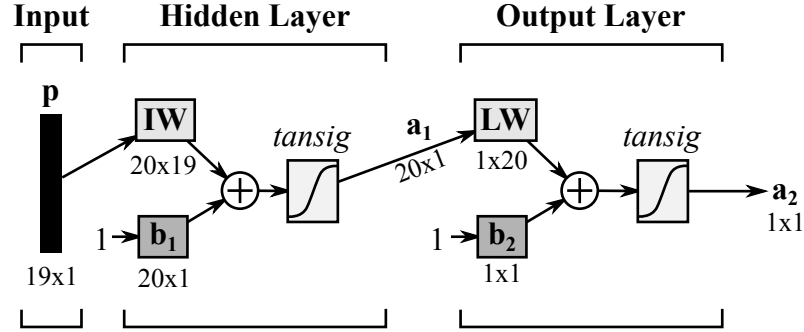


Figure 5.5: Neural network block diagram. This block diagram describes both the noise neural network and the emission neural network, which are structurally equivalent, but have different weights and biases. The size of each element is indicated by the dimensions below the given element; e.g., \mathbf{IW} is a matrix with 20 rows and 19 columns.

as unknown emissions – as either chorus or hiss. In this way, the neural network is expected to *outperform* the trainer by categorizing emissions based on their similarity, in the 19-dimensional property space shown in Table 5.1, to events which the trainer *is* able to categorize.

For example, let us say that the human trainer categorizes emission A as chorus and emission B as hiss, but is unable to make a decision about emission C. The neural network would then categorize emission A as chorus, based on its similarity to other known chorus emissions (previously categorized by the trainer), and emission B as hiss, based on its similarity to other known hiss emissions. Finally, the neural network would examine the characteristics of emission C; if they more closely resembled those of known chorus emissions, emission C would be categorized as chorus, and if they more closely resembled those of known hiss emissions, emission C would be categorized as hiss. In this way, the neural network is capable of making intelligent decisions about event categorization based on information and processing power which are not readily available to the trainer.

Both neural networks are trained using the scaled conjugate gradient backpropagation method [Møller, 1993] with initial weights and biases chosen via the Nguyen-Widrow initialization algorithm [Nguyen and Widrow, 1990]. The training set for each neural network is split into three groups: the “main” set (70% of values), the

“validation” set (15% of values) and the “test” set (15% of values). The backpropagation training procedure is performed only with the main set. The validation set is used to improve the generalization of the neural network via early stopping as follows. During training, the error of the main set (defined as the mean squared error between the targets and the current outputs of the network) decreases monotonically and, initially, so does the error of the validation set. However, at a certain point, the error of the validation set stops decreasing due to overfitting of the neural network to the main set. The training is halted after the error of the validation set fails to decrease for six iterations. In contrast, the test set is a completely independent measure of the effectiveness of training and is not used in the training at all.

The results of training the noise neural network are shown via the confusion matrices in Figures 5.6. Each training set is split into three subsets: the “main” set (70% of inputs), the “validation” set (15% of inputs) and the “test” set (15% of inputs). The “total” set represents the sum of all three sets. The boxes in each confusion matrix are described with respect to the main confusion matrix in the upper left. Squares 1 and 5 (green background) represent the number of neural network outputs which matched the targets, and squares 2 and 4 (red background) indicate the number of neural network outputs which failed to do so. Squares 7 and 8 represent the percent of each *target* class which were (upper green number) and were not (lower red number) categorized correctly. Squares 3 and 6 represent the percent of each *output* class which were and were not categorized correctly. Square 9 (blue background) indicates the total percent of outputs which matched their targets (correct detections, upper green number) and those that did not (lower red number). It can be seen that the noise neural network correctly categorizes 91.9% of the input data and shows no signs of overfitting, as seen from the fact that the total success rates of the main and test sets are very similar (92.1% versus 91.3%).

The emission neural network, shown in Figure 5.7, performs nearly as well, correctly categorizing 87.9% of emissions, but with some symptoms of overfitting. This can be seen from the fact that the percent of correct detections for the main set (89.5%) is significantly higher than that of the test and validation sets (both 84.0%). However, when we tried to reduce overfitting by reducing the number of neurons in

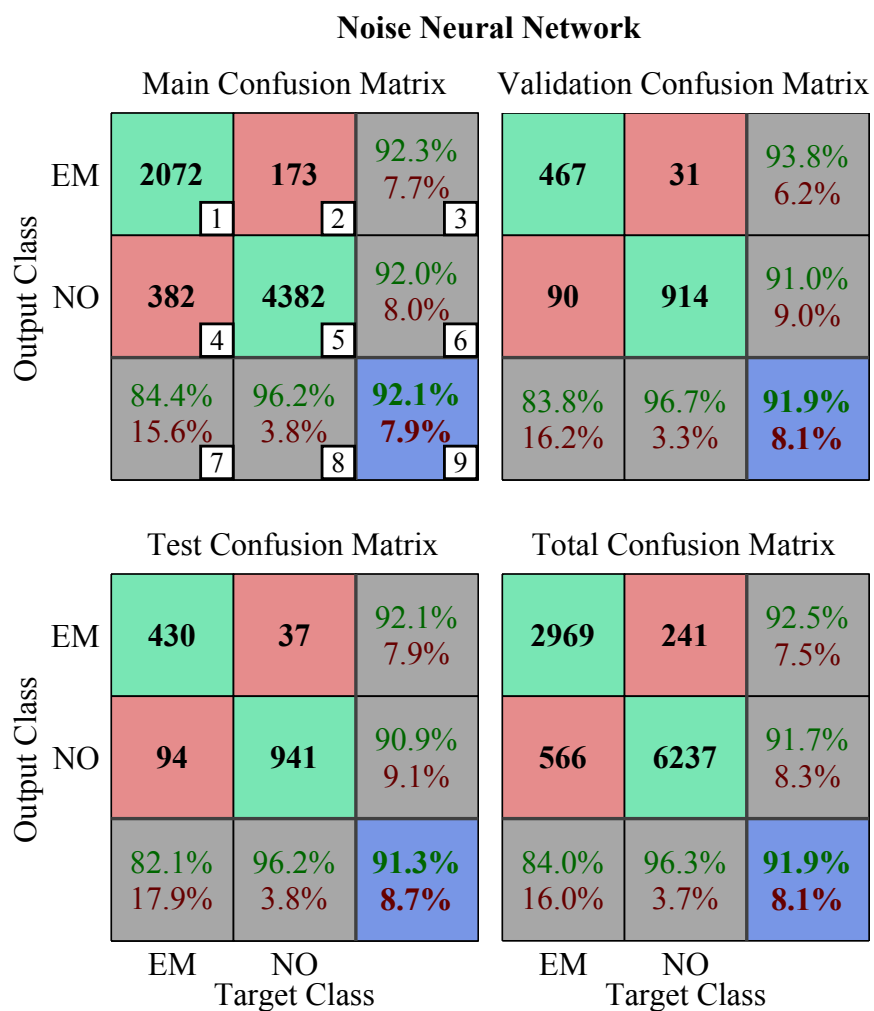


Figure 5.6: Neural network confusion matrices for training of the noise neural network. The labels “EM” and “NO” mean emissions and noise, respectively. The total success rate for this neural network is around 92%. Instructions on interpreting the confusion matrices are in the text.

the hidden layer, the number of correct detections decreased for all three sets. Therefore, we tolerate this mild overfitting and accept the fact that the correct detection rate of the emission neural network is expected to be closer to the test and validation rates of 84.0% than the total rate of 87.9%.

Once the neural networks have been trained, they are ready to be used on the full catalog of 154,639 detected events over the 10 years of data for this study. Initially, all events are passed through the noise neural network and are categorized as either noise or emissions. All noise events are discarded. All emission events are then passed through the emission neural network, and they are further categorized as either chorus or hiss. The end result is a database of all chorus and hiss emissions detected over the course of this study, including time, frequency, amplitude, and other characteristics from Section 5.1.3. From this database, many different statistics may be determined about chorus and hiss emissions observed at Palmer, a small subset of which is discussed in Section 5.2.

5.1.6 Algorithm Speed

All aspects of the emission detector are implemented in MATLAB Version 2010a. The spheric removal, hum removal, event detection and event characterization steps are run in parallel using the MATLAB parallel computing toolbox with eight simultaneous threads on a Dell PowerEdge R710 rack-mount server with two quad-core Intel Xeon X5550 processors with 8 MB of cache and 16 GB of system RAM. The median time for cleaning one day of data (consisting of a total of 960 sec of broadband data from four 10-sec data segments per hr) is 234 sec. The median time for detecting and characterizing events for one day of data is 16 sec.

The neural networks are run on a workstation with an AMD Athlon 64 X2 4200+ dual-core processor with 512 kB of cache and 4 GB of system RAM. The total time required for the human trainer to create the training set by manually categorizing emissions is approximately one work week. The time required to run the training algorithm on the neural networks and to run the neural networks on the detected events for the entire 10-year data set is less than five minutes.

Emission Neural Network						
Main Confusion Matrix			Validation Confusion Matrix			
Output Class	HI	1010 127 88.8% 11.2%		213 39 84.5% 15.5%		
	CH	53 527 90.9% 9.1%		20 96 82.8% 17.2%		
		95.0% 5.0% 80.6% 19.4% 89.5% 10.5%		91.4% 8.6% 71.1% 28.9% 84.0% 16.0%		
Test Confusion Matrix			Total Confusion Matrix			
Output Class	HI	211 46 82.1% 17.9%		1434 212 87.1% 12.9%		
	CH	13 98 88.3% 11.7%		86 721 89.3% 10.7%		
		94.2% 5.8% 68.1% 31.9% 84.0% 16.0%		94.3% 5.7% 77.3% 22.7% 87.9% 12.1%		
Target Class			Target Class			

Figure 5.7: Same as Figure 5.6, but for the emission neural network. The labels “HI” and “CH” mean hiss and chorus, respectively. Due to slight overfitting, the success rate for this neural network is probably closer to the test set success rate of 84.0% than to the total set success rate of 87.9%.

If only the CPU-bound cleaning and event detection/characterization steps are considered, the chorus/hiss detection system runs at a rate of 350x real time on modern server hardware, assuming four 10-sec data segments sampled per hr. If data were sampled continuously, with 360 10-sec data samples per hr, the speed would drop to 3.8x real time. In the future, the detection system may be easily implemented in a real time setting at field sites using standard workstation hardware. However, in a real time setting, it would be necessary to periodically add current data to the training set and re-train the network, in the event that site conditions change over time (for example, due to solar cycle variations or changes in system calibration).

5.2 Solar Cycle Variation of Emissions

5.2.1 General Trends

The first property of chorus and hiss which we investigate using the emission database is the most common frequency and time ranges for emission occurrence at Palmer. This property is visualized using the “cumulative spectrogram” approach described in Section 3.1.2. The cumulative spectrogram is the sum, in log-space, of the average mediodiagram amplitude of each emission, divided by the number of available data files for each synoptic epoch. This is effectively a plot of normalized emission occurrence, weighted by emission PSD, with respect to frequency and local time.

Cumulative spectrograms of chorus and hiss emissions from May 2000 through May 2010 are shown in Figure 5.8. This figure may be compared with Figure 3.4, though, in Figure 5.8, we have broken down chorus and hiss in a different way. In particular, when chorus and hiss appear in the same broadband record, regardless of whether they appear in the same or different frequency bands, we labeled that entire broadband record as *chorus with hiss* in Chapter 3. In contrast, in this study, we independently label multiple emissions in a given broadband record if they occur in different frequency bands. Additionally, we label a given bandlimited emission as “chorus” if it contains chorus-like features, regardless of background hiss in the same frequency band, in light of the fact that the background hiss may simply be an

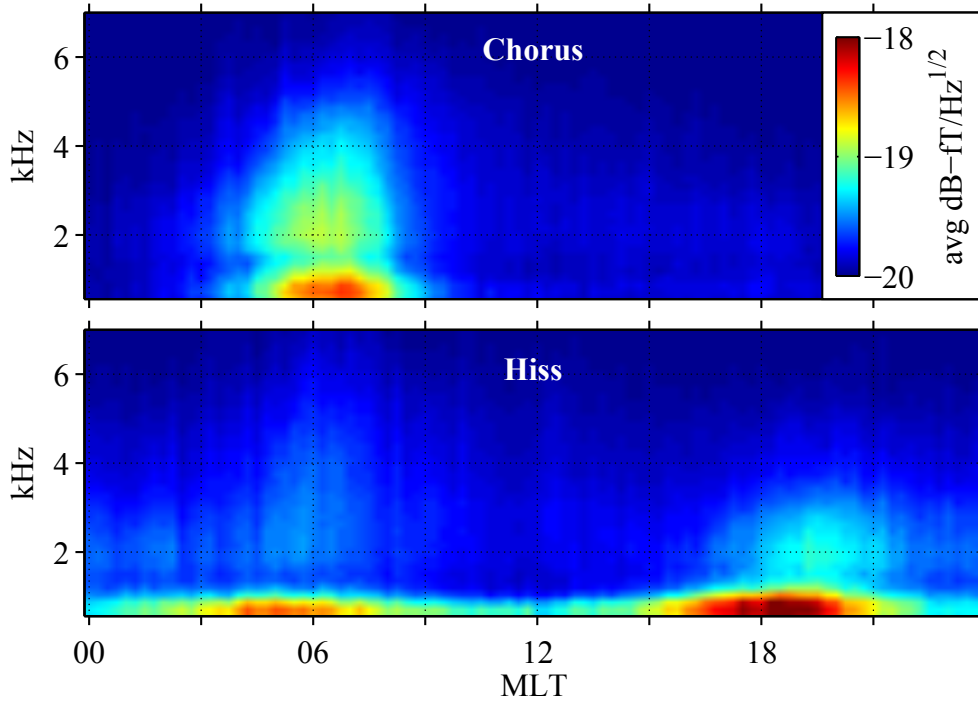


Figure 5.8: Cumulative spectrograms for chorus and hiss computed over the entire 10-year data set. Chorus is observed exclusively in the dawn sector. Hiss is observed at all local times, with peaks near dawn and dusk. Additional higher-frequency structure for hiss is observed in the dusk sector.

artifact of magnetospheric or subionospheric multipath of the original chorus emission. In Chapter 3, we examined only one year of data, 2003, completely by hand. The similarity then of the automated results from this study to the manual results from Chapter 3 are an excellent verification of the automated algorithm (though it should be noted that the same human trainer was used for manual emission identification in both studies, and there may be small systematic biases).

Consistent with other ground studies of chorus [[Storey, 1953](#); [Allcock, 1957](#); [Pope, 1957, 1960](#)] and hiss [e.g., [Laaspere et al., 1964](#)] at similar geomagnetic latitudes, Figure 5.8 shows that chorus is essentially restricted to the dawn sector at Palmer at frequencies up to ~ 6 kHz, while hiss appears at all local times below ~ 1 kHz, peaking in occurrence in the dawn and dusk sectors. A component of hiss is also seen up to ~ 4 kHz in the dusk sector between 16 and 22 MLT [[Vershinin, 1970](#); [Carpenter](#)

et al., 1975; *Hayakawa et al.*, 1988]. In Chapter 3, we hypothesized that the observed dawn hiss may be partially caused by chorus [*Santolik et al.*, 2006; *Bortnik et al.*, 2008] while the observed dusk hiss may be partially caused by terrestrial lightning [*Sonwalkar and Inan*, 1989; *Draganov et al.*, 1992; *Green et al.*, 2005; *Meredith et al.*, 2006].

We also break chorus and hiss occurrence down into a count of average number of emissions per day with a monthly cadence over the course of the entire data set. These occurrence rates are shown in Figure 5.9 (top) along with monthly average K_p and AE indices (middle) and the 10.7-cm solar radio flux from Penticton, British Columbia, Canada (bottom). Two main trends can be seen in the occurrence rates in Figure 5.9 for both chorus and hiss. First, there is a variation in emission occurrence with year, generally declining from 2000 through 2010 with the exception of 2003, a particularly disturbed year. This corresponds to the decline of solar cycle 23 (as indicated by the decline in 10.7-cm radio flux) and the monthly average K_p and AE values over that range, consistent with the known control of chorus and hiss by geomagnetic activity [e.g., *Storey*, 1953; *Laaspere et al.*, 1964; *Meredith et al.*, 2001, 2004]. Second, there is a variation in emission occurrence with season, generally peaking in austral winter (June, July and August) and reaching a minimum in austral summer (November, December, January) due to variations in ionospheric density and absorption that result from seasonal variations in solar illumination [e.g., *Helliwell*, 1965, Sec. 3.8-3.10]. The correlation of geomagnetic activity and, correspondingly, emission occurrence with 10.7-cm radio flux is very weak, and the plot of 10.7-cm radio flux is simply meant to illustrate the phase of the solar cycle.

5.2.2 Yearly and Monthly Variation

The solar-cyclical and seasonal trends of emission occurrence can be explored in more detail by focusing individually on the yearly and monthly variation of emissions. Figure 5.10 shows in the top panels histograms of chorus and hiss occurrence versus year averaged over all months (left) and occurrence versus month averaged over all years (right). The bottom panels show the K_p and AE indices averaged over the

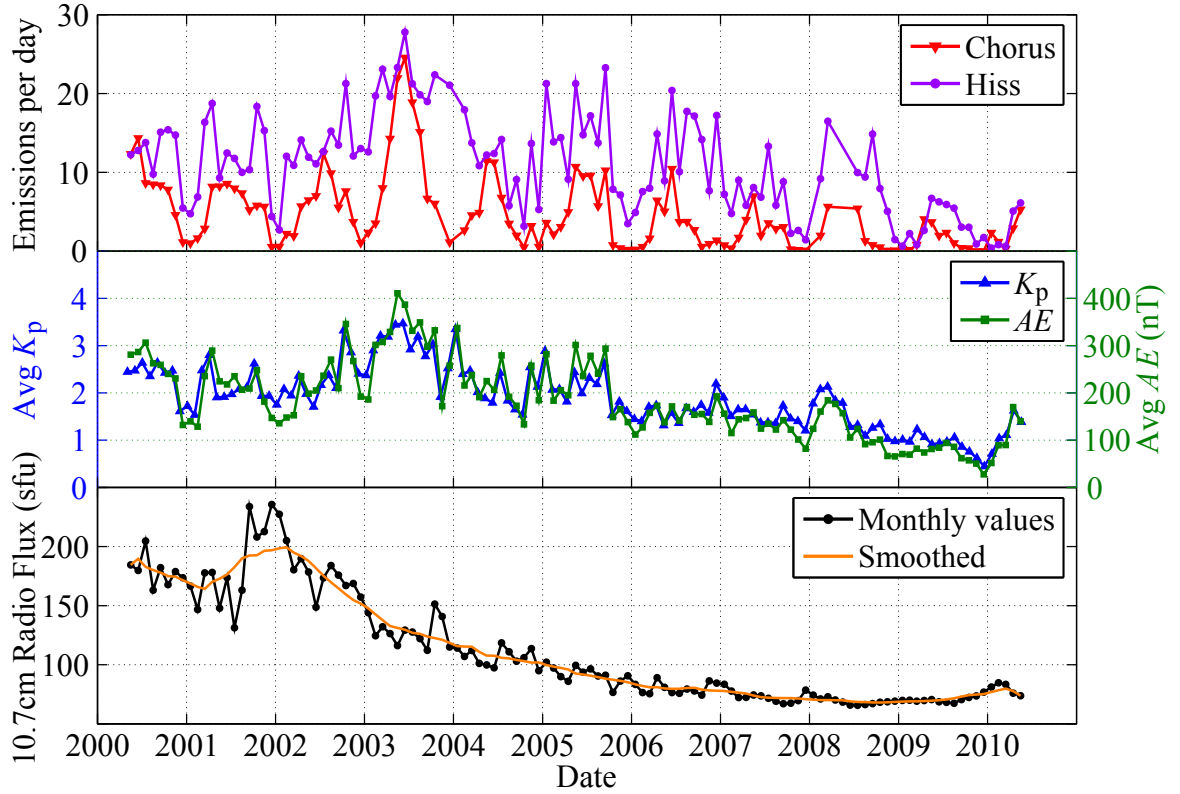


Figure 5.9: (Top) Chorus and hiss occurrence rate, (middle) average K_p and AE indices and (bottom) solar 10.7-cm radio flux for the entire data set, plotted with a monthly cadence. The 12-month smoothed average of the 10.7-cm radio flux is also plotted as an orange line. Chorus and hiss occurrence is well-correlated with geomagnetic activity in a given month, though neither emission occurrence nor geomagnetic activity is particularly well-correlated with radio flux. In the plot of emission occurrence, months with fewer than 12 full days of data (fewer than 1152 synoptic epochs) have been discarded.

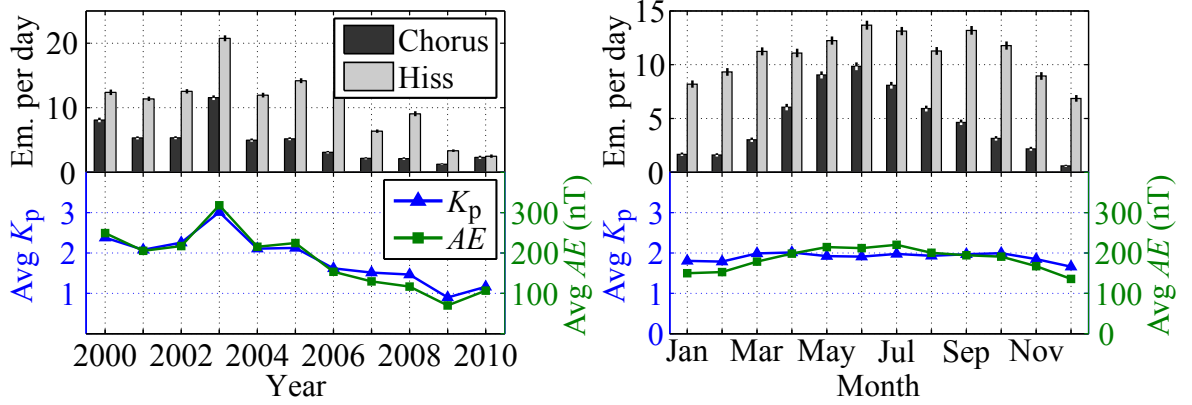


Figure 5.10: (Left) Histogram of chorus and hiss occurrence rate by year (top) and average K_p and AE indices (bottom). The chorus and hiss occurrence rates naturally follow the average K_p and AE in a given year. (Right) Histogram of chorus and hiss occurrence by month (top) and average K_p and AE indices (bottom). The seasonal variation of hiss is at least partially affected by the mild seasonal variation of geomagnetic activity, while the seasonal variation of chorus is primarily dependent on the seasonal variations of ionospheric absorption due to changing solar illumination. Error bars shown are 95% confidence intervals.

same periods. Note that we have only averaged over synoptic epochs for which we have Palmer data from May 2000 through May 2010, so the 2000 and 2010 averages are only over partial years.

The yearly occurrence rates shown in the left panels of Figure 5.10 show a strong correlation with the average K_p and AE values for a given year, indicating strong dependence for both emissions on the geomagnetic disturbance level. The general trend of decreasing occurrence with increasing year is seen, consistent with the decline of K_p and AE in later years coinciding with the waning of solar cycle 23. The obvious exception is 2003, which saw significantly more disturbed geomagnetic conditions than surrounding years. This increased level of geomagnetic disturbance corresponds to a doubling of chorus occurrence in this year versus 2002 and 2004 and a near-doubling in hiss occurrence versus those same years.

The decline of emission occurrence frequency with waning solar cycle is in contrast to the results of *Smith et al.* [2010], who saw no obvious correlation of average receiver amplitude with sunspot number at the higher-latitude Halley Station ($L=4.5$, 61.8°S

invariant latitude). The lack of correlation observed by [Smith et al. \[2010\]](#) may have been due to a variety of factors, including (1) the poor correlation of sunspot number with geomagnetic activity, (2) the corrupting influence of terrestrial lightning in their data, (3) the fact that Halley is on the Antarctic coast and therefore emissions propagating in the Earth-ionosphere waveguide from the Antarctic continent suffer greater attenuation over the Antarctic ice than do emissions observed at Palmer, which primarily propagate over seawater, or (4) simply the fact that Halley is located at a significantly higher L shell than Palmer and tends to observe a somewhat different set of emissions.

The monthly occurrence rates shown in the right panels of Figure 5.10 show a very different trend than the yearly occurrence rates. Here, we see a slight seasonal variation of geomagnetic disturbance levels, generally weaker during austral summer and stronger during austral winter [[Berthelier, 1976](#)], with slight peaks during the equinoxes [[Russell and McPherron, 1973](#)]. However, the hiss and especially chorus occurrence rates show a very strong seasonal variation which is disproportionately greater than would be expected from the seasonal variation in geomagnetic activity alone (though there is a slight peak in hiss occurrence during the equinoxes).

The large seasonal variation in chorus and hiss occurrence is the result of one of the most debilitating factors for interpreting ground-based measurements of magnetospheric phenomena, namely variations in ionospheric absorption. Daytime absorption rates for trans-ionospheric propagation can be tens of dB higher than nighttime rates at 50° invariant latitude [[Helliwell, 1965](#), Fig. 3-35], and the signal strength is further reduced during the day due to increased absorption in the Earth-ionosphere waveguide.

To illustrate the effect of ionospheric absorption on received chorus wave power, Figure 5.11 shows cumulative spectrograms of chorus on a monthly basis, from January to December, averaged over the full 10-year data set. The dawn day/night terminator is marked with a golden dashed line on the left of each image, and the dusk day/night terminator is marked with a blue dashed line on the right of each image. As the onset of daylight shifts to later local times from January to June, the region of observed chorus emerges between 04 and 10 MLT. Then as the onset

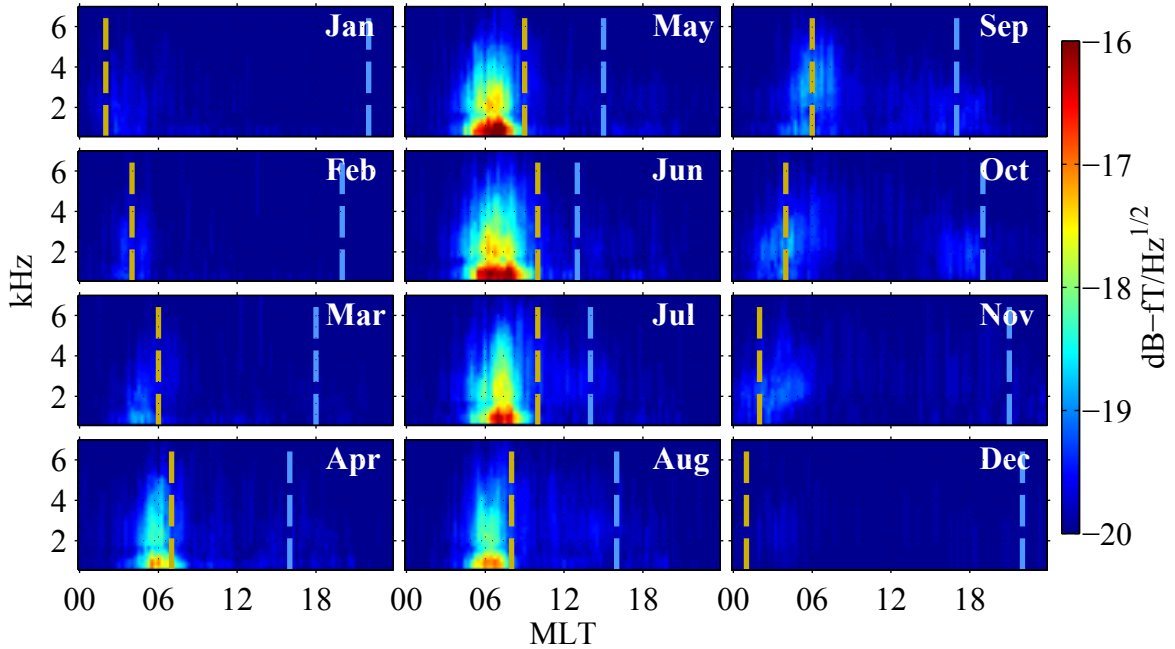


Figure 5.11: Cumulative spectrograms of chorus by month. The dawn terminator is shown as the golden dashed line on the left of each image, and the dusk terminator is shown as the blue dashed line on the right of each image. The region between the two terminator lines is sunlit, and the region beyond either line is in darkness. This progression shows that chorus is only observable during local night.

of daylight moves to earlier local times from June through December, the region of observed chorus fades away. This monthly progression clearly shows that, due to increased ionospheric attenuation during daytime, chorus is only observable during local night, the times of which change dramatically throughout the year at Palmer’s high geographic latitude (64.05°S). The “preferred” interval for observing chorus at Palmer is somewhere between 04 and 13 MLT although it is only observed between 04 and 10 MLT because the hours between 10 and 13 MLT are always sunlit.

Results are similar for hiss, as shown in Figure 5.12, except that hiss is often seen at lower amplitudes below 1 kHz, even when Palmer is in daylight (as suggested by the band below 1 kHz in the lower panel of Figure 5.8, even at local noon). This is probably the result of ionospheric absorption decreasing with decreasing frequency [e.g., [Helliwell, 1965](#), Fig. 3-35]. The hiss amplitudes below 1 kHz at dawn and dusk

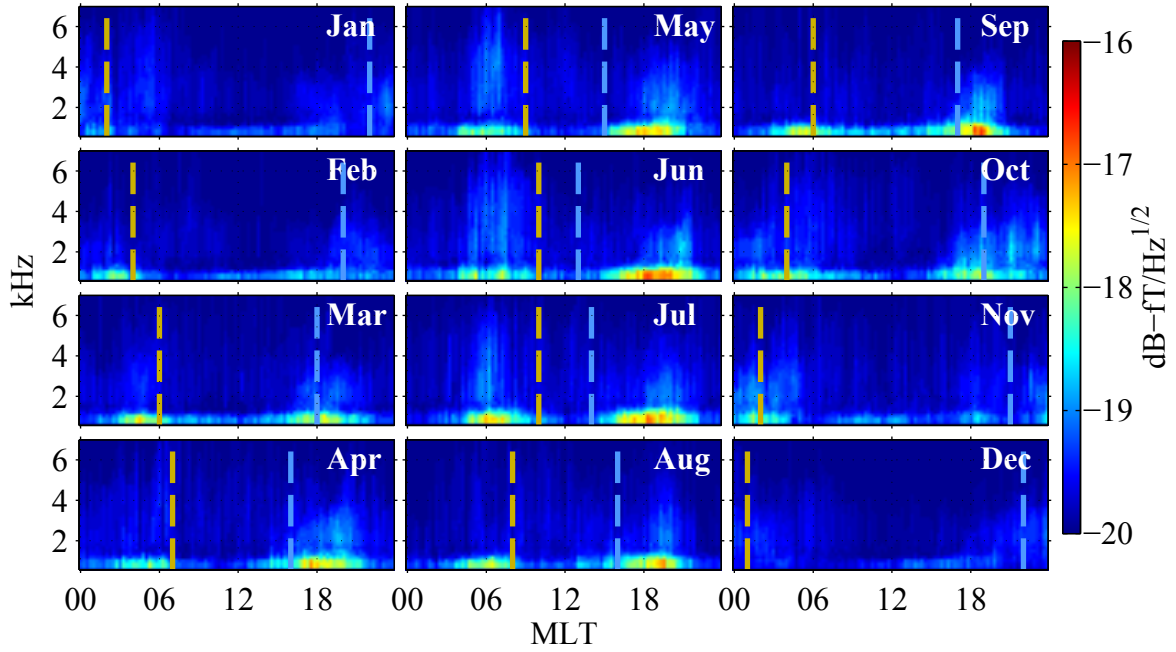


Figure 5.12: The same as Figure 5.11, but for hiss. The effect of the terminator is still significant, but less dramatic, due to the lower frequencies of hiss compared with chorus.

do however increase when Palmer is in darkness versus when it is sunlit. These results are consistent with those of *Smith et al.* [2010], who found a significantly stronger influence of the day/night terminator for emissions at ~ 3 kHz than for those at ~ 1 kHz, although they did not systematically differentiate between chorus and hiss.

5.3 Summary

An algorithm for automatically detecting and differentiating between chorus and hiss on data from ground-based ELF/VLF wave receivers has been developed. The algorithm operates on 10-sec broadband data records, sampled at 100 kHz. Data is first cleaned of sferics and hum. Next, events are detected using empirical methods and fed to a pair of previously-trained neural networks which discard noise events and categorize remaining events as either chorus or hiss.

All aspects of the algorithm are automatic and require no operator intervention

with the exception of the initial training of the neural network. This initial training is accomplished by having a human trainer manually create a training set by categorizing a subset of detected events as either noise, chorus or hiss. The neural networks are then trained using this training set. The noise neural network used in this study is capable of correctly differentiating between noise and emissions for 91.9% of the 10,013 events in the noise neural network training set. The emission neural network is capable of correctly differentiating between chorus and hiss for 84.0% of the 2453 events in the emission neural training set. Excluding the one-time assembly of the neural network training set by the trainer, the algorithm runs at 350x real time on a single modern 8-core computer and could easily run at better than real time on more conservative hardware.

The algorithm was run on 10 years of broadband data from Palmer Station, Antarctica, from May 2000 through May 2010. Based on the output of the automated detector, we show that chorus is primarily observed in the dawn sector, at frequencies from 400 Hz to ~ 6 kHz, while hiss is observed below 1 kHz at all local times and up to ~ 4 kHz in the dusk sector. The average occurrence rates of chorus and hiss in a given year, over the course of a solar cycle, are strongly dependent on the average geomagnetic disturbance levels in that year.

Over the course of a single year, chorus occurrence in particular varies significantly from June to December, as a result of the longer daylight hours and resulting increased ionospheric absorption during austral summer versus austral winter. Hiss occurrence varies in this same manner for the same reason although the difference is less dramatic due to the lower frequencies of hiss and resulting decreased ionospheric absorption. Although the perils of high ionospheric absorption in interpreting ground-based ELF/VLF wave data have long been known, Figure 5.11 starkly illustrates its effects and shows that caution must be used when comparing data from summer months to winter months.

Chapter 6

Summary and Suggestions for Future Work

6.1 Summary of Major Results

Palmer Station’s unique combination of low-noise environment, location at middle geomagnetic latitudes, and long uninterrupted history of measurements make it an excellent vantage point from which to explore the statistics of mid-latitude chorus and hiss emissions. These emissions play critical roles in the source and loss mechanisms for energetic electrons in the Earth’s radiation belts, which in turn pose a hazard to satellites and astronauts in near-Earth space.

In Chapter 3, we explored the general trends of chorus and hiss emissions observed at Palmer from January through October, 2003. At Palmer, both chorus and hiss are observed on more than 50% of days during solar maximum. We showed that when hiss is observed with chorus, they appear together exclusively in the dawn sector, which is consistent with the possibility that chorus is a source of hiss at this MLT. Hiss appears without chorus exclusively in the dusk sector, in which case the hiss frequency spectrum and local time of appearance is consistent with lightning as a source.

In Chapter 4, we investigated in more detail the manner in which chorus emissions propagate from their magnetospheric sources to the ground at Palmer. We primarily

investigated the role of the plasmopause in guiding or refracting the waves. We began with a data-based study of chorus observations at Palmer, coupled with observations of plasmasphere extent using the extreme ultraviolet instrument on board the IMAGE satellite. We combined these two measurements using logistic regression to generate a statistical model of chorus occurrence probability as a function of plasmasphere extent. We determined that the greatest occurrence probability came about when the plasmasphere extent was at $L=2.6$ for chorus frequencies below 1.5 kHz and $L=2.7$ for frequencies above 3 kHz.

The physical mechanism by which the plasmopause controls chorus observations at Palmer was explored in more detail via modeling. We began by modeling chorus propagation and Landau damping in the magnetosphere via reverse raytracing, using the new Stanford VLF 3D raytracer. Rays were launched from the vicinity of Palmer and their crossings of the magnetospheric equator outside the plasmopause were noted. Propagation loss was included via Landau damping in the magnetosphere, and attenuation in the Earth-ionosphere waveguide was included using a full wave model. The amplitudes of the wave energy represented by the rays at their equatorial crossings were binned by radial extent and wavenormal, and the sum of all amplitude bins defined the chorus availability factor, or CHAF. CHAF is a proxy measurement of the likelihood of observing chorus at Palmer. By varying the extent of the plasmopause in the model, we were able to obtain a plot of CHAF versus plasmasphere extent, analogous to the plot of measured chorus occurrence probability versus observed plasmasphere extent.

The plots of modeled CHAF and observed chorus occurrence probability agreed well with each other, showing a single maximum of occurrence within $0.5 R_E$ of each other for frequencies below 1.5 kHz and within $0.2 R_E$ for frequencies above 3 kHz. We explained that the likely reason that a single peak exists, as opposed to a monotonically increasing likelihood of chorus occurrence for decreasing plasmasphere extent, is the result of a balance between two propagation modes: the direct propagation from the chorus source to the ground outside the plasmasphere and propagation to the ground via one or more magnetospheric reflections (MRs) into the plasmasphere. For large plasmasphere extents, the plasmopause appears as a barrier, and Palmer's

low L shell is shielded from waves outside the plasmasphere. As the plasmopause moves to lower L shells, Palmer becomes accessible by both the direct path and the MR path. Finally, as the plasmopause moves still lower, chorus on the MR path must propagate for an increased amount of time outside the plasmasphere before it is able to MR into the plasmasphere. Such propagation results in increased damping due to the greater energetic fluxes outside the plasmasphere and the subsequent extinguishing of the MR path without any appreciable effect on the direct path.

In addition, the fact that the non-ducted model of chorus propagation reproduces the results of the measurements strongly suggests that the observed chorus at mid latitudes is non-ducted. This finding is in contrast to a long-held belief that all ELF/VLF wave observations on the ground are made possible by virtue of magnetospheric ducts, guiding these waves from their source to the ground as discussed in Section 1.2.2. This conclusion is further strengthened by the fact that the observed peak in chorus occurrence appears when the plasmopause is at $L=2.6$, slightly higher than Palmer’s L shell at $L=2.4$. If ducts were responsible for bringing chorus to the ground, we would expect to see a peak of chorus occurrence when the plasmopause was at or slightly below Palmer’s L shell, since in that case, ducts would be able to form at Palmer’s L shell and bring chorus waves to the ionosphere directly above Palmer. Thus, we conclude from this study that the majority of chorus waves observed at Palmer are likely non-ducted.

Inspired by the drudgery of manually scanning through broadband spectrograms in order to compile statistics for Chapters 3 and 4, we took a step back from purely magnetospheric studies in Chapter 5 to focus on automating the generation of statistical databases of magnetospheric emissions from raw data collected at Palmer. We developed a novel method of automatically detecting and categorizing emissions in broadband data. The procedure consists of three broad steps: (a) cleaning of the source broadband data of common sources of interference, (b) detection of “events” and characterization of their properties, and (c) automatic categorization of detected events as chorus, hiss and noise, using a sequential pair of complementary neural networks.

In support of step (a), we discussed the development of a method of detecting and

removing sferics from the broadband data using an autoregressive model of the underlying signal. Proper implementation of the sferic removal allows most sferics to be removed without significantly altering the spectrum of the underlying emissions. Step (b) required us to determine a series of relevant scalar characteristics for each event which would help to separate the events into the categories of chorus, hiss and noise. In addition to characteristics about the frequency, time and amplitude of the event, we also included characteristics about the “burstiness” of the event and its dominant slope. Finally, step (c) utilizes a pair of neural networks which are trained on a subset of detected events that have been manually characterized by a human trainer. The result is a fully automated emission detection and characterization system where the only manual step is the one-time construction of the training set.

Using this system, we created a database of spectrally-categorized chorus and hiss emissions observed at Palmer Station over 10 years of observations, nearly an entire 11-year solar cycle. This database was used to highlight various aspects of chorus and hiss occurrence at Palmer. We showed that in a given year, the occurrence rates of chorus and hiss are very well correlated with the average level of geomagnetic activity in that year, as measured by the K_p and AE indices. We also showed that, in a given month, emission occurrence, particularly of chorus, is far more dependent on the seasonal variation of the day-night terminator than on the average geomagnetic activity in that month. This dependence is the result of the fact that the absorption of waves in the ionosphere is greatest during local daytime, when the ionospheric densities are highest; as a result, chorus emissions are simply not visible during local day. This increased daytime absorption makes measurements of the seasonal variation of chorus occurrence in the magnetosphere impossible from the ground. The variation of hiss occurrence with the day-night terminator is similar, though less pronounced, as a result of the fact that hiss frequencies are usually lower than chorus frequencies and lower frequencies suffer less trans-ionospheric attenuation.

6.2 Suggestions for Future Work

Future researchers may wish to expand on the topics covered in this thesis. In particular, the studies discussed in Chapters 3 and 4 were limited by the fact that, at the time they were carried out, the automated emission detector discussed in Chapter 5 was not yet developed. With the introduction of the automated emission detector, the most time-consuming and monotonous aspect of these studies, namely collecting chorus and hiss statistics, may be eliminated. It would thus be possible for the researcher to focus on the implications of the statistics, instead of getting caught up in collecting them.

Researchers may first be interested in expanding the techniques of Chapter 4, which dealt with the propagation of chorus from its magnetospheric source to the ground, to hiss. Hiss is complementary to chorus, with a source believed also to lie in the equatorial region. Because hiss is generated inside the plasmasphere, it is not immediately clear how the extent of the plasmopause would affect the propagation of hiss; more likely, its main effect will be in dictating the boundary of the hiss source region. The observational aspect of the study could be the same as in Chapter 4, with the measurements of the plasmopause being collected in the same way from IMAGE EUV data and statistics of hiss emissions instead of chorus being gathered from Palmer data. The primary difference in the modeling aspect would lie in the fact that hiss is sourced within the plasmasphere, whereas chorus is sourced without; otherwise, all aspects of the model would be similar. As was noted earlier in Section 4.4.4, researchers should use caution when implementing Landau damping using measured hot electron fluxes in the plasmasphere, as the fluxes used in our model from *Bell et al.* [2002] were measured only during quiet and moderately disturbed periods and are not MLT-dependent. A more rigorous study of Landau damping of hiss within the plasmasphere would benefit from a more extensive model of plasmaspheric particle fluxes.

The power of the automated emission detector discussed in Chapter 5 is by no means limited to Palmer data. Though the detector is tuned to the calibration, emission and noise profiles at Palmer, the detector could be easily adapted to other

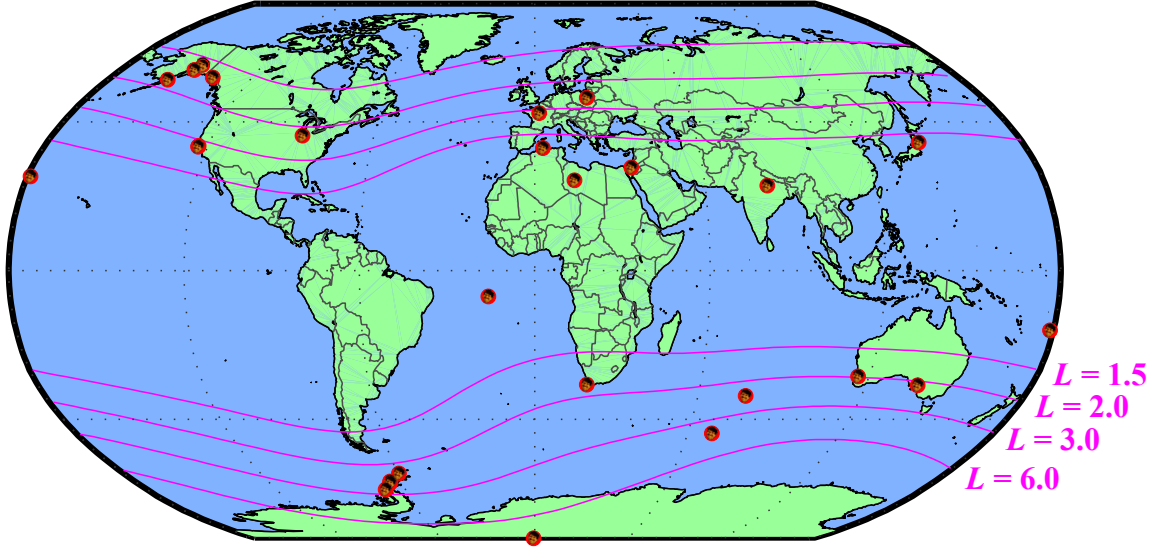


Figure 6.1: The Stanford VLF group operates and collaborates with dozens of broadband ELF/VLF receivers, indicated by red dots, worldwide.

stations and was designed with this adaptability in mind. The Stanford VLF group operates and collaborates with operators of over two dozen worldwide ELF/VLF receiver sites as shown in Figure 6.1. Although few of these sites have the extensive historical data of Palmer, the automated emission detector could be used for shorter studies at select sites at different latitudes to determine characteristics of emissions across a range of L shells. High latitude stations in particular are expected to show a greater variety of emissions, including auroral chorus and hiss emissions, the former of which, in contrast to mid-latitude chorus, appears during quiet as well as disturbed periods [Spasojevic and Inan, 2010].

Additionally, certain locations have clusters of broadband receivers, such as the Antarctic peninsula near Palmer, and southern Alaska. Multi-station measurements of similar emissions at these sites could give insight into the specific ionospheric exit points of chorus and hiss emissions. Such studies have been done previously for chorus on a limited scale by Golkowski and Inan [2008] using receivers in Alaska. Future studies could compare exit points of both chorus and hiss during less disturbed and more disturbed geomagnetic conditions, using the automated emission detector to find periods of emissions during these periods.

The automated emission detector is also not limited to measurements at ground stations. In situ satellite measurements could also benefit from an application of the automated emission detector either in a post-processing stage or implemented as on-board processing (the latter of which would be more difficult due to the need to manually train the neural networks before implementation). On-board detection of chorus and hiss would be a particularly exciting application. Satellite telemetry is usually limited, and schedules of when to record and save broadband data generally must be agreed upon beforehand. Use of an automated emission detector would allow a satellite to only save broadband data when emissions were present, allowing the satellite to avoid wasting telemetry on uninteresting data.

Although the roles of chorus and lightning in the generation of plasmaspheric hiss were superficially investigated in Chapter 3, recently developed tools would allow the role of lightning in generating hiss to be explored at a much deeper level. Specifically, the recent work on global lightning detection by *Said et al.* [2010] has recently been implemented as a worldwide lightning detection network. Correlating individual lightning-producing storm cells with worldwide ground observations of hiss would provide convincing evidence for the extent to which lightning plays a role in hiss generation to a level of detail not previously explored.

Finally, although the automated emission detector is tuned to detect chorus and hiss emissions and reject all other events as noise, it would be straightforward to allow magnetospheric whistlers, another fairly prevalent whistler-mode emission, to be detected as well. Because the originating emission that gives rise to whistlers is an impulse, whistlers are an excellent diagnostic tool for determining properties of the magnetospheric medium through which they propagate [e.g., *Park, 1972*], and methods are currently being developed to automatically detect and process them [*Lichtenberger et al., 2008*]. Use of the automated detector system may be valuable as an alternate or complementary method of detecting whistlers for this purpose.

The intent of the work in this thesis is to provide a means of using ground observations to further our understanding of chorus and hiss, rather than an end. We consider the new perspective shown in Chapter 4 of chorus emissions' propagation from their magnetospheric source to the ground to be fundamental to interpreting

ground observations of chorus, and we expect that the automated emission detector of Chapter 5 will go a long way towards making statistical studies of chorus and hiss far easier to perform. We look forward to seeing the results of studies that use these tools to continue to advance our fundamental understanding of magnetospheric whistler-mode emissions.

Appendix A

Statistics for Binomial-Distributed Data

With their ability to record and save large volumes of data, ground receivers are particularly well-suited for statistical studies of chorus and hiss. The studies presented throughout this thesis share a consistent measurement format, with 10-second broadband samples from Palmer Station sampled every fifteen minutes. In each sample of data, the recorded data is either true (an emission did occur) or false (an emission did not occur). Thus, in a given measurement period, the probability of a sample being “true” is Bernoulli-distributed with mean p and variance $p(1 - p)$. If n independent samples are made, the resulting number of true values is binomial distributed with mean np and variance $np(1 - p)$.

In order to understand the statistical analyses presented in this thesis, we discuss in this section some useful statistical methods for binomial-distributed data. Unless otherwise noted, more details for the statistical concepts in this section may be found in [Navidi \[2006\]](#), an excellent introduction to statistical methods for engineering and scientific applications.

A.1 The Central Limit Theorem

Let X_1, \dots, X_n be a series of n random samples from a population with mean μ and variance σ^2 . The central limit theorem (CLT) states that, given a measurement of the sample mean, \hat{p} , with a sufficient number of random samples ($n \gtrsim 30$), as

$$\hat{p} = \frac{X_1 + \dots + X_n}{n}, \quad (\text{A.1})$$

then the observed sample mean is distributed normally as

$$\hat{p} \sim \mathcal{N}\left(\mu, \frac{\sigma^2}{n}\right). \quad (\text{A.2})$$

The power of the CLT lies in its ability to help us bound the mean of the true population with a certain confidence level based on our observations of only a subset of the population.

A.2 The Agresti-Coull Confidence Interval

Inherent in the implementation of the CLT in determining confidence intervals is the z -score, given by

$$z = \frac{\hat{p} - \mu_0}{\sigma_0}, \quad (\text{A.3})$$

where μ_0 is the population mean and σ_0 is the population standard deviation. z under a normal distribution with mean $\mu=0$ and variance $\sigma^2=1$ (also known as a “standard normal population,” written $\mathcal{N}(0, 1)$) is equivalent to \hat{p} measured under the normal distribution with mean μ_0 and variance σ_0^2 . That is, the probability of measuring a value less than or equal to \hat{p} from our sample population is equal to the probability of measuring a value less than or equal to z from the standard normal population. This is illustrated in Figure A.1, which shows that if a z -score of $z=-1$ is computed from a value \hat{p} , the probability of sampling a number less than or equal to \hat{p} from our sample distribution is equal to the area to the left of z under the standard normal population, or 0.16. This is equivalent to the value of the cumulative distribution

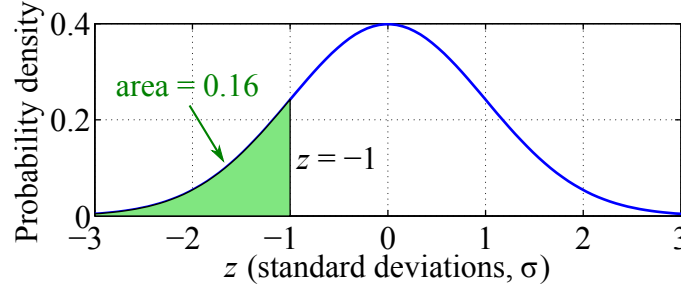


Figure A.1: The z -score (z) is the independent variable of a normal probability distribution function with mean $\mu=0$ and variance $\sigma^2=1$. The probability of sampling a number less than or equal to z is equal to the area under the normal curve to the left of z .

function (CDF) for the standard normal population at z . This can be determined with the MATLAB command `normcdf(-1)`, which yields a value of 0.16.

Confidence intervals are typically defined with respect to a certain percentage. For example, if we wish to say that the true mean of a sample population, μ , lies in the range $A \pm B$ with 95% confidence, this is equivalent to saying that there is no more than a 5% chance that, given our sample population, either $\mu < A - B$ or $\mu > A + B$.

Traditionally, a $100(1 - \alpha)\%$ confidence interval is defined with respect to the n measurements X_1, \dots, X_n and the z -score as

$$\hat{p} \pm z_{\alpha/2} \hat{\sigma} / \sqrt{n}, \quad (\text{A.4})$$

where $z_{\alpha/2}$ is the value of z for which the CDF of the standard normal population is equal to $1 - \alpha/2$ and $\hat{\sigma}$ is the sample standard deviation. In MATLAB, $z_{\alpha/2}$ is computed as `norminv(1 - $\alpha/2$)`. For example, for a 95% confidence interval, we set $\alpha=0.05$, and $z_{0.025}=1.96$.

However, when dealing with Bernoulli distributions, recent research [[Agresti and Coull, 1998](#)] has shown that a modified version of (A.4) is usually more accurate. Given X successes in n independent Bernoulli samples with success probability p (so X is binomial distributed as $X \sim \text{Bin}(n, p)$), define $\tilde{n} = n + 4$ and $\tilde{p} = (X + 2)/\tilde{n}$.

Then a $100(1 - \alpha)\%$ confidence interval for p is

$$\tilde{p} \pm z_{\alpha/2} \sqrt{\frac{\tilde{p}(1 - \tilde{p})}{\tilde{n}}}. \quad (\text{A.5})$$

This is the Agresti-Coull confidence interval and is used for all confidence intervals, including histogram error bars, in this thesis.

A.3 Hypothesis Testing for Sample Means

Hypothesis tests follow directly from confidence intervals. Specifically, we focus on the probability that the true population success probability p (say, the probability of observing chorus) in n independent samples (or synoptic epochs) is greater than a certain value, p_0 . Define the null hypothesis, H_0 , as the probability that p is less than or equal to p_0 , and the alternate hypothesis, H_1 , that it is not:

$$H_0 : p \leq p_0 \quad \text{vs.} \quad H_1 : p > p_0. \quad (\text{A.6})$$

Given a sufficiently large sample size, via the central limit theorem, the sample proportion is given by (A.2) as

$$\hat{p} \sim \mathcal{N}\left(p, \frac{p(1 - p)}{n}\right) \quad (\text{A.7})$$

where we have used the fact that the binomial distribution has mean $\mu = np$ and variance $\sigma^2 = np(1 - p)$. Usually in magnetospheric data, we have made n measurements and found a measured emission occurrence probability, \hat{p} . We wish to state that the true emission occurrence probability, p , is greater than or equal to some unknown value, p_0 with, say, 95% confidence. We note that \hat{p} is distributed as in (A.7) with mean p_0 and variance $p_0(1 - p_0)/n$. We find the z -score by substituting these values into (A.3) to get

$$z = \frac{\hat{p} - p_0}{\sqrt{p_0(1 - p_0)/n}}. \quad (\text{A.8})$$

This can be rearranged with respect to p_0 as

$$p_0 = \frac{2n\hat{p} + z^2 \pm z\sqrt{-4n\hat{p}^2 + 4n\hat{p} + z^2}}{2z^2 + 2n} \quad (\text{A.9})$$

where the choice of negative sign in the quadratic formula implies a positive value of z , as in our case shown next.

We can reject the null hypothesis at the 5% level when the probability that $\hat{p} > p_0$ is less than 5% when $p \leq p_0$, i.e., the observed mean is greater than p_0 while the true mean is less than p_0 . This is equivalent to setting $z = \text{norminv}(0.95) = 1.64$. We can then say with 95% confidence that the true mean probability of observing emissions, p , is greater than or equal to p_0 , as determined with (A.9), given n samples with a sample mean of \hat{p} .

If the null hypothesis were of the alternate form,

$$H_0 : p \geq p_0 \quad \text{vs.} \quad H_1 : p < p_0, \quad (\text{A.10})$$

which is equivalent to (A.6) but with the inequalities reversed, then the process would be the same, except that we would set $z = \text{norminv}(0.05) = -1.64$, and the negative sign in (A.9) would indicate a negative value for z .

A.4 Logistic Multiple Regression

Often, collections of binary true/false data are collected in the context of a potential driving force of which the sample mean is a function. For example, in Chapter 4, we collect binary samples of chorus and attempt to determine how the probability of chorus occurrence depends on plasmasphere extent. The traditional method of showing the dependence of the sample mean, μ , on the independent (generally continuous) variable, A , is via a histogram, where bar height is equal to the average of μ in the A -range of the given bar. However, histograms suffer from two problems: first, because of their noisy and discontinuous sampling, it is difficult to make a prediction for μ given a single value of A . Second, they are not useful when examining the

dependence of μ on more than one dependent variable, due to the need to reduce the statistical counts in each bin as the bin limits become more specific.

If it is reasonable to assume that μ depends in a relatively simple way on A , then logistic regression [*Chatterjee and Hadi, 2006*, Ch. 12], a subset of the more general field of regression analysis, can be used in the place of the histogram. Under regression analysis, a linear combination of parameters is sought to form an estimate of μ , the probability of event occurrence. Because linear models have, in general, unbounded values, a *logit* response function is used for μ , defining the output of the linear model, Y , as

$$Y = \log \left(\frac{\mu}{1 - \mu} \right), \quad (\text{A.11})$$

and conversely,

$$\mu = \frac{e^Y}{1 + e^Y}. \quad (\text{A.12})$$

This transforms the bounded parameter $\mu \in [0, 1]$ to the unbounded parameter $Y \in (-\infty, \infty)$. Given m distinct independent variables, Y is modeled as

$$Y = X\beta = \begin{bmatrix} 1, & x_1, & x_2, & \dots, & x_m \end{bmatrix} \begin{bmatrix} \beta_0 \\ \beta_1 \\ \beta_2 \\ \vdots \\ \beta_m \end{bmatrix}, \quad (\text{A.13})$$

where X is a row vector of predictors, formed by transformations of the independent variables (e.g., $x_1 = A$, $x_2 = A^2$, etc.), and β is a column vector of coefficient estimates. If μ is expected to be a function of more than one independent variable (say, A and B), then X can be composed of combinations of both independent variables (e.g., $x_1 = A$, $x_2 = B$, $x_3 = AB$, $x_4 = A^2B$, etc.). There is no restriction on the form of the terms of X , and more complicated functions such as $\log(A)$ could be included as appropriate. In practice, the logistic regression fitting procedure is accomplished computationally, and MATLAB contains an excellent regression package via the `glmval` and `glmfit` functions in the statistics toolbox.

As one might infer, a large part of the difficulty in choosing a reasonable composition of X is knowing when to stop adding terms. Determining the appropriate predictors for X is a science unto itself, and methods of choosing terms to exclude are largely heuristic. One such method makes use of a concept known as the Bayesian Information Criterion (BIC). BIC is a figure of merit for a model, given by

$$\text{BIC} = -2(\text{Model Log-Likelihood}) + m \log n, \quad (\text{A.14})$$

where m is the number of terms in X and n is the number of samples of binary data used in the model fit. Lower BIC scores are better. The log-likelihood for binomial-distributed data is given by

$$\sum_k \log(\text{Bernoulli PDF}(b_k)) \quad (\text{A.15})$$

where b_k are individual binary samples (1 or 0), and the Bernoulli PDF has mean given by the fitted mean, $\hat{\mu}$, determined via logistic regression.

The BIC score of a given model is reduced for better fits and penalized for each additional term. Penalizing models with extraneous terms honors the principle of parsimony, which says that simpler models are preferred to more complex ones; this avoids overfitting the model to the data. The choice of terms which minimizes a model's BIC can be considered optimal for that model. The MATLAB `glmfit` function also determines P -values for each term in the model; term P -values represent the significance level at which one can reject the null hypothesis that that particular term's coefficient is actually zero. For example, a P -value of 0.05 for a given term's coefficient indicates that there is 95% confidence that that term is relevant. Higher P -values (lower confidence) may warrant dropping that term.

A.5 Fishing Expeditions: A Statistical Fallacy

Although the field of statistics has many excellent tools to help scientists organize and make sense of large quantities of information, these same statistical methods can also

be misused to give false conclusions either unintentionally or due to an experimenter's implicit or explicit biases. The inclusion of this section was inspired by an excellent recent article in the Journal of Personality and Social Psychology by [Wagenmakers et al. \[2011\]](#).

It is often the case in scientific measurements that a phenomenon is observed, such as chorus amplitude at Palmer, and the experimenter is not certain of what environmental factors are most likely to predict this phenomenon, such as a choice between the K_p , AE and Dst indices. One approach may be to perform analysis of chorus amplitude with respect to all available variables, and see which one has the greatest correlation, or analogously, the lowest P -value. Here, the P -value is the significance level at which we can reject the null hypothesis that the actual correlation is 0. The process of examining multiple variables and determining a post priori hypothesis from the results is known as exploration, or, colloquially, a “fishing expedition.” There is nothing inherently wrong with fishing expeditions, and they can be very useful in discovering relationships that are difficult to predict from first principles.

Once the most relevant index is determined, say AE , the temptation is to report the associated P -value as the definitive P -value for the correlation between chorus amplitude and AE . However, this approach ignores the fact that the experimenter has used the same data twice: once to determine a new hypothesis and again to test that hypothesis. Such double use of data is contradictory to the scientific method, which states that the hypothesis must be stated before it is tested. To see why such an approach is problematic, consider a case where the probability of misreporting a high correlation for any individual index is 0.05. In this case, the probability that *at least* one of the three correlations is misreported is the inverse of the probability that each correlation is reported correctly or $1 - .95^3 = 0.14$, a value is significantly higher than the probability of misreporting any individual high correlation. This higher probability of error illustrates the fact that conclusions from exploratory studies are not as strong as conclusions from confirmatory studies.

Optimally, once the a new hypothesis is established via an exploratory study, it should be tested using different data in a confirmatory study. Failing that, the fact that the correlation was initially determined in an exploratory fashion should be

explicitly stated. An excellent in-depth article on this subject is available by [Kerr \[1998\]](#).

Appendix B

Notable Emissions at Palmer

This appendix showcases some notable examples of emissions observed at Palmer Station. Beyond chorus and hiss, several interesting classes of magnetospheric ELF/VLF emissions are often seen. Whistlers are certainly the most common emission (more so than chorus or hiss), and their prevalence and often high amplitudes allow them to interact with ambient hot particles. This interaction gives rise to a variety of interesting effects including the triggering of discrete emissions [[Helliwell *et al.*, 1964](#)], triggering of chorus or hiss-like emissions [[Sonwalkar and Inan, 1989](#)], and generation of plasmaspheric hiss due to many overlapping magnetospheric reflections [[Draganov *et al.*, 1992](#)] (see Section 3.3.2 for further discussion of lightning as a source of hiss). In addition to these common emissions, periodic and quasi-periodic discrete emissions [e.g., [Sazhin and Hayakawa, 1994](#), and references therein] are seen more rarely at Palmer. An excellent empirical review of these different emissions can be found in [Helliwell \[1965, Ch. 7\]](#).

B.1 Chorus and Hiss Progression

The synoptic spectrogram, initially discussed in Section 3.1.1, consists of a series of 5-second spectrograms, one per synoptic epoch at 5, 20, 35 and 50 minutes past the hour, stitched together horizontally to form a single pseudo-continuous spectrogram. An example 24-hour synoptic spectrogram is shown in Figure 3.1. The synoptic

spectrogram should not be confused as being a continuous spectrogram; it consists of a series of 5-second snapshots in time.

The synoptic spectrogram is an excellent way to get a sense of the large-scale evolution of electromagnetic activity over the course of several hours. In this section we use the synoptic spectrogram to show the evolution of chorus and hiss emissions over their total duration, which is usually several hours or more. Figure B.1 shows several example chorus emissions during local dawn and Figure B.2 shows example hiss emissions during local dusk. There is considerably more variation seen over individual events than might be expected from the statistically averaged cumulative spectrograms of Figure 5.8. All times are in coordinated universal time (UTC) and all color scales are the same as in Figure B.1a. Note that the time and frequency scales of the plots are not the same.

As seen in Figure B.1, chorus is usually first seen at low frequencies which increase over time, but as Figure B.1c shows this is not always the case. In addition, chorus is often seen in multiple bands, some of which may appear hiss-like with varying degrees of structure; this observation is consistent with chorus as a source of hiss during certain local times (see Section 3.3.1 for further discussion). The termination of chorus is generally gradual, though the amplitude may change abruptly over a 15-minute interval. Different frequency bands often vary in amplitude independently of each other, as can be seen in the middle section of Figure B.1c.

As Figure B.2 shows, hiss also begins at low frequencies, increases in frequency over time, and generally decreases in frequency slightly before terminating [e.g., *Vershinin*, 1970; *Carpenter et al.*, 1975]. Dusk hiss typically appears in only a single frequency band without any simultaneous chorus and is likely sourced at least in part by terrestrial lightning (see Section 3.3.2 for further discussion).

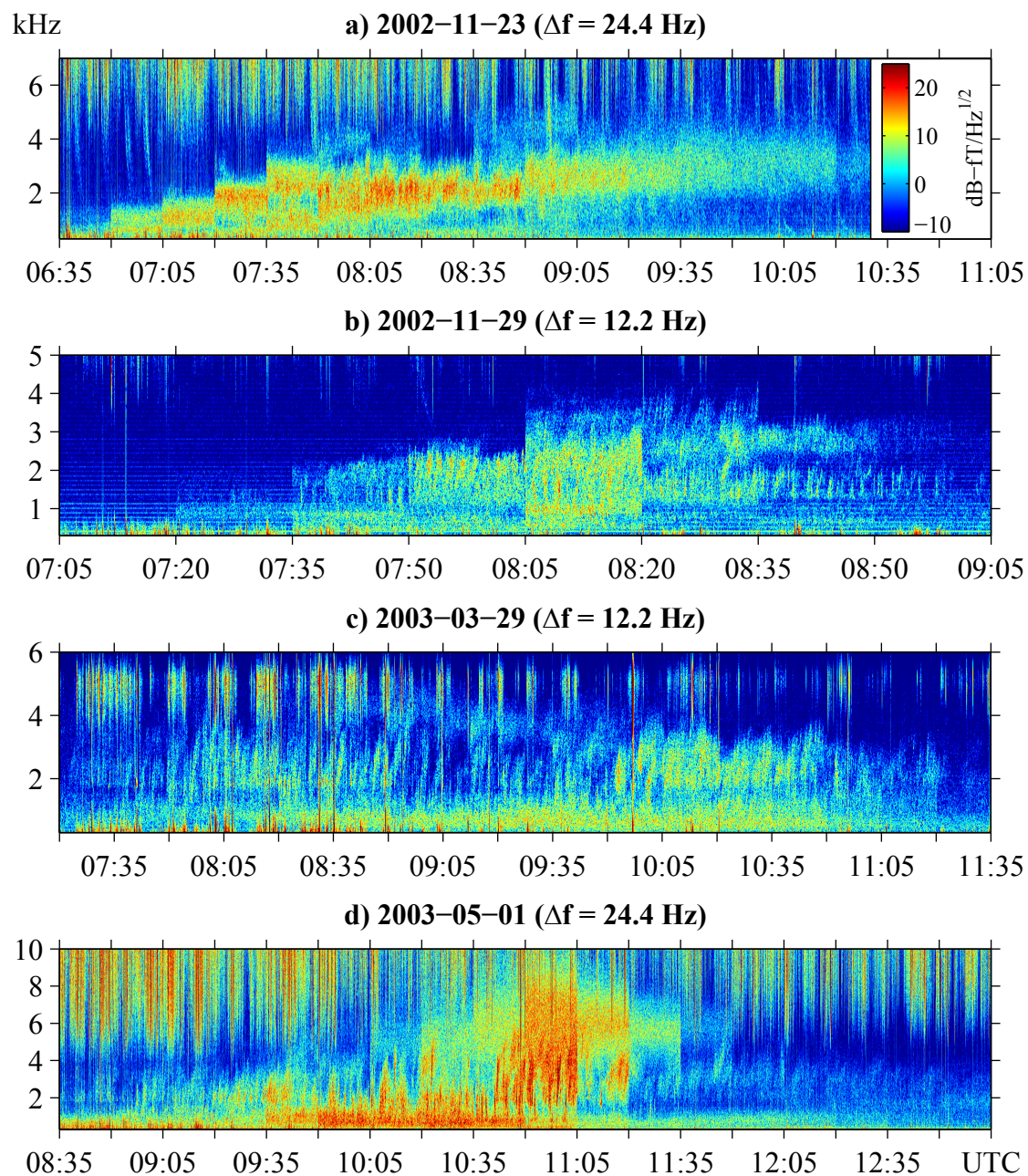


Figure B.1: Synoptic spectrograms showing the progression of chorus emissions.

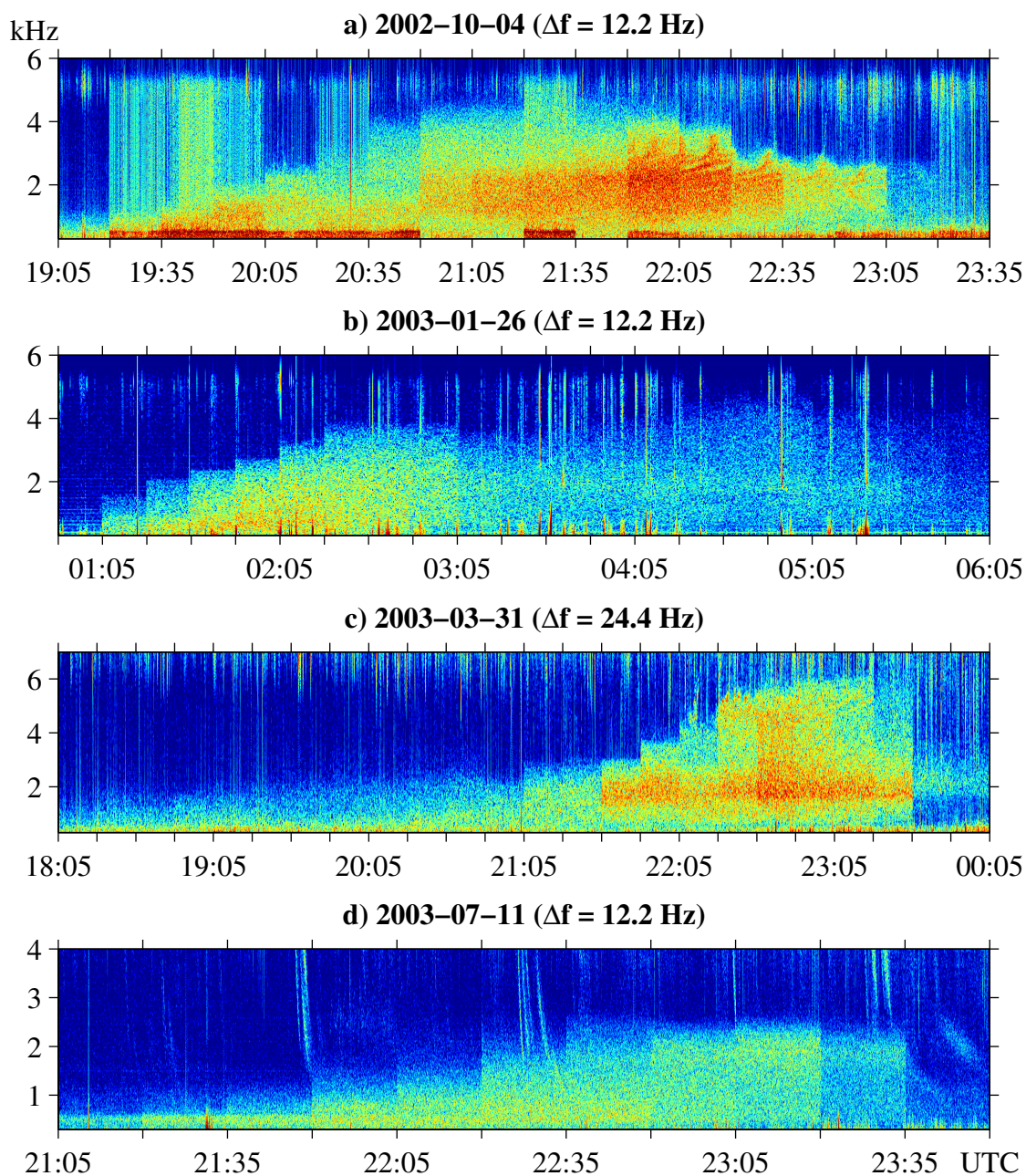


Figure B.2: Synoptic spectrograms showing the progression of hiss emissions.

B.2 Individual Emissions

This section shows individual spectrograms of interesting emissions. These spectrograms are up to 60-seconds in duration. Chorus emissions are shown in Figure B.3, hiss emissions are shown in Figure B.4 and simultaneous overlapping chorus and hiss emissions are shown in Figure B.5. All color scales are the same as shown in Figure B.3a.

Examples of interesting whistler emissions are shown in Figure B.6. Although individual whistlers are quite common at Palmer, the multipath nose whistlers of Figure B.6a are typically a high-latitude phenomenon and are significantly less common at Palmer's middle latitude. Whistlers which hop multiple times between hemispheres as in Figures B.6b-d may cause or contribute to hiss bands and serve as a source of plasmaspheric hiss.

Whistlers may also spontaneously trigger emissions, as shown in Figure B.7. These may either be discrete emissions, as in Figures B.7a,b or continuous chorus or hiss-like emission, as in Figures B.7c,d. Typically, these emissions last for only a short amount of time, up to a few tens of seconds. However, under the right magnetospheric conditions or during periods of intense whistler activity these triggered emissions may persist for longer periods of time.

Finally, Figure B.8 shows exotic free-running emissions which have no obvious triggering source. These include periodic emissions in Figures B.8a,b and intense, high-bandwidth discrete emissions in Figures B.8c,d.

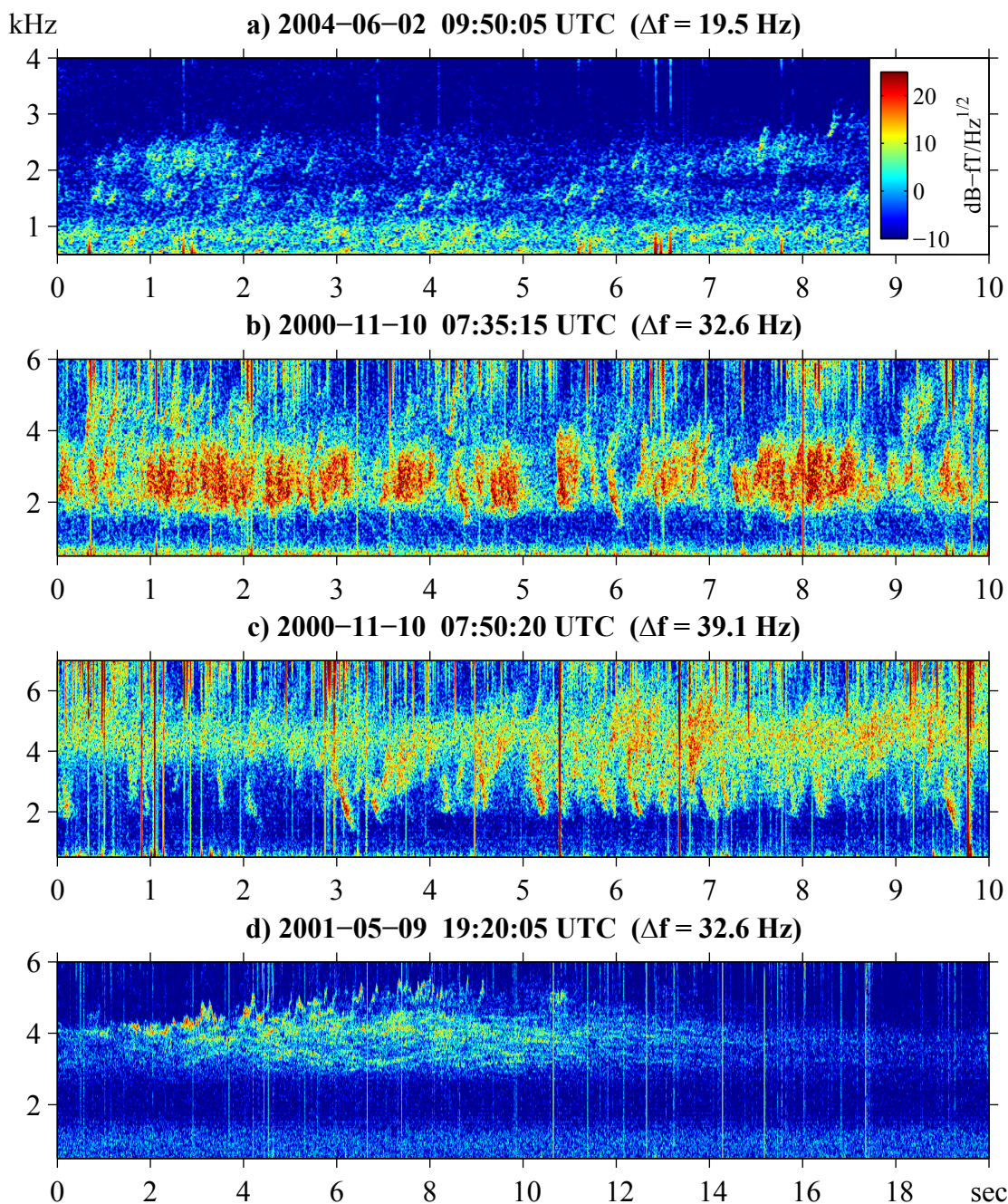


Figure B.3: Examples of chorus emissions. (a) Typical medium-amplitude chorus which is primarily rising tones. (b,c) More intense chorus consists of rising and falling tones of greater bandwidth. (d) A unique chorus emission which appears briefly in an intense burst.

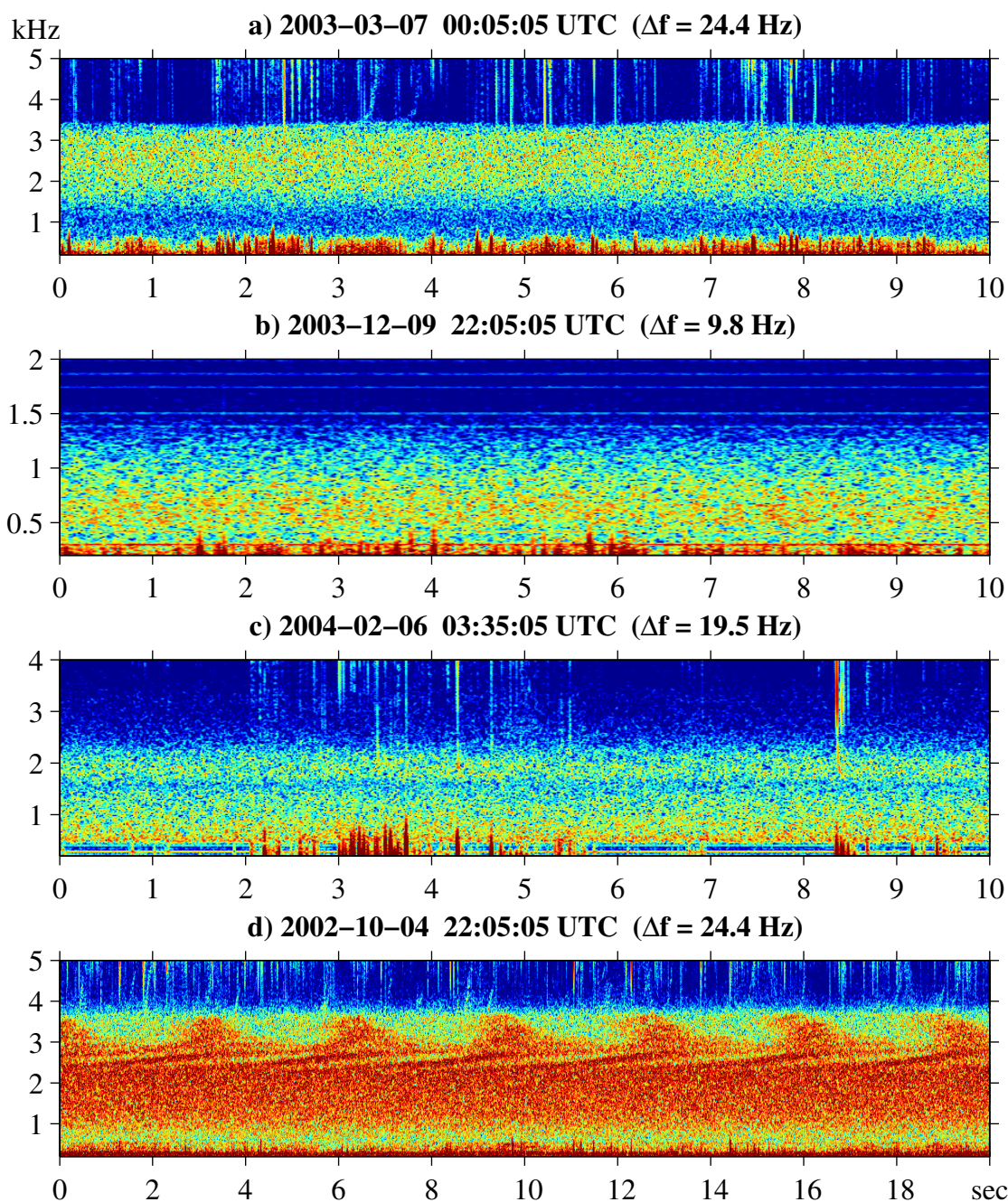


Figure B.4: Examples of hiss emissions. (a) Hiss emission with a sharp upper frequency cutoff and a diffuse lower frequency cutoff. (b) Hiss emission with no obvious lower frequency cutoff. (c) Hiss with a null at 1.8 kHz, likely due to the effects of the Earth-ionosphere waveguide. (d) Hiss overlaid with an intense periodic or multiply-hopping emission.



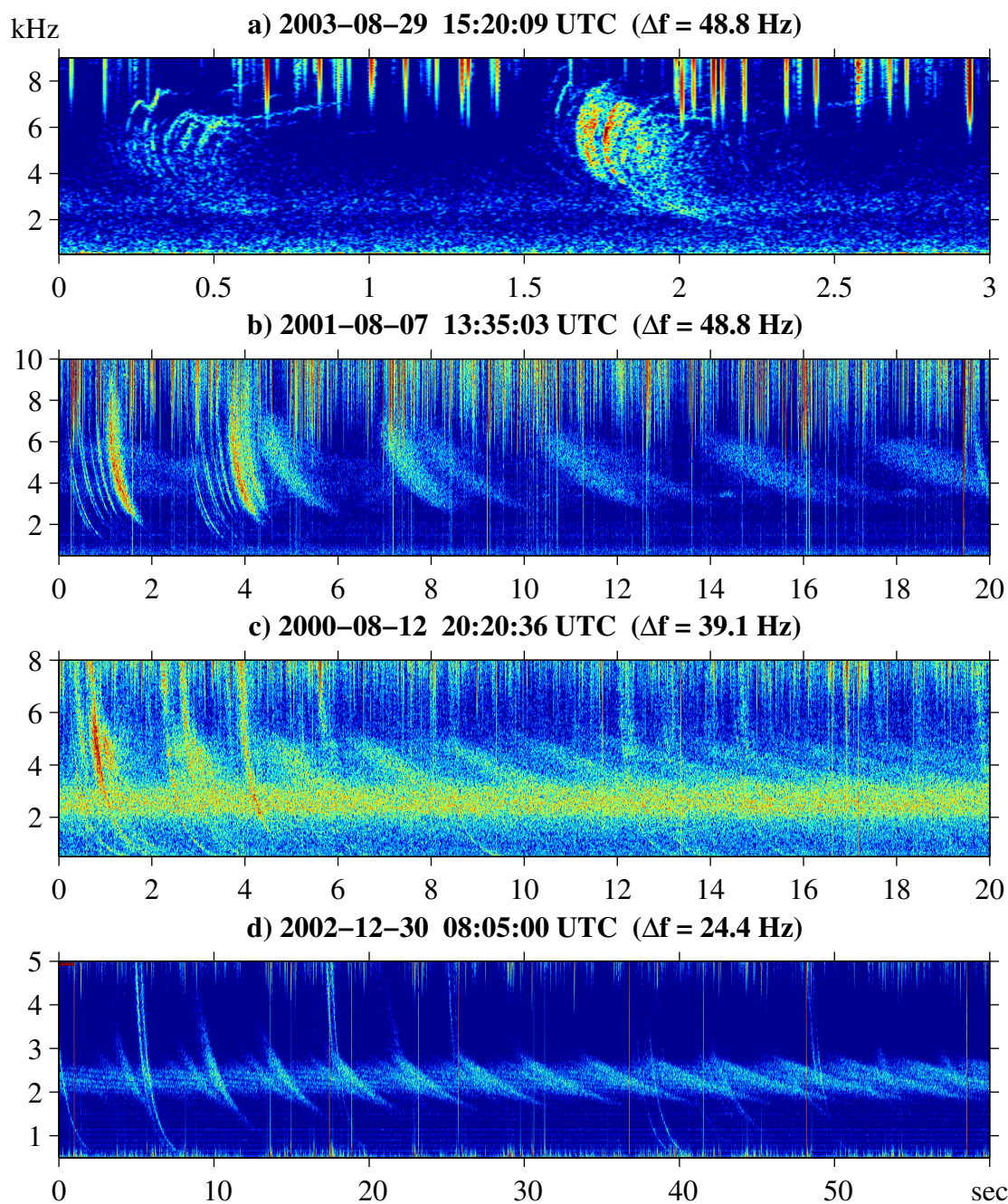


Figure B.6: Examples of whistlers. (a) A multi-component nose whistler caused by a single lightning strike whose energy travels through multiple ducts. (b) Multiply-hopping whistlers, where each successive hop shows increasing dispersion. (c,d) Multiply hopping whistlers contributing to existing hiss bands.

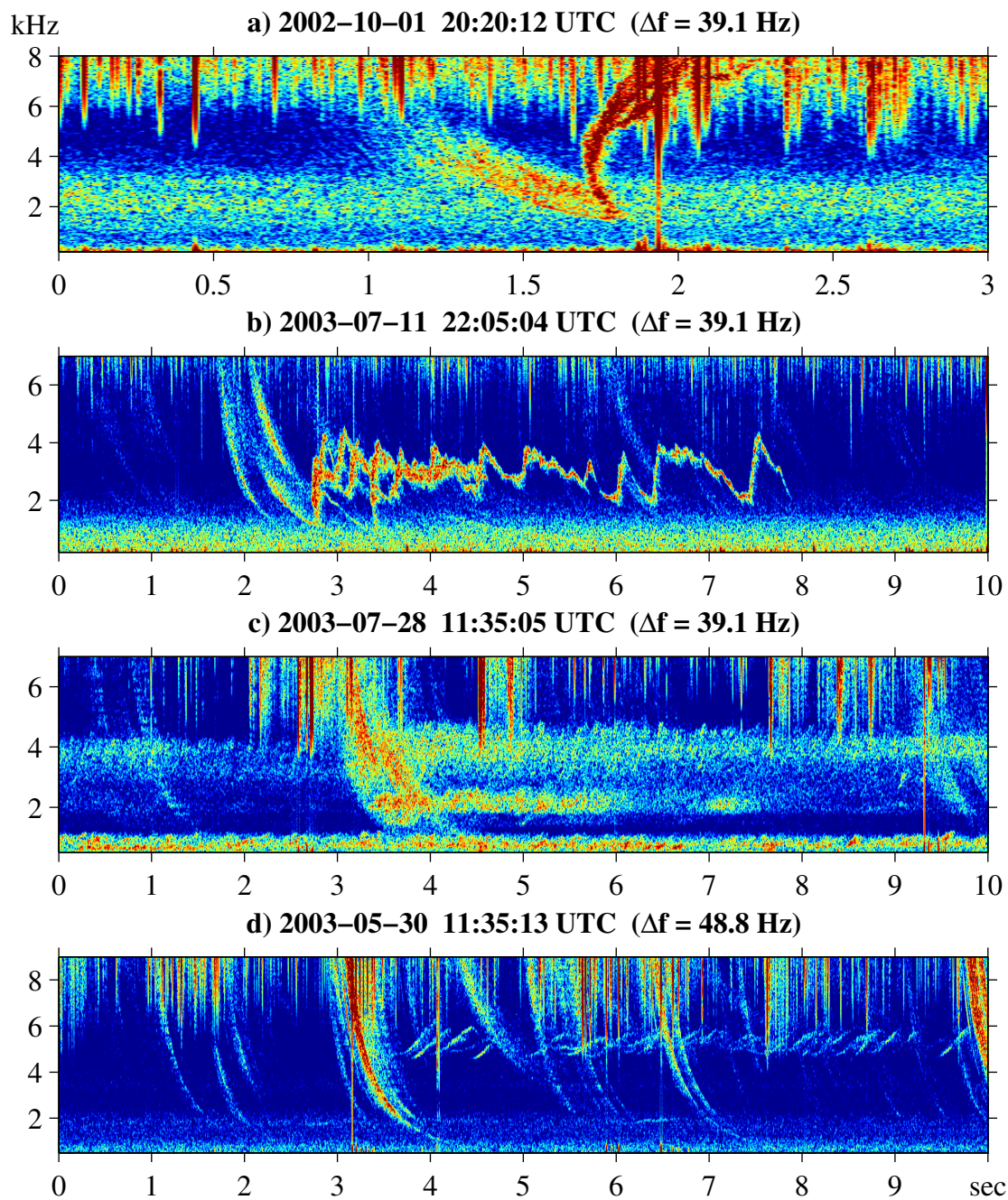


Figure B.7: Examples of emissions triggered from whistlers, including (a,b) discrete emissions and (c,d) chorus-like emissions.

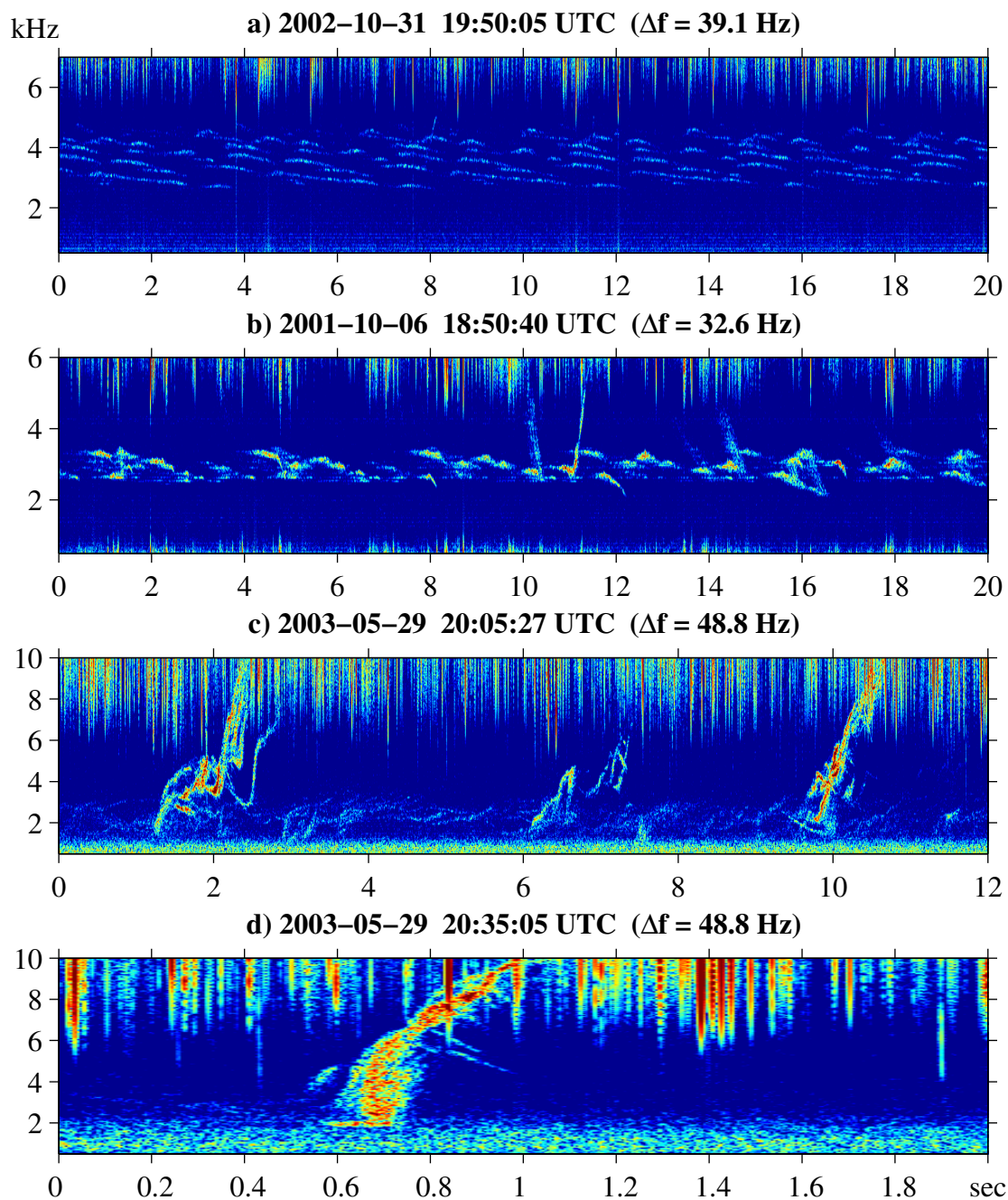


Figure B.8: Examples of uncommon and irregular emissions. (a,b) Periodic emissions. (c) Intense discrete quasi-periodic emissions with a lower band of hiss. (d) 30 minutes later, a zoomed-in view of one discrete emission.

Bibliography

- Abel, B., and R. M. Thorne (1998), Electron scattering loss in Earth's inner magnetosphere 1. Dominant physical processes, *J. Geophys. Res.*, *103*, 2385–2396, doi:10.1029/97JA02919.
- Agresti, A., and B. A. Coull (1998), Approximate is better than "exact" for interval estimation of binomial proportions, *The American Statistician*, *52*(2), pp. 119–126.
- Allcock, G. M. (1957), A Study of the Audio-frequency Radio Phenomenon known as "Dawn Chorus", *Aust. J. Phys.*, *10*, 286.
- Appleton, E. V., and M. A. F. Barnett (1925), On Some Direct Evidence for Downward Atmospheric Reflection of Electric Rays, *Royal Society of London Proceedings Series A*, *109*, 621–641.
- Bailey, J. C., R. J. Blakeslee, D. E. Buechler, and J. J. Christian (2007), Diurnal lightning distributions as observed by the optical transient detector (otd) and the lightning imaging sensor (lis), *13th International Conference on Atmospheric Electricity*, 13-17 Aug. 2007, Beijing, China.
- Baker, D. N. (2000), The occurrence of operational anomalies in spacecraft and their relationship to space weather, *IEEE Transactions on Plasma Science*, *28*, 2007–2016, doi:10.1109/27.902228.
- Bartels, J., N. H. Heck, and H. F. Johnston (1939), The three-hour range index measuring geomagnetic activity, *Terrestrial Magnetism and Atmospheric Activity*, *44*(4), 411–454, doi:10.1029/TE044i004p00411.

- Bauer, S. J. (1973), *Physics of Planetary Ionospheres*, Springer-Verlag, New York, NY.
- Bell, T. F., U. S. Inan, J. Bortnik, and J. D. Scudder (2002), The Landau damping of magnetospherically reflected whistlers within the plasmasphere, *Geophys. Res. Lett.*, *29*(15), 150,000–1, doi:10.1029/2002GL014752.
- Berthelier, A. (1976), Influence of the polarity of the interplanetary magnetic field on the annual and the diurnal variations of magnetic activity, *J. Geophys. Res.*, *81*, 4546–4552, doi:10.1029/JA081i025p04546.
- Bilitza, D., and B. W. Reinisch (2008), International Reference Ionosphere 2007: Improvements and new parameters, *Advances in Space Research*, *42*, 599–609, doi:10.1016/j.asr.2007.07.048.
- Bittencourt, J. A. (2004), *Fundamentals of Plasma Physics*, third ed., Springer-Verlag New York, Inc., New York, NY.
- Bortnik, J., and R. M. Thorne (2007), The dual role of ELF/VLF chorus waves in the acceleration and precipitation of radiation belt electrons, *J. Atmos. Terr. Phys.*, *69*, 378–386, doi:10.1016/j.jastp.2006.05.030.
- Bortnik, J., U. S. Inan, and T. F. Bell (2003), Energy distribution and lifetime of magnetospherically reflecting whistlers in the plasmasphere, *J. Geophys. Res. (Space Phys.)*, *108*, 1199, doi:10.1029/2002JA009316.
- Bortnik, J., R. M. Thorne, and N. P. Meredith (2007a), Modeling the propagation characteristics of chorus using CRRES suprathermal electron fluxes, *J. Geophys. Res. (Space Phys.)*, *112*, 8204, doi:10.1029/2006JA012237.
- Bortnik, J., R. M. Thorne, N. P. Meredith, and O. Santolik (2007b), Ray tracing of penetrating chorus and its implications for the radiation belts, *Geophys. Res. Lett.*, *34*, 15,109, doi:10.1029/2007GL030040.

- Bortnik, J., R. M. Thorne, and N. P. Meredith (2008), The unexpected origin of plasmaspheric hiss from discrete chorus emissions, *Nature*, *452*, 62–66, doi:10.1038/nature06741.
- Brinca, A. L. (1972), On the Stability of Obliquely Propagating Whistlers, *J. Geophys. Res.*, *77*, 3495–3507, doi:10.1029/JA077i019p03495.
- Burch, J. L. (2000), IMAGE mission overview, *Space Sci. Rev.*, *91*, 1–14.
- Burgess, W. C. (1993), Lightning-induced coupling of the radiation belts to geomagnetically conjugate ionospheric regions, Ph.D. thesis, Stanford Univ., CA.
- Burtis, W. J., and R. A. Helliwell (1975), Magnetospheric chorus - Amplitude and growth rate, *J. Geophys. Res.*, *80*, 3265–3270.
- Burtis, W. J., and R. A. Helliwell (1976), Magnetospheric chorus: Occurrence patterns and normalized frequency, *Planet. Space Sci.*, *24*, 1007–1007, doi:10.1016/0032-0633(76)90119-7.
- Carpenter, D., and J. Lemaire (2004), The Plasmasphere Boundary Layer, *Ann. Geophys.*, *22*, 4291–4298.
- Carpenter, D. L. (1970), Whistler Evidence of the Dynamic Behavior of the Dusk-side Bulge in the Plasmasphere, *J. Geophys. Res.*, *75*, 3837–3847, doi:10.1029/JA075i019p03837.
- Carpenter, D. L., and R. R. Anderson (1992), An ISEE/Whistler model of equatorial electron density in the magnetosphere, *J. Geophys. Res.*, *97*, 1097–1108, doi:10.1029/91JA01548.
- Carpenter, D. L., and A. J. Smith (2001), The study of bulk plasma motions and associated electric fields in the plasmasphere by means of whistler-mode signals, *J. Atmos. Terr. Phys.*, *63*, 1117–1132, doi:10.1016/S1364-6826(00)00217-0.
- Carpenter, D. L., J. C. Foster, T. J. Rosenberg, and L. J. Lanzerotti (1975), A subauroral and mid-latitude view of substorm activity, *J. Geophys. Res.*, *80*, 4279–4286.

- Carpenter, D. L., et al. (2002), Small-scale field-aligned plasmaspheric density structures inferred from the Radio Plasma Imager on IMAGE, *J. Geophys. Res. (Space Phys.)*, *107*, 1258, doi:10.1029/2001JA009199.
- Chapman, S., and J. Bartels (1940), *Geomagnetism*, Oxford Univ. Press, London.
- Chatterjee, S., and A. S. Hadi (2006), *Regression Analysis by Example*, fourth ed., Wiley-Interscience, Hoboken, NJ.
- Chen, L., J. Bortnik, R. M. Thorne, R. B. Horne, and V. K. Jordanova (2009), Three-dimensional ray tracing of VLF waves in a magnetospheric environment containing a plasmaspheric plume, *Geophys. Res. Lett.*, *36*, 22,101, doi:10.1029/2009GL040451.
- Christian, H. J., et al. (2003), Global frequency and distribution of lightning as observed from space by the Optical Transient Detector, *J. Geophys. Res. (Atmos.)*, *108*, 4005, doi:10.1029/2002JD002347.
- Chum, J., and O. Santolík (2005), Propagation of whistler-mode chorus to low altitudes: divergent ray trajectories and ground accessibility, *Ann. Geophys.*, *23*, 3727–3738.
- Church, S. R., and R. M. Thorne (1983), On the origin of plasmaspheric hiss - Ray path integrated amplification, *J. Geophys. Res.*, *88*, 7941–7957.
- Cohen, M. B., R. K. Said, and U. S. Inan (2010), Mitigation of 50-60 hz power line interference in geophysical data, *Radio Sci.*, doi:10.1029/2010RS004420.
- Cole, D. G. (2003), Space weather: its effects and predictability, *Space Sci. Rev.*, *107*, 295–302, doi:10.1023/A:1025500513499.
- Comfort, R. H. (1986), Plasmasphere thermal structure as measured by ISEE-1 and DE-1, *Advances in Space Research*, *6*, 31–40, doi:10.1016/0273-1177(86)90314-5.
- Cornilleau-Wehrlin, N., R. Gendrin, F. Lefeuvre, M. Parrot, R. Grard, D. Jones, A. Bahnsen, E. Ungstrup, and W. Gibbons (1978), VLF electromagnetic waves observed onboard GEOS-1, *Space Sci. Rev.*, *22*, 371–382.

- Daglis, I. A., R. M. Thorne, W. Baumjohann, and S. Orsini (1999), The terrestrial ring current: Origin, formation, and decay, *Reviews of Geophysics*, *37*, 407–438, doi:10.1029/1999RG900009.
- Davis, T. N., and M. Sugiura (1966), Auroral Electrojet Activity Index AE and Its Universal Time Variations, *J. Geophys. Res.*, *71*, 785.
- Dowden, R. L. (1971), Distinctions between mid latitude VLF hiss and discrete emissions, *Planet. Space Sci.*, *19*, 374–376, doi:10.1016/0032-0633(71)90100-0.
- Draganov, A. B., U. S. Inan, V. S. Sonwalkar, and T. F. Bell (1992), Magnetospherically reflected whistlers as a source of plasmaspheric hiss, *Geophys. Res. Lett.*, *19*, 233–236.
- Dunckel, N., and R. A. Helliwell (1969), Whistler-Mode Emissions on the OGO 1 Satellite, *J. Geophys. Res.*, *74*, 6371–6385, doi:10.1029/JA074i026p06371.
- Dungey, J. W. (1961), Interplanetary Magnetic Field and the Auroral Zones, *Physical Review Letters*, *6*, 47–48, doi:10.1103/PhysRevLett.6.47.
- Fälthammar, C. (1965), Effects of Time-Dependent Electric Fields on Geomagnetically Trapped Radiation, *J. Geophys. Res.*, *70*, 2503–2516, doi:10.1029/JZ070i011p02503.
- Gail, W. B., and D. L. Carpenter (1984), Whistler induced suppression of VLF noise, *J. Geophys. Res.*, *89*, 1015–1022, doi:10.1029/JA089iA02p01015.
- Gallagher, D. L., P. D. Craven, and R. H. Comfort (2000), Global core plasma model, *J. Geophys. Res.*, *105*, 18,819–18,834, doi:10.1029/1999JA000241.
- Godsill, S. J., and P. J. W. Rayner (1998), *Digital audio restoration : a statistical model based approach*, Springer, New York, NY.
- Golden, D. I., M. Spasojevic, and U. S. Inan (2009), Diurnal dependence of ELF/VLF hiss and its relation to chorus at L = 2.4, *J. Geophys. Res. (Space Phys.)*, *114* (A13), 5212, doi:10.1029/2008JA013946.

- Golden, D. I., M. Spasojevic, F. R. Foust, N. G. Lehtinen, N. P. Meredith, and U. S. Inan (2010), Role of the plasmopause in dictating the ground accessibility of ELF/VLF chorus, *J. Geophys. Res. (Space Phys.)*, *115*, 11,211, doi:10.1029/2010JA015955.
- Golden, D. I., M. Spasojevic, and U. S. Inan (2011), Determination of solar cycle variations of mid-latitude ELF/VLF chorus and hiss via automated signal detection, *J. Geophys. Res. (Space Phys.)*, doi:10.1029/2010JA016193.
- Goldstein, J., M. Spasojević, P. H. Reiff, B. R. Sandel, W. T. Forrester, D. L. Gallagher, and B. W. Reinisch (2003), Identifying the plasmopause in IMAGE EUV data using IMAGE RPI in situ steep density gradients, *J. Geophys. Res. (Space Phys.)*, *108*, 1147, doi:10.1029/2002JA009475.
- Gołkowski, M., and U. S. Inan (2008), Multistation observations of ELF/VLF whistler mode chorus, *J. Geophys. Res. (Space Phys.)*, *113*, 8210, doi:10.1029/2007JA012977.
- Green, J. L., S. Boardsen, L. Garcia, W. W. L. Taylor, S. F. Fung, and B. W. Reinisch (2005), On the origin of whistler mode radiation in the plasmasphere, *J. Geophys. Res. (Space Phys.)*, *110*(A9), 3201, doi:10.1029/2004JA010495.
- Gubbins, D. (1981), Rotation of the Inner Core, *J. Geophys. Res.*, *86*, 11,695–11,699, doi:10.1029/JB086iB12p11695.
- Gurnett, D. A., and T. B. Burns (1968), The Low-Frequency Cutoff of ELF Emissions, *J. Geophys. Res.*, *73*, 7437–7445, doi:10.1029/JA073i023p07437.
- Gurnett, D. A., and B. J. O'Brien (1964), High-Latitude Geophysical Studies with Satellite Injun 3, 5, Very Low Frequency Electromagnetic Radiation, *J. Geophys. Res.*, *69*, 65, doi:10.1029/JZ069i001p00065.
- Gustafsson, G., N. E. Papitashvili, and V. O. Papitashvili (1992), A revised corrected geomagnetic coordinate system for Epochs 1985 and 1990, *Journal of Atmospheric and Terrestrial Physics*, *54*, 1609–1631.

- Haque, N., M. Spasojevic, O. Santolík, and U. S. Inan (2010), Wave normal angles of magnetospheric chorus emissions observed on the Polar spacecraft, *Journal of Geophysical Research (Space Physics)*, *115*, doi:10.1029/2009JA014717.
- Haselgrove, J. (1955), Ray Theory and a New Method for Ray Tracing, in *Physics of the Ionosphere*, p. 355.
- Hayakawa, M., and S. S. Sazhin (1992), Mid-latitude and plasmaspheric hiss - A review, *Planet. Space Sci.*, *40*, 1325–1338, doi:10.1016/0032-0633(92)90089-7.
- Hayakawa, M., Y. Tanaka, and J. Ohtsu (1975a), The morphologies of low-latitude and auroral VLF ‘hiss’, *J. Atmos. Terr. Phys.*, *37*, 517–529.
- Hayakawa, M., Y. Tanaka, and J. Ohtsu (1975b), Satellite and ground observations of magnetospheric VLF hiss associated with the severe magnetic storm on May 25–27, 1967, *J. Geophys. Res.*, *80*, 86–92.
- Hayakawa, M., K. Bullough, and T. R. Kaiser (1977), Properties of storm-time magnetospheric VLF emissions as deduced from the Ariel 3 satellite and ground-based observations, *Planet. Space Sci.*, *25*, 353–368, doi:10.1016/0032-0633(77)90051-4.
- Hayakawa, M., Y. Yamanaka, M. Parrot, and F. Lefeuvre (1984), The wave normals of magnetospheric chorus emissions observed on board GEOS 2, *J. Geophys. Res.*, *89*, 2811–2821, doi:10.1029/JA089iA05p02811.
- Hayakawa, M., Y. Tanaka, and T. Okada (1985), Morphological characteristics and the polarization of plasmaspheric ELF hiss observed at Moshiri ($L \sim 1.6$), *J. Geophys. Res.*, *90*, 5133–5140.
- Hayakawa, M., Y. Tanaka, T. Okada, M. Tixier, and S. S. Sazhin (1988), Substorm-associated VLF emissions with frequency drift observed in the premidnight sector, *J. Geophys. Res.*, *93*, 5685–5700.
- Helliwell, R. A. (1965), *Whistlers and Related Ionospheric Phenomena*, Stanford University Press, Stanford, CA.

- Helliwell, R. A., J. Katsufakis, M. Trimpi, and N. Brice (1964), Artificially Stimulated Very Low Frequency Radiation from the Ionosphere, *J. Geophys. Res.*, *69*, 2391–2394, doi:10.1029/JZ069i011p02391.
- Helliwell, R. A., D. L. Carpenter, U. S. Inan, and J. P. Katsufakis (1986), Generation of band-limited VLF noise using the Siple transmitter - A model for magnetospheric hiss, *J. Geophys. Res.*, *91*, 4381–4392, doi:10.1029/JA091iA04p04381.
- Horne, R. B., S. A. Glauert, and R. M. Thorne (2003), Resonant diffusion of radiation belt electrons by whistler-mode chorus, *Geophys. Res. Lett.*, *30*(9), 090,000–1, doi:10.1029/2003GL016963.
- Horne, R. B., et al. (2005), Wave acceleration of electrons in the Van Allen radiation belts, *Nature*, *437*, 227–230, doi:10.1038/nature03939.
- Inan, U. S., and T. F. Bell (1977), The plasmopause as a VLF wave guide, *J. Geophys. Res.*, *82*, 2819–2827, doi:10.1029/JA082i019p02819.
- Jørgensen, T. S. (1968), Interpretation of Auroral Hiss Measured on OGO 2 and at Byrd Station in Terms of Incoherent Cerenkov Radiation, *J. Geophys. Res.*, *73*, 1055–1069, doi:10.1029/JA073i003p01055.
- Kennel, C. (1966), Low-Frequency Whistler Mode, *Physics of Fluids*, *9*, 2190–2202, doi:10.1063/1.1761588.
- Kennel, C. F., and H. E. Petscheck (1966), Limit on stably trapped particle fluxes, *J. Geophys. Res.*, *71*, 1–28.
- Kennel, C. F., and R. M. Thorne (1967), Unstable Growth of Unducted Whistlers Propagating at an Angle to the Geomagnetic Field, *J. Geophys. Res.*, *72*, 871.
- Kerr, N. L. (1998), HARKing: Hypothesizing After the Results are Known, *Pers. Soc. Psychol. Rev.*, *2*(3), 196–217, doi:10.1207/s15327957pspr0203\4.
- Kimura, I. (1966), Effects of ions on whistler-mode ray tracing, *Radio Sci.*, *1*(3), 269.

- Kivelson, M. G., and C. T. Russell (1995), *Introduction to Space Physics*, Cambridge University Press, Cambridge, UK.
- Kleimenova, N. G., M. S. Kovner, and V. A. Kuznetsova (1976), VLF-ground observations near the plasmapause projections, *J. Atmos. Terr. Phys.*, *38*, 1215.
- Koons, H. C. (1981), The role of hiss in magnetospheric chorus emissions, *J. Geophys. Res.*, *86*, 6745–6754.
- Laaspere, T., M. G. Morgan, and W. C. Johnson (1964), Chorus, hiss, and other audio-frequency emissions at stations of the whistlers-east network, *Proc. IEEE*, *52*(11), 1331–1349.
- LeDocq, M. J., D. A. Gurnett, and G. B. Hospodarsky (1998), Chorus Source Locations from VLF Poynting Flux Measurements with the Polar Spacecraft, *Geophys. Res. Lett.*, *25*, 4063, doi:10.1029/1998GL900071.
- Lehtinen, N. G., and U. S. Inan (2008), Radiation of ELF/VLF waves by harmonically varying currents into a stratified ionosphere with application to radiation by a modulated electrojet, *J. Geophys. Res. (Space Phys.)*, *113*, 6301, doi:10.1029/2007JA012911.
- Lehtinen, N. G., and U. S. Inan (2009), Full-wave modeling of transionospheric propagation of VLF waves, *Geophys. Res. Lett.*, *36*, 3104, doi:10.1029/2008GL036535.
- Lekien, F., and J. Marsden (2005), Tricubic interpolation in three dimensions, *International Journal For Numerical Methods in Engineering*, *63*, 455–471.
- Lemaire, J. (1989), Plasma distribution models in a rotating magnetic dipole and refilling of plasmaspheric flux tubes, *Physics of Fluids B*, *1*, 1519–1525, doi:10.1063/1.858928.
- Lichtenberger, J., C. Ferencz, L. Bodnár, D. Hamar, and P. Steinbach (2008), Automatic Whistler Detector and Analyzer system: Automatic Whistler Detector, *J. Geophys. Res. (Space Phys.)*, *113*, 12,201, doi:10.1029/2008JA013467.

- Lorentzen, K. R., J. B. Blake, U. S. Inan, and J. Bortnik (2001), Observations of relativistic electron microbursts in association with VLF chorus, *J. Geophys. Res.*, *106*, 6017–6028, doi:10.1029/2000JA003018.
- Lyons, L. R., and R. M. Thorne (1973), Equilibrium Structure of Radiation Belt Electrons, *J. Geophys. Res.*, *78*, 2142–2149, doi:10.1029/JA078i013p02142.
- Lyons, L. R., R. M. Thorne, and C. F. Kennel (1972), Pitch-angle diffusion of radiation belt electrons within the plasmasphere., *J. Geophys. Res.*, *77*, 3455–3474.
- Maeda, K. (1962), Whistlers and VLF Emissions in Connection with the Earth Storm, *J. Phys. Soc. Jpn. Supplement*, *17*, B95.
- Makita, K. (1979), VLF-LF hiss emissions associated with the aurora, *Mem. Natl. Inst. Polar Res., Ser. A, Aeronomy*, *16*.
- McIlwain, C. E. (1961), Coordinates for Mapping the Distribution of Magnetically Trapped Particles, *J. Geophys. Res.*, *66*, 3681–3691, doi:10.1029/JZ066i011p03681.
- Meredith, N. P., R. B. Horne, and R. R. Anderson (2001), Substorm dependence of chorus amplitudes: Implications for the acceleration of electrons to relativistic energies, *J. Geophys. Res.*, *106*, 13,165–13,178, doi:10.1029/2000JA900156.
- Meredith, N. P., R. B. Horne, D. Summers, R. M. Thorne, R. H. A. Iles, D. Heynderickx, and R. R. Anderson (2002), Evidence for acceleration of outer zone electrons to relativistic energies by whistler mode chorus, *Ann. Geophys.*, *20*, 967–979.
- Meredith, N. P., R. B. Horne, R. M. Thorne, D. Summers, and R. R. Anderson (2004), Substorm dependence of plasmaspheric hiss, *J. Geophys. Res. (Space Phys.)*, *109*(A18), 6209, doi:10.1029/2004JA010387.
- Meredith, N. P., R. B. Horne, M. A. Clilverd, D. Horsfall, R. M. Thorne, and R. R. Anderson (2006), Origins of plasmaspheric hiss, *J. Geophys. Res. (Space Phys.)*, *111*(A10), 9217, doi:10.1029/2006JA011707.

- Møller, M. F. (1993), A scaled conjugate gradient algorithm for fast supervised learning, *Neural Networks*, *6*(4), 525–533, doi:DOI:10.1016/S0893-6080(05)80056-5.
- Murayama, T. (1982), Coupling function between solar wind parameters and geomagnetic indices, *Rev. Geophys. Space Phys.*, *20*, 623–629.
- Navidi, W. (2006), *Statistics for Engineers and Scientists*, McGraw-Hill, New York, NY.
- Neugebauer, M., and C. W. Snyder (1966), Mariner 2 Observations of the Solar Wind, 1, Average Properties, *J. Geophys. Res.*, *71*, 4469.
- Newberry, I. T., R. H. Comfort, P. G. Richards, and C. R. Chappell (1989), Thermal He(+) in the plasmasphere - Comparison of observations with numerical calculations, *J. Geophys. Res.*, *94*, 15,265–15,276, doi:10.1029/JA094iA11p15265.
- Nguyen, D., and B. Widrow (1990), Improving the learning speed of 2-layer neural networks by choosing initial values of the adaptive weights, *Neural Networks*, *1990.*, *1990 IJCNN International Joint Conference on*, pp. 21–26 vol.3, doi:10.1109/IJCNN.1990.137819.
- Nunn, D., Y. Omura, H. Matsumoto, I. Nagano, and S. Yagitani (1997), The numerical simulation of VLF chorus and discrete emissions observed on the Geotail satellite using a Vlasov code, *J. Geophys. Res.*, *102*, 27,083–27,098, doi:10.1029/97JA02518.
- O’Brien, T. P., K. R. Lorentzen, I. R. Mann, N. P. Meredith, J. B. Blake, J. F. Fennell, M. D. Looper, D. K. Milling, and R. R. Anderson (2003), Energization of relativistic electrons in the presence of ULF power and MeV microbursts: Evidence for dual ULF and VLF acceleration, *J. Geophys. Res. (Space Phys.)*, *108*, 1329, doi:10.1029/2002JA009784.
- Papitashvili, N. (2001), Corrected geomagnetic coordinates, http://omniweb.gsfc.nasa.gov/vitmo/cgmm_des.html, Accessed January 2011.

- Parady, B. K., D. D. Eberlein, J. A. Marvin, W. W. L. Taylor, and J. L. J. Cahill (1975), Plasmaspheric hiss observations in the evening and afternoon quadrants, *J. Geophys. Res.*, *80*, 2183–2198.
- Park, C. G. (1972), Methods of determining electron concentrations in the magnetosphere from nose whistlers, *Tech. Rep. 3454-1*, Stanford University, Stanford, CA.
- Parrot, M., O. Santolík, D. Gurnett, J. Pickett, and N. Cornilleau-Wehrlin (2004), Characteristics of magnetospherically reflected chorus waves observed by CLUSTER, *Ann. Geophys.*, *22*, 2597–2606.
- Pope, J. H. (1957), Diurnal Variation in the Occurrence of ‘Dawn Chorus’, *Nature*, *180*, 433, doi:10.1038/180433a0.
- Pope, J. H. (1960), Effect of Latitude on the Diurnal Maximum of ‘Dawn Chorus’, *Nature*, *185*, 87–88, doi:10.1038/185087b0.
- Roederer, J. G. (1970), *Dynamics of geomagnetically trapped radiation*.
- Roelof, E. C., and A. J. Skinner (2000), Extraction of ion distributions from magnetospheric ENA and EUV images, *Space Sci. Rev.*, *91*, 437–459.
- Russell, C. T., and R. L. McPherron (1973), Semiannual variation of geomagnetic activity., *J. Geophys. Res.*, *78*, 92–108, doi:10.1029/JA078i001p00092.
- Russell, C. T., R. E. Holzer, and E. J. Smith (1969), OGO 3 observations of ELF noise in the magnetosphere. 1. Spatial extent and frequency of occurrence., *J. Geophys. Res.*, *74*, 755–777.
- Russell, C. T., R. L. McPherron, and J. P. J. Coleman (1972), Fluctuating Magnetic Fields in the Magnetosphere. I: ELF and VLF Fluctuations, *Space Sci. Rev.*, *12*, 810–856, doi:10.1007/BF00173072.
- Said, R. K. (2009), Accurate and efficient long-range lightning geo-location using a vlf radio atmospheric waveform bank, Ph.D. thesis, Stanford Univ., CA.

- Said, R. K., U. S. Inan, and K. L. Cummins (2010), Long-range lightning geolocation using a VLF radio atmospheric waveform bank, *J. Geophys. Res. (Atmos.)*, *115*, 23,108, doi:10.1029/2010JD013863.
- Sandel, B. R., et al. (2000), The Extreme Ultraviolet Imager Investigation for the IMAGE Mission, *Space Sci. Rev.*, *91*, 197–242.
- Santolík, O. (2008), New results of investigations of whistler-mode chorus emissions, *Nonlinear Proc. Geoph.*, *15*, 621–630.
- Santolík, O., D. A. Gurnett, J. S. Pickett, M. Parrot, and N. Cornilleau-Wehrin (2005), Central position of the source region of storm-time chorus, *Planet. Space Sci.*, *53*, 299–305, doi:10.1016/j.pss.2004.09.056.
- Santolík, O., J. Chum, M. Parrot, D. A. Gurnett, J. S. Pickett, and N. Cornilleau-Wehrin (2006), Propagation of whistler mode chorus to low altitudes: Spacecraft observations of structured ELF hiss, *J. Geophys. Res. (Space Phys.)*, *111*(A10), 10,208, doi:10.1029/2005JA011462.
- Sazhin, S. S., and M. Hayakawa (1992), Magnetospheric chorus emissions - A review, *Planet. Space Sci.*, *40*, 681–697, doi:10.1016/0032-0633(92)90009-D.
- Sazhin, S. S., and M. Hayakawa (1994), Periodic and quasiperiodic VLF emissions, *J. Atmos. Terr. Phys.*, *56*, 735–753.
- Schulz, M., and L. J. Lanzerotti (1974), *Particle diffusion in the radiation belts*.
- Shprits, Y. Y., R. M. Thorne, R. B. Horne, S. A. Glauert, M. Cartwright, C. T. Russell, D. N. Baker, and S. G. Kanekal (2006), Acceleration mechanism responsible for the formation of the new radiation belt during the 2003 Halloween solar storm, *Geophys. Res. Lett.*, *33*, 5104, doi:10.1029/2005GL024256.
- Shprits, Y. Y., S. R. Elkington, N. P. Meredith, and D. A. Subbotin (2008a), Review of modeling of losses and sources of relativistic electrons in the outer radiation belt I: Radial transport, *J. Atmos. Terr. Phys.*, *70*, 1679–1693, doi:10.1016/j.jastp.2008.06.008.

- Shprits, Y. Y., D. A. Subbotin, N. P. Meredith, and S. R. Elkington (2008b), Review of modeling of losses and sources of relativistic electrons in the outer radiation belt II: Local acceleration and loss, *J. Atmos. Terr. Phys.*, *70*, 1694–1713, doi:10.1016/j.jastp.2008.06.014.
- Smith, A. J., M. P. Freeman, and G. D. Reeves (1996), Postmidnight VLF chorus events, a substorm signature observed at the ground near L=4, *J. Geophys. Res.*, *101*, 24,641–24,654, doi:10.1029/96JA02236.
- Smith, A. J., M. P. Freeman, M. G. Wickett, and B. D. Cox (1999), On the relationship between the magnetic and VLF signatures of the substorm expansion phase, *J. Geophys. Res.*, *104*, 12,351–12,360, doi:10.1029/1998JA900184.
- Smith, A. J., R. B. Horne, and N. P. Meredith (2004), Ground observations of chorus following geomagnetic storms, *J. Geophys. Res. (Space Phys.)*, *109*(A18), 2205, doi:10.1029/2003JA010204.
- Smith, A. J., R. B. Horne, and N. P. Meredith (2010), The statistics of natural ELF/VLF waves derived from a long continuous set of ground-based observations at high latitude, *J. Atmos. Terr. Phys.*, *72*, 463–475, doi:10.1016/j.jastp.2009.12.018.
- Sonwalkar, V. S. (1995), *Handbook of Atmospheric Electrodynamics*, vol. II, chap. Magnetospheric LF-, VLF-, and ELF-Waves, pp. 407–460, CRC Press.
- Sonwalkar, V. S., and J. Harikumar (2000), An explanation of ground observations of auroral hiss: Role of density depletions and meter-scale irregularities, *J. Geophys. Res.*, *105*, 18,867–18,884, doi:10.1029/1999JA000302.
- Sonwalkar, V. S., and U. S. Inan (1989), Lightning as an embryonic source of VLF hiss, *J. Geophys. Res.*, *94*, 6986–6994.
- Spasojević, M. (2003), Global dynamics of the earth’s plasmasphere, Ph.D. thesis, Stanford Univ., CA.

- Spasojevic, M., and U. S. Inan (2005), Ground based VLF observations near $L = 2.5$ during the Halloween 2003 storm, *Geophys. Res. Lett.*, *32*, 21,103, doi:10.1029/2005GL024377.
- Spasojevic, M., and U. S. Inan (2010), Drivers of chorus in the outer dayside magnetosphere, *Journal of Geophysical Research (Space Physics)*, *115*, doi:10.1029/2009JA014452.
- Storey, L. R. O. (1953), An Investigation of Whistling Atmospherics, *Philos. Trans. R. Soc. London, Ser. A*, *246*, 113–141.
- Sugiura, M. (1964), Hourly values of equatorial Dst for IGY, in *Annals of the International Geophysical Year*, vol. 35, pp. 945–948, Pergamon Press, Oxford.
- Taylor, W. W. L., and D. A. Gurnett (1968), Morphology of VLF Emissions Observed with the Injun 3 Satellite, *J. Geophys. Res.*, *73*, 5615.
- Thorne, R. M., and C. F. Kennel (1967), Quasi-Trapped VLF Propagation in the Outer Magnetosphere, *J. Geophys. Res.*, *72*, 857.
- Thorne, R. M., E. J. Smith, R. K. Burton, and R. E. Holzer (1973), Plasmaspheric Hiss, *J. Geophys. Res.*, *78*, 1581–1596, doi:10.1029/JA078i010p01581.
- Thorne, R. M., S. R. Church, and D. J. Gorney (1979), On the origin of plasmaspheric hiss - The importance of wave propagation and the plasmopause, *J. Geophys. Res.*, *84*, 5241–5247.
- Thorne, R. M., T. P. O'Brien, Y. Y. Shprits, D. Summers, and R. B. Horne (2005), Timescale for MeV electron microburst loss during geomagnetic storms, *J. Geophys. Res. (Space Phys.)*, *110*, 9202, doi:10.1029/2004JA010882.
- Trakhtengerts, V. Y. (1999), A generation mechanism for chorus emission, *Ann. Geophys.*, *17*, 95–100, doi:10.1007/s00585-999-0095-4.
- Tsuruda, K., S. Machida, T. Terasawa, A. Nishida, and K. Maezawa (1982), High spatial attenuation of the Siple transmitter signal and natural VLF chorus observed

- at ground-based chain stations near Roberval, Quebec, *J. Geophys. Res.*, *87*, 742–750.
- Tsurutani, B. T., and E. J. Smith (1974), Postmidnight Chorus: A Substorm Phenomenon, *J. Geophys. Res.*, *79*, 118–127, doi:10.1029/JA079i001p00118.
- Tsurutani, B. T., and E. J. Smith (1977), Two types of magnetospheric ELF chorus and their substorm dependences, *J. Geophys. Res.*, *82*, 5112–5128.
- Tsyganenko, N. A. (1995), Modeling the Earth’s magnetospheric magnetic field confined within a realistic magnetopause, *J. Geophys. Res.*, *100*, 5599–5612, doi:10.1029/94JA03193.
- Tsyganenko, N. A., and M. I. Sitnov (2005), Modeling the dynamics of the inner magnetosphere during strong geomagnetic storms, *J. Geophys. Res. (Space Phys.)*, *110*, 3208, doi:10.1029/2004JA010798.
- Tsyganenko, N. A., and D. P. Stern (1996), Modeling the global magnetic field of the large-scale Birkeland current systems, *J. Geophys. Res.*, *101*, 27,187–27,198, doi:10.1029/96JA02735.
- van Allen, J. A., and L. A. Frank (1959), Radiation Around the Earth to a Radial Distance of 107,400 km., *Nature*, *183*, 430–434, doi:10.1038/183430a0.
- Vernov, S. N., and A. E. Chudakov (1960), Investigation of radiation in outer space, in *Moscow Cosmic Ray Conference, Volume III*, edited by S. I. Syrovatsky, p. 19.
- Vershinin, E. F. (1970), About the intensity of the hiss near inner boundary of the plasmopause and about the bursts of hiss with drifting frequency, *Ann. Geophys.*, *26*, 703.
- Wagenmakers, E.-J., R. Wetzels, D. Borsboom, and H. van der Maas (2011), Why psychologists must change the way they analyze their data: The case of psi, *J. Pers. Soc. Psychol.*, in press.

- Walt, M. (1994), *Introduction to geomagnetically trapped radiation*, Cambridge University Press.
- Welch, P. D. (1967), The Use of Fast Fourier Transform for the Estimation of Power Spectra: A Method Based on Time Averaging Over Short, Modified Periodograms, *IEEE Trans. Audio & Electroacoust.*, AU-15, 70–73.